Applications of Digital ASIC Array System for Noise Analysis, Non-linearity Correction, Event Classification and Reconstruction

by

Hao Yang

A dissertation submitted in partial fulfillment
of the requirements for the degree of
Doctor of Philosophy
(Nuclear Engineering and Radiological Sciences)
in The University of Michigan
2013

Doctoral Committee:

Professor Zhong He, Chair
Professor Andrew E. Yagle
Emeritus Professor Glenn F. Knoll
Associate Research Scientist Feng Zhang

To my family

ACKNOWLEDGEMENTS

First and foremost I would like to express my deepest appreciation to my committee chair, Professor Zhong He, who has been inspiring, encouraging and continuously supportive through my five-year Ph.D life in University of Michigan. Without his guidance and patient help, this dissertation would not have been possible.

I am grateful to Dr. Feng Zhang who trained me at the beginning of my Ph.D and continuously and generously provides help and excellent suggestions to my research.

I would also like to thank my other committee members, Professor Glenn Knoll and Professor Andrew E. Yagle for their support and guidance related to my Ph. D work.

I would like to acknowledge all my fellow students for their inspiring discussion related to this dissertation, including Dr. Stephen E. Anderson, Dr. Willy Kaye, Dr. Miesher Rodrigues, Dr. Yvan Boucher, and especially Dr. Yuefeng Zhu, who is the leading researcher in the digital ASIC project. I also want to thank Mr. James Berry for his engineering support to my research.

I am also grateful to all my friends, Jason M. Jaworski, William Koehler, Michael Streicher and all other friends, who make my life in Ann Arbor to be an unforgettable memory.

I could not express enough appreciation to my parents, Wenjun Ma and Rongfang Yang, elder sister Nan Ma, for their spiritual support from ten thousand miles away. Even though they may not contribute to my research directly, their warm considerations make my Ph.D life much easier and less concerned.

Last but definitely not least, I am deeply in debt to my wife, Jingjing Qian. She sacrificed so much time accompany me in the lab for countless nights and weekends. It is her love, support and encouragement that empower me to go through all difficulties in the past five years.

TABLE OF CONTENTS

CHAPTER

LIST OF FIGURES

Figure

LIST OF TABLES

Table

LIST OF ABBREVIATIONS

CdZnTe Cadmium Zinc Telluride

HPGe High Purity Germanium

FWHM Full Width Half Maximum

ASIC Application Specified Integrated Circuit

NaI(Tl) Sodium Iodide(Thallium)

e^-**-**e^+ electron-positron

HgI$_2$ Mercury Iodide

HPB High Pressure Bridgman

ATC Aurora Technologies Corporation

THM Traveling Heater Method

C/A Cathode to Anode Amplitude Ratio

BNL Brookhaven National Laboratory

VAS Voltage ASIC with Stretcher

TAT Trigger ASIC with Timing

UM University of Michigan

GM-I Gamma Medica-Ideas

cROB Computer Readout Board

CMN Common Mode Noise

ADC Analog-to-Digital Converter

TlBr Thallium Bromide

WPCT Weighting Potential Cross-Talk

NL Non-Linearity

EC Electron Cloud

ABSTRACT

Applications of Digital ASIC Array System for Noise Analysis, Non-linearity Correction, Event Classification and Reconstruction

by

Hao Yang

Chair: Zhong He

Wide band gap semiconductor detectors have been studied over decades for gamma-ray spectroscopy and CdZnTe has attracted most attention. Compared to HPGe detectors, the room temperature operation of CdZnTe detectors is an appealing feature. With the help of a 3-D position sensing technique and the use of low electronic noise analog ASIC, the energy resolution of pixelated CdZnTe detectors has been improved to 0.48% FWHM which is close to the theoretical limit of 0.2% FWHM at 662 keV achieved by HPGe detectors. However, the lateral position resolution of the pixelated CdZnTe detectors is determined by the pixel pitch size if using an analog ASIC. In addition, analog ASIC can only report the signal amplitude and triggering time information for each pixel that is not adequate to describe the charge transportation and induction details. These issues can degrade the spectroscopic performance for multiple pixel events, high energy events, and Compton scattering imaging angular resolution. In order to overcome these issues, a different version of the ASIC, the digital ASIC, has been developed, which can provide the digitized pre-amplifier signal waveforms. After several design iterations, the current digital

ASIC system contains four digital ASIC modules in a 2×2 array and has demonstrated 2 keV FWHM electronic noise. This work discusses the performance of the digital ASIC array system and its non-linear response. The non-linear response of the digital ASIC array system can be corrected experimentally and the performance of the non-linearity correction has been demonstrated. The energy resolution degradation of single-detector multiple-pixel events has also been studied. By using the pre-amplifier waveforms, three types of events can be identified and reconstructed properly, including (1) single-pixel multiple interaction events, (2) incomplete charge collection events, and (3) side-neighbor charge leak events. The photopeak efficiency is increased and the shape of the photopeak is more symmetric. The material defect diagnosis has also been demonstrated with the analog ASIC system and a superior performance of the diagnosis has been achieved using the digital ASIC system.

CHAPTER I

Introduction

Unlike light photons, gamma-rays cannot be seen by human eyes so a detection media is needed to sense them. In 1903, Sir William Crookes made the first gamma-ray detection device, a scintillator screen of **ZnS!**. With the help of this screen, the scintillation light produced by gamma-rays was visible to the naked eyes if viewed in a dark room. This is the first time that the invisible gamma-rays were converted to visible light, and thus were observed by humans. Nowadays, one of the most popular scintillator detectors is NaI(Tl), but its energy resolution is poor at about 6.7% FWHM at 662 keV even after many years of material development [9]. The poor energy resolution is partly limited by the light generation mechanism, which requires 25 eV energy to produce one photon as information carrier [10]. In order to overcome this limitation, semiconductor detectors have been used since they can generate a much larger number of information carriers, in the form of electron-hole pairs, for a given gamma-ray energy. The current best spectroscopic performance is achieved by HPGe detectors, 900 eV FWHM at 662 keV (0.14%) [11]. However, due to their narrow band gap which leads to high thermal noise at room temperature, HPGe detectors needs cryogenic cooling to be able to operate in room temperatures. In contrast, CdZnTe detectors have much wider band gap allowing for room temperature operation. In this thesis, all experiments were conducted at ambient temperatures without liquid nitrogen cooling.

1.1 Room Temperature 3-D Semiconductor Detectors

1.1.1 Room Temperature Operation

At any nonzero temperature, electron-hole pairs can be generated in semiconductor detectors by thermal energy. The thermally generation rate of electron-hole pairs can be calculated via Eq. 1.1 [10], where T is the absolute temperature, E_g is the band gap energy, k is Boltzmann constant and C is proportionality constant characteristic of the material. Clearly, the equilibrium concentration of thermally generated electron-hole pairs strongly depend on the temperature and will decrease significantly if the band gap is wider. Since the forbidden band gap energy is 0.7 eV for germanium, the thermally generated electron-hole pairs can produce too much leakage current at room temperature. Even though Si has a wider band gap energy, 1.12 eV, and thus operable at room temperatures; silicon's low atomic number, 14, causes it to have very small cross sections for high energy gamma rays. The band gap energy of 1.64 keV and average atomic number 49.1 for CdZnTe make it a good candidate for room temperature operation detector material [12–14].

$$p(T) = CT^{3/2}\exp(-\frac{E_g}{2kT}) \tag{1.1}$$

A High Pressure Bridgman(HPB) technique developed by Aurora Technologies Corporation(ATC) makes it possible to grow high quality CdZnTe crystals [15]. In 1992, it was reported for the first time that CdZnTe could achieve useful energy spectroscopy under temperatures up to 100°C. In addition, it was observed that the HPB CdZnTe detectors did not polarize under constant bias for seven days. Polarization had prevented CdTe and HgI_2 from practical applications [16,17]. This progress made CdZnTe crystals much more promising than HgI_2 and CdTe crystals, which had polarization issue over decades [18–20]. Recently, Redlen technology applied Traveling Heater Method(THM) to produce large volume CdZnTe detectors and the stability of these detectors has been studied by Dr. Yvan Boucher [21].

1.1.2 The Shockley-Ramo Theorem

As previously explained, the gamma-ray energy is converted into electron-hole pairs in semiconductor detectors through three major types of interaction: photoelectric absorption, Compton scattering and electron-positron(e^--e^+) pair production. Therefore, the induced signal on the electrode caused by the moving electron-hole pairs driven by the internal electric field is an indirect measurement of the incident gamma-ray energy. Prior to Shockley-Ramo Theorem, the induced charge Q, caused by moving charge on an electrode is calculated by Eq. 1.2, where φ is the electric potential, ρ is the space charge density, ε is the dielectric constant, E is the instantaneous electric field at each point of the moving charge trajectory and S is the surface surrounding the electrode. Since the electric field E, changes with the position of the moving charge, the induced charge Q, calculation could be very tedious for every point on the trajectory. The Shockley-Ramo Theorem, independently found by Shockley and Ramo in 1930s, states that the induced signal, ΔQ, on an electrode by a charge q moving from $\mathbf{x}_i$ to $\mathbf{x}_i$ is given by Eq. 1.3 [1, 22, 23], where $\mathbf{E_0}$ and φ_0 are the weighting field and the weighting potential respectively. The weighting field and the weighting potential are calculated by setting the collecting electrodes to unit potential and the other electrodes to zero, which can be calculated by Ansoft Maxwell 2D software[1].

$$\nabla^2\varphi = \frac{\rho}{\varepsilon} \qquad \mathbf{E} = -\nabla\varphi \qquad Q = \oint_S \varepsilon\mathbf{E}\cdot d\mathbf{S} \tag{1.2}$$

---

[1] Ansoft_Inc.: 225 West Station Square Drive, Suite 200, Pittsburgh, PA 15219, USA

$$\Delta Q = \int_{\mathbf{x}_i}^{\mathbf{x}_f} qE_0 \cdot d\mathbf{x} = -q[\varphi_0(\mathbf{x}_f) - \varphi_0(\mathbf{x}_i)] \tag{1.3}$$

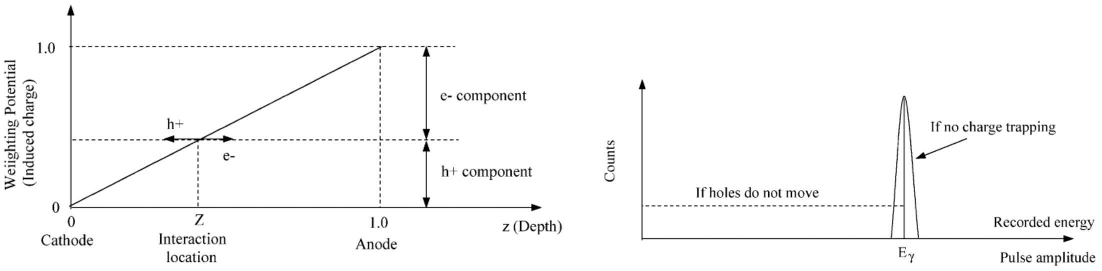

(a) (b)

Figure 1.1: The weighting potential of the anode on a conventional detector with planar electrodes and the induced signal components from the electrons and holes (a). (b) shows the expected energy spectra for mono-energetic gamma-ray with full energy deposition at different interaction depths. [1]

With the help of Shockley-Ramo Theorem, the induced signal can be easily calculated by the product of the charge and the weighting potential change. For a conventional detector with planar electrodes, the weighting potential changes linearly from 0 to 1 as shown in Fig. 1.1(a). For a typical planar HPGe detector, since the electron and hole lifetimes are long, the induced signal does not depend on the interaction depth. Thereafter, the recorded spectrum should have a photopeak representing the incident mono-energetic gamma-ray with full energy deposition as shown in solid curve in Fig. 1.1(b). However, as shown in Table 1.1, the mobility of electrons is much greater than that of holes in CdZnTe and HgI_2 and the mobility-life time product, $\mu\tau$, of holes is much smaller than that of electrons, which makes the collection of holes very difficult. Usually, during the charge collection time of electrons, the holes can be considered stationary. This will result in no photopeak in the spectrum for mono-energetic gamma-rays, shown as a dashed curve in Fig. 1.1(b), since the induced signal amplitude linearly depends on the interaction depths. In order to overcome the severe trapping and slow moving of holes, the single polarity charge sensing technique was implemented on semiconductor detectors.

Table 1.1: Material Properties at 300 K [8]

Material	μ_{e^-} (cm^2/Vs)	τ_{e^-} (s)	μ_{h^+} (cm^2/Vs)	τ_{h^+} (s)
Ge[2]	3.6×10^4 [24]	$>10^{-3}$	4.2×10^4 [24]	10^{-3}
CdZnTe	1000	3×10^{-6}	50 - 80	10^{-6}
HgI_2	100	10^{-6}	4	10^{-5}

1.1.3 Single Polarity Charge Sensing and 3-D Correction

The single polarity charge sensing technique was originally implemented in planar gas detector by Frisch in 1940s [25]. The key modification of the planar electrodes is the additional Frisch grid. Fig. 1.2 illustrates the principle of the Frisch grid detector [2]. The weighting potential between the cathode and the gird is zero and increases to 1 linearly from the grid to the anode. Therefore, according to the Shockley-Ramo Theorem, only the electrons passing the Frisch grid contribute to the induced signal on the anode so the effect of slow ions is totally removed. Since the size of gas detector can be large and the gap between the grid and the anode is very small, it can still have a reasonable size of detection region.

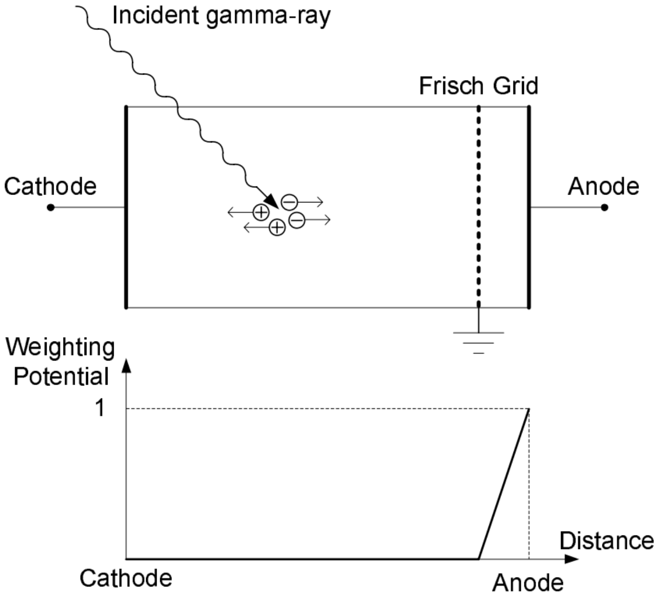

Figure 1.2: Frisch grid detector and the weighting potential of its anode [2]

---

[2] The electron and hole mobilities μ_{e^-} and μ_{h^+} are at 77 K.

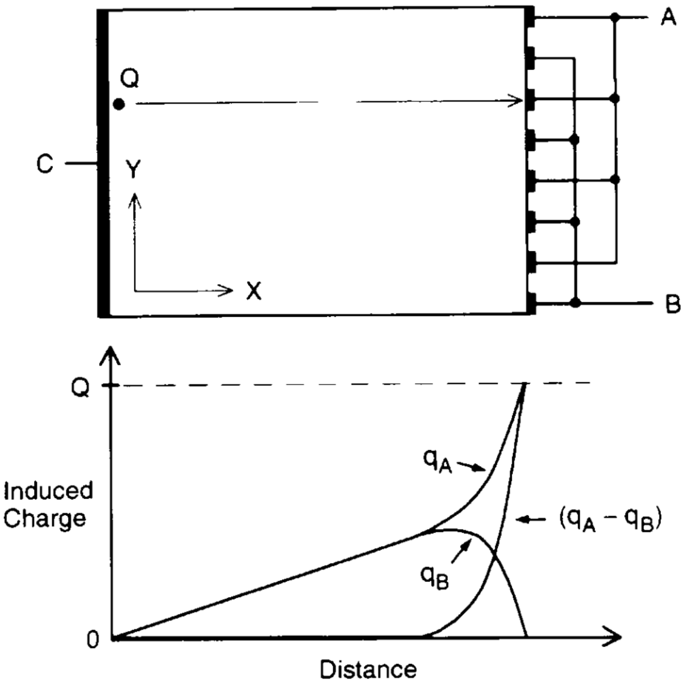

Figure 1.3: Principle illustration of coplanar grid detector [3]

One single polarity charge sensing technique was applied to semiconductor detectors by Luke in 1994 using the coplanar grid electrodes as shown in Fig. 1.3 [3, 26]. The signal difference between two grid electrode resembles the weighting potential plot in Fig. 1.2. Thus, the signal difference does not depend on the interaction depth anymore, which eliminates the trapping and slow drifting issue of the holes. A 5% FWHM energy resolution at 662 keV on a cube of 5 mm CdZnTe detector was observed the first time. Since the CdZnTe detector can have electron trapping as well as non-uniformity issues, it is very difficult to further improve the spectroscopic performance of a coplanar grid detector. In order to overcome these issues, Dr. Zhong He invented 3-D position sensing technique by combining 2-D lateral position sensing using a pixelated anode design [27] based on the small pixel effect [28] and the depth sensing technique [29,30]. Fig. 1.4 illustrates the pixelated detector used in this study and the corresponding weighting potential for one of the anode pixels and the cathode

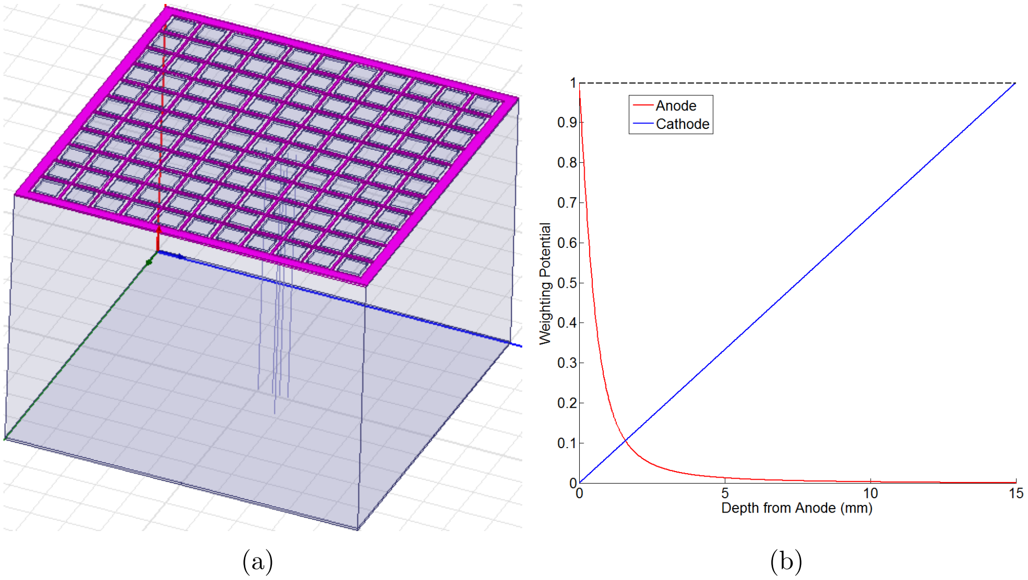

(a) (b)

Figure 1.4: Illustration of a pixelated detector (a) and the weighting potential of one anode pixel and the cathode (b)

simulated by Ansoft Maxwell 2D software[3]. The highlighted pink part in Fig. 1.4(a) is the steering grid used to help the charge collection for multiple pixel events and it is usually biased at a lower potential than the anode pixels during operation. According to the weighting potential in Fig. 1.4(b), the signal amplitude of an anode pixel does not change significantly until the electrons get very close to the anode surface while that of the cathode changes linearly with the interaction depth. Therefore, the interaction depth can be calculated by the cathode to anode signal amplitude ratio C/A, which is known as the C/A depth sensing technique.

With the help of 3-D position sensing technique, every gamma-ray interaction can be located in a detector. Therefore, each detector can be divided into many voxels and the detector response can be calibrated based on each voxel, which is called 3-D correction [31]. Typically, for a $20\times20\times15$ mm^3 CdZnTe detector, there are 11 by 11 pixels and 40 depth bins so it adds up to about 5000 voxels. Due to the detector material non-uniformity, the pixel by pixel correction is very critical in order to further improve the spectroscopic performance of CdZnTe detectors. Besides the material

---

[3] Ansoft_Inc.: 225 West Station Square Drive, Suite 200, Pittsburgh, PA 15219, USA

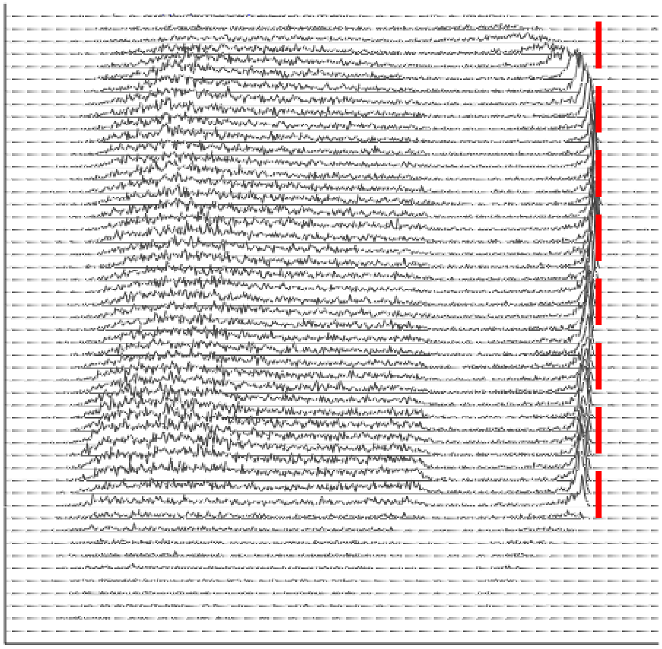

Figure 1.5: Depth separated spectrum of one anode pixel. The horizontal axis is energy in ADC unit and the vertical axis corresponds to different interaction depths from cathode to anode side bottom to top.

non-uniformity, different interaction depths lead to different electron trapping, which can also broaden the photopeak of the full energy deposition events. Fig. 1.5 illustrates the trapping correction for one anode pixel. The difference between the photopeak centroid and the red dash line is used to calibrate the electron trapping effect. After 3-D correction, the best energy resolution of a large volume CdZnTe detector at room temperature has been improved to 0.48% FWHM at 662 keV using BNL ASIC with 2 keV FWHM electronic noise and 3 MeV dynamic range [4]. A better energy resolution of 0.39% FWHM at 662 keV was also demonstrated with 1.2 MeV dynamic range, which was only twice the theoretical limit of 0.2% [32].

1.2 Readout ASIC Evolution

1.2.1 Analog ASIC

Due to the pixelated anode design, a multiple-channel readout system is required. In 1998, the ASIC VA1 chip designed by IDEAS[4] was applied to two 1 cm^3 cubic CdZnTe detectors with 11 by 11 anode pixels. Each VA1 ASIC had 128 independent signal readout channels for the anode pixels with the dynamic range up to $\sim$1MeV. Cathode and grid channels were readout separately by two charge-sensitive pre-amplifiers A250 from AMPTEK[5]. The energy resolution was 1.75% FWHM at 662 keV for all single pixels [33, 34]. However, this version of ASIC could not read out cathode or grid channel directly so a discrete circuitry had to be built resulting in noisy cathode and grid signals. In addition, it does not have peak hold capability so it only holds the sample amplitude based on the peaking time. It was also incapable of reconstructing multiple pixel events since the C/A ratio is no longer sufficient to determine individual interaction depths.

A second generation of readout system based on the IDEAS VAS_UM2[6]/TAT2[7] ASIC chip applied to two 1.5×1.5×1 cm^3 CdZnTe detectors in 2003 [35]. Each VAS_UM2 chip has 32 independent channels for signal amplitude and each TAT2 chip has 32 independent channels for triggering time sensing. One VAS_UM2 chip and one TAT2 chip form a chipset and four chipsets are needed for 121 anode pixels, the grid channel and the cathode channel. Prof. He's group demonstrated the capability of multiple pixel events reconstruction for the first time, with energy resolutions of 1.57% and 2.13% FWHM at 662 keV for two-pixel and three-pixel events along with single-pixel event energy resolution of 1.11% FWHM [35]. The third generation ASIC, the IDEAS VAS_UM3.1/TAT3, inherited the architecture of the second gener-

---

[4] IDEAS Veritasveien 9, N-1332 Hovik, Norway

[5] Amptek Inc., 6 De Angelo Drive, Bedford, MA 01730 USA

[6] Voltage ASIC with Stretcher, version2

[7] Trigger ASIC with Timing, version 2

ation with lower electronic noise. An energy resolution of sub-1%(0.93%) FWHM at 662 keV for single-pixel events on CdZnTe detectors was achieved for the first time in 2004 [36]. The fourth generation of VAS_UM/TAT4 ASIC was developed in 2005 with 129 independent channels on a single chip [37]. Since each chip is much more compact than previous versions, the readout mother board was able to take 3 by 3 ASIC modules, each consists of one ASIC chip and one CdZnTe detector. This new design can expand the effective detection volume of CdZnTe detectors. The volume of each single CdZnTe crystal is limited by the material growth process. In 2010, the Polaris system with an array of 18 position sensitive detectors using 6 cm^3 pixelated CdZnTe crystals demonstrated the sub 1% energy resolution at 662 keV for all single-pixel events [38].

1.2.2 Digital ASIC

Since the second generation of VAS_UM2/TAT2 ASIC was invented, multiple pixel events were proven to be able to reconstructed with separate energy depositions and locations, which made Compton imaging possible on a single CdZnTe detector. In 2003, Dr. Carolyn E. Lehner first demonstrated the capability of full 4π Compton imaging on a single $15\times15\times10$ mm^3 CdZnTe detector and 17° FWHM angular resolution at 662 keV was achieved after 10 iterations using the weighted list-mode maximum likelihood reconstruction [39, 40]. However, the angular resolution of single detector Compton imaging heavily depends on the position resolution, which was limited by both the electronic noise and the pixel pitch size. Since the multiple pixel events are reconstructed based on the drift time to C/A ratio depth conversion, lower electronic noise and timing resolution will lead to better interaction depth resolution. The lateral position resolution cannot be better than the pixel pitch size even though the electron cloud size may be smaller than that. For lower energy gamma rays, an alternative imaging method, coded aperture, has to be used since the cross section of

Compton scattering is too small [41]. Better position resolution on the detector will improve angular resolution and signal-to-noise ratio of reconstructed images for both Compton Imaging and coded aperture imaging. In order to achieve better position resolution [42, 43], a digital readout ASIC was developed and first demonstrated the sub-pixel position capability in 2010 [44]. A similar idea has been applied to HPGe detector by using proximity electrode and reading out the signal waveforms on both the collecting strip electrode and its neighboring stripe electrodes [45]. Different from the analog ASIC presented before, which can only provide the amplitude and timing information for each channel, the digital ASIC can sample the pre-amplifier output on each channel directly and hold all the samples on a bank of capacitors for later A/D conversion. These signal samples contain sufficient information for reconstruction purpose, which will further improve the energy resolution and position resolution of pixelated CdZnTe detectors. The application of signal waveforms to improve energy spectrum characteristic of CdZnTe detectors can be dated back to 1997 [46]. A clustering method to process signals from a CdZnTe detector based on waveforms have demonstrated improved energy resolution on CdZnTe detectors [47]. The feasibility in neutrino-less double beta decay research using a fine-pitched pixelated CdZnTe detector has also been studied with a digital waveform acquisition system [**?**]. Besides the applications on CdZnTe detectors, the signal waveform processing has also been applied to TlBr detectors in order to study the crystal material properties such as electron drift mobility [48].

There are several digital readout systems being used such as digital oscilloscope and waveform digitizers [**?**, 46, 47]. However, these systems can only read out a few channels so they cannot be easily applied to pixelated detectors. In order to readout more channels, a digital ASIC readout system has been collaboratively developed by Dr. Zhong He's group from University of Michigan and Gamma Medica-Ideas. The first generation digital ASIC can only be operated in full readout mode, which means that all 121 anode pixel channels plus cathode and grid channels will be read out regardless of the number of triggered pixels. Since it takes time to perform A/D conversion, the maximum counting rate was limited to about 200 cps. The second generation digital ASIC was designed to have two modes of readout: full readout and sparse readout. In contrast to full readout mode as described before, only those channels that are triggered and their selected neighbor pixel anode channels will be readout in sparse readout mode. Usually, within the dynamic range up to 3 MeV, the average number of channels triggered is much smaller than 121 the counting rate was increased significantly. The current generation of digital ASIC system used in this study has an array of 2 by 2 digital ASICs with 2 keV FWHM electronic noise. The 32 and 36 keV K X-rays from ^{137}Cs were observed separately for the first time with the digital ASIC array system.

1.3 Objective and Overview of This Work

This work consists of three major parts: (1) digital ASIC array readout system; (2) 3-D semiconductor detectors; and (3) event classification and improved reconstruction. Two different types of digital readout systems will be introduced in Chapter II. The prototype digital system was designed by Dr. Stephen E. Anderson [49] due to the limited sampling time window not achievable on the digital ASIC readout system and a new data acquisition software has been developed to better utilize that system. The noise performance of current digital ASIC array system has been studied and the spectroscopic performance with large volume CdZnTe detectors will be demonstrated. Those large volume CdZnTe detectors are fabricated by different methods and their active detection volume is critical for radiation detection. Chapter III will introduce a relative efficiency experiment to prove that the active volume of 6 cm^3 Redlen detectors, grown by Traveling Heater Method(THM), is similar to that of eV-Products detectors, which were grown by High Pressure Bridgman(HPB). Chapter V and VI will focus on the application of the digital ASIC array system. The event classification algorithms for three major gamma-ray interactions: (1) photoelectric absorption; (2) Compton scattering; and (3) pair production, have been developed with the prototype digital system by Dr. Stephen E. Anderson [49]. Besides his work, other groups have tried to reject incomplete charge collection events using analog ASIC and their capability is limited by the available information [50, 51]. With the low electronic noise digital ASIC array system, this thesis work has extended event classification technique to three more types of events, including (1) multiple-interaction under a single-pixel anode events; (2) incomplete charge collection events; and (3) side-neighbor charge leakage events. In addition, since the digital ASIC can provide pre-amplifier signal waveforms rather than amplitude and trigger timing only, it can perform diagnosis measurements on material defects based on the sub-pixel position distribution and the change of pulse rise time corresponding to material properties, more details are shown in Chapter VI.

CHAPTER II

Digital Readout Systems

High Purity Gemanium(HPGe) detectors have served the radiation detection applications for decades. There are two typical electrode configurations for HPGe detectors, planar and coaxial. Since both electrode configurations are very simple, the signal processing circuitry can be designed with discrete electronic components. However, the electron and hole mobility in CdZnTe has significant difference so the small pixel effect is utilized to overcome the depth-dependent signal amplitude variation. CdZnTe detectors used in this study have 11×11 pixel anodes, 1 common steering grid and 1 planar cathode, which requires 123 readout channels. It is not practical to build the signal processing circuitry with discrete components due to the large number of readout channels. Thanks to the evolution of silicon technology, the signal processing circuitry can be built on a very small chip, also known as, Application Specified Integrated Circuit(ASIC). Prof. He's group at University of Michigan have been collaborating with Gamma Medica-Ideas(GM-I) to develop ASIC readout systems for pixelated CdZnTe detectors. These ASICs are named VAS_UM/TAT. After several design iterations, the current VAS_UM2.1/TAT4 chip has 129 channels, which is sufficient for pixelated CdZnTe detectors described above. With the help of this ASIC, our CdZnTe detector has achieved excellent spectroscopy performance(<1% FWHM) at 662 keV [36]. However, there are several problems of the current VAS_UM/TAT

ASIC. For instance, this ASIC cannot identify multiple-interaction under the same pixel events or differentiate between a true charge collection signal and a transient signal due to weighting potential crosstalk. In order to overcome these issues, Dr. Zhong He suggested that the entire pre-amplifier signal be digitized. Since the digitized signal provides the full information on induced charge as a function of time on each electrode, the event reconstruction using a digital ASIC should outperform the analog readout system. There are two major digital readout systems used by our group introduced in this chapter, (1) VAD_UM digital ASIC and (2) CompuScope GaGe digitizer.

2.1 UM_VAD Array System

UM_VAD array system is comprised of 4 digital ASICs and 1 readout (Espresso) board. The front end card which carries the 4 digital ASICs is shown in Fig. 2.1. These 4 ASICs are divided into 2 groups. Each group has its own receiver circuitry and ADC unit. In order to reduce the trace length and minimize the electronic noise, these 4 ASICs are placed in two different orientations on the front end board, which is shown in Fig. 2.1, two on the left and two on the right. Each digital ASIC has 124 channels with individual charge-sensitive pre-amplifiers. The pre-amplifier signals are sampled constantly at a frequency up to 80MHz. Since there are only 160 storage cells for each channel, a higher sampling frequency results in a shorter sampling time window. The data communication is bridged via a computer readout board(cROB 8) designed by GM-I and a national instrument PCI-DIO-32HS card. The detailed functionality has been introduced in Dr. Yuefeng Zhu's Ph.D thesis [5]. This session will describe some experimental observations and electronic noise analysis.

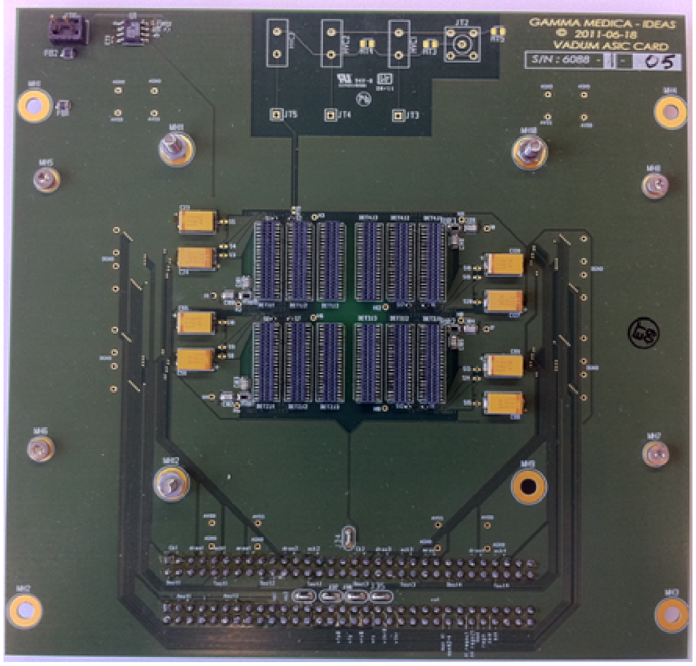

Figure 2.1: Digital ASIC array front end card.

2.1.1 Eelectronic Noise on a Single Channel

Each digital ASIC has 2 readout modes, full readout mode and sparse readout mode, and the readout of each mode has to be initiated by an anode trigger. In full readout mode, all 121 anode pixels are read out after an anode trigger occurs. In sparse readout mode, only the triggered anode pixel and their selected neighbor pixels are read out. In the full readout mode, signals on all channels including those without any induced charge, can be readout to perform noise analysis. Fig. 2.2 shows the distribution of signal amplitude distribution on channel 20 when there is no induced charge on this pixel anode. This is the case when this pixel anode has no trigger, or is not a neighbor of any triggered anode pixels. The FWHM of this distribution is a direct measure of the UM_VAD system noise. We found that on the previous iteration of the digital ASIC system, the noise distribution has a similar pattern on two systems produced in the same batch shown in red on Fig. 2.3. However, the noise performance measured on the system without the ASIC input traces does not show this pattern. It was verified that the noise pattern was caused by the lengthy

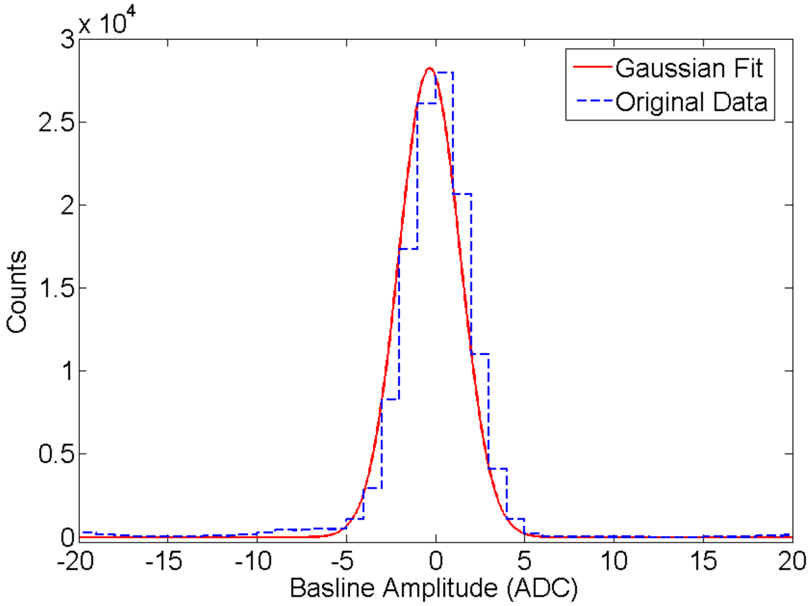

Figure 2.2: Baseline amplitude distribution on one anode channel (Channel 20)

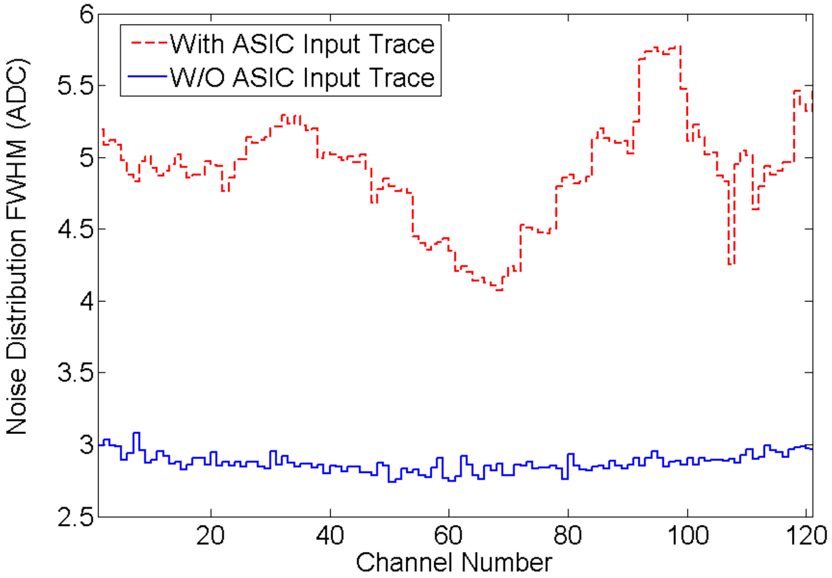

Figure 2.3: Noise distribution over 121 anode channels with and without ASIC input traces in on previous digital ASIC system. No detector was connected.

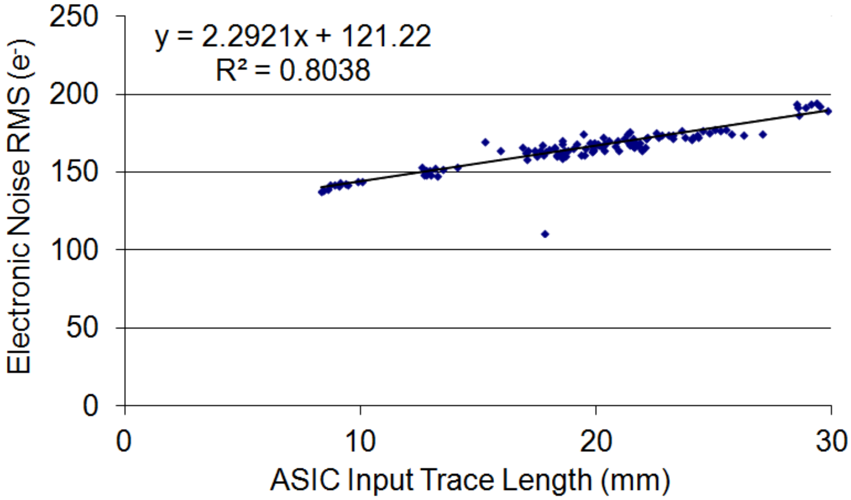

Figure 2.4: Correlation between the length of ASIC input traces and the electronic noise

ASIC input traces. Fig. 2.4[1] illustrates the correlation between the length of ASIC input traces and the electronic noise measured by GM-I. From Fig. 2.3, the measured average noise is about 5 ADC channels FWHM over 121 pixels, which corresponds to about 2.8 keV FWHM at 662 keV. This electronic noise does not include the components caused by the detector input capacitance or the leakage current between the pixels and steering grid. The electronic noise of the system in operation is about 3.5 keV FWHM.

On the current digital ASIC array system, the length of ASIC input traces has been reduced and the correlation between the measured noise and trace length is no longer significant. Additionally, the receiver gain has been increased to minimize the noise contribution of the Espresso board. Fig. 2.5 shows the spectra of a ^{137}Cs source on two versions of the digital ASIC system. Lower electronic noise results in better depth resolution and sub-pixel position resolution, which are very critical for Compton imaging. Fig. 2.6 shows the system noise measured with the detector connected and both the cathode bias and steering grid bias were applied. The average

---

[1] This plot is provided by Gamma Medica-Ideas.

noise is about 4.5 ADC channels FWHM, which is equivalent to 2 keV FWHM at 662 keV. As introduced in the previous chapter, the interaction depth is determined by the cathode-to anode signal ratio, $d = \frac{C}{A} \cdot D$. Thus, the depth uncertainty can be derived as follows,

$$\sigma_d = \sqrt{(\frac{\sigma_C}{C})^2 + (\frac{\sigma_A}{A})^2} \cdot \frac{C}{A} \cdot D, \tag{2.1}$$

where C is the cathode signal amplitude, A is the anode signal amplitude, D is the detector thickness, σ_d is the depth uncertain, σ_C is the cathode signal uncertainty and σ_A is the anode signal uncertainty. Usually, σ_C or σ_A does not solely depend on the electronic noise and contain contribution from the statistical nature of the charge generation, incomplete charge conversion, etc. However, the uncertainty caused by the electronic noise is not negligible since the best observed energy resolution is less than 0.5% at 662 keV [32], corresponding to an overall uncertainty of about 3.5 keV FWHM. Therefore, the decrease of electronic noise 3.5 keV to about 2 keV is a significant improvement because both σ_C and σ_A is reduced, indicating smaller than σ_d by Eq. 2.1

Using the latest digital ASIC array readout system, having a 2 keV FWHM electronic noise, the energy spectrum for a ^{137}Cs source is shown in Fig. 2.7. Two characteristic x-rays at 32 keV and 36 keV from the ^{137}Cs source are clearly resolved. This is a result of a lower electronic noise.

2.1.2 Eelectronic Noise Correlation on Multiple Channels

There are three major types of gamma-ray interactions, photoelectric absorption, Compton scattering and pair production. Typically, the higher the energy of the incident gamma ray has, the more number of interactions it will have with the detector material, which will lead to multiple pixel events in pixelated detectors. Sometimes, the electron cloud generated by a single interaction can be shared by multiple pixels

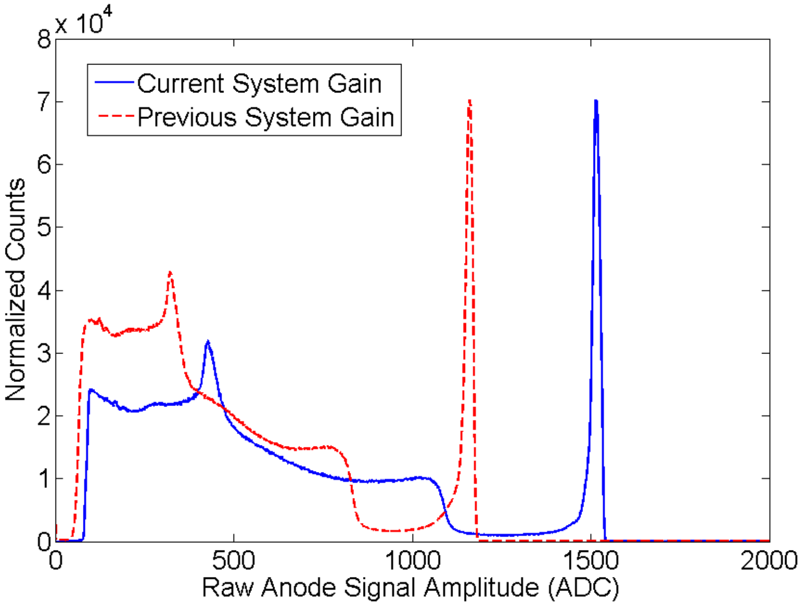

Figure 2.5: Raw spectra of ^{137}Cs source on two versions of digital ASIC system

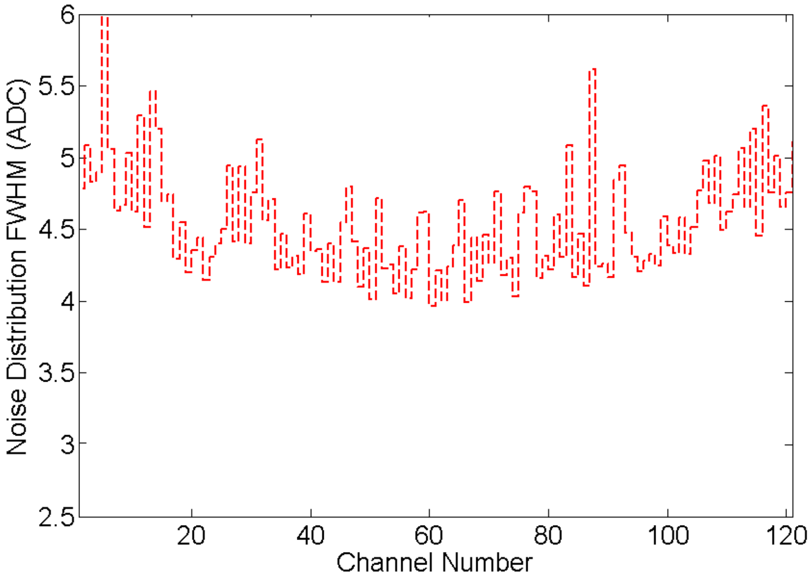

Figure 2.6: Noise distribution over 121 anode channels with detector plugged in and required high voltage biases on current digital ASIC system.

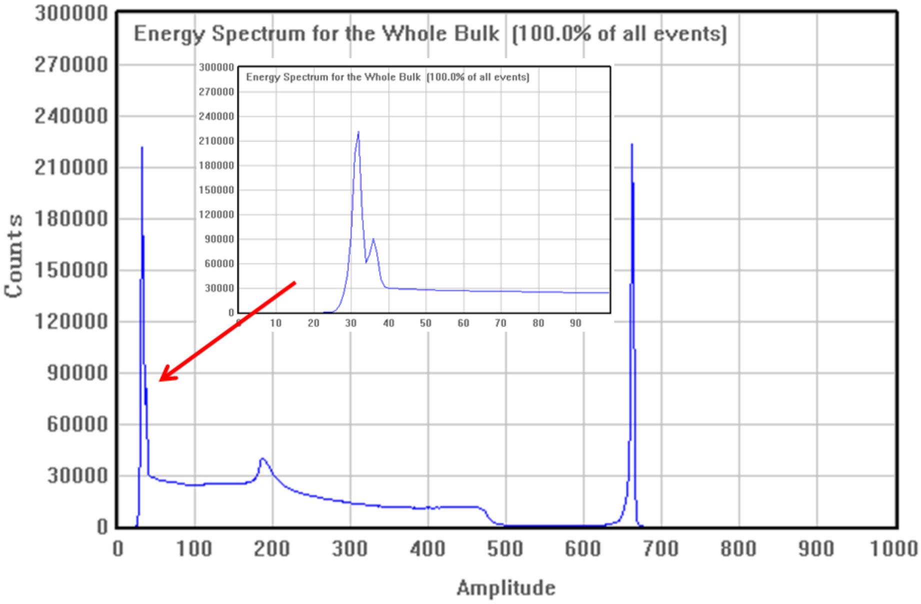

Figure 2.7: The spectrum of a ^{137}Cs source after depth correction.

as well. These multiple-pixel events, especially Compton scattering events, are essential for Compton imaging. In order to reconstruct the energy deposition of these multiple pixel events, it is necessary to add up signals from multiple channels. Unlike the single pixel events reconstruction, whose energy resolution is affected by the electronic noise on a single ASIC channel, the energy resolution of these multiple pixel events is determined by the electronic noise over multiple pixels. If the electronic noise on different channels is positively correlated, the energy resolution of multiple pixel events will degrade faster than the case if the noise of different channels are uncorrelated.

In Dr. Yuefeng Zhu's dissertation [5], the common mode noise was observed on the previous digital ASIC system and the conclusion was that the common mode noise contributes to about 10% in the total electronic noise. The electronic noise of the latest digital ASIC system with and without the common mode noise correction is shown pixel-by-pixel in Fig. 2.8. It can be seen that about 15% of the electronic noise is caused by the common mode noise. The higher fraction on the current digital ASIC array system does not indicate worse common mode noise since the overall elec-

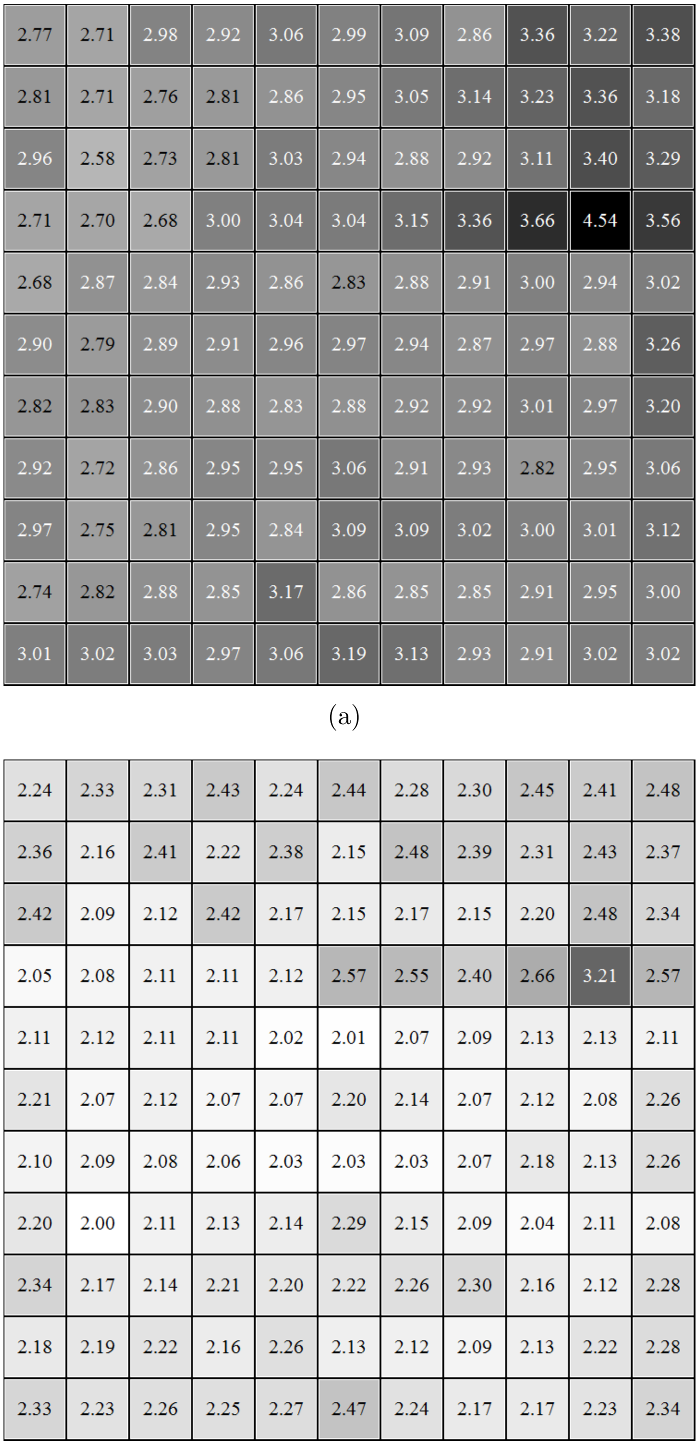

2.77	2.71	2.98	2.92	3.06	2.99	3.09	2.86	3.36	3.22	3.38
2.81	2.71	2.76	2.81	2.86	2.95	3.05	3.14	3.23	3.36	3.18
2.96	2.58	2.73	2.81	3.03	2.94	2.88	2.92	3.11	3.40	3.29
2.71	2.70	2.68	3.00	3.04	3.04	3.15	3.36	3.66	4.54	3.56
2.68	2.87	2.84	2.93	2.86	2.83	2.88	2.91	3.00	2.94	3.02
2.90	2.79	2.89	2.91	2.96	2.97	2.94	2.87	2.97	2.88	3.26
2.82	2.83	2.90	2.88	2.83	2.88	2.92	2.92	3.01	2.97	3.20
2.92	2.72	2.86	2.95	2.95	3.06	2.91	2.93	2.82	2.95	3.06
2.97	2.75	2.81	2.95	2.84	3.09	3.09	3.02	3.00	3.01	3.12
2.74	2.82	2.88	2.85	3.17	2.86	2.85	2.85	2.91	2.95	3.00
3.01	3.02	3.03	2.97	3.06	3.19	3.13	2.93	2.91	3.02	3.02

(a)

2.24	2.33	2.31	2.43	2.24	2.44	2.28	2.30	2.45	2.41	2.48
2.36	2.16	2.41	2.22	2.38	2.15	2.48	2.39	2.31	2.43	2.37
2.42	2.09	2.12	2.42	2.17	2.15	2.17	2.15	2.20	2.48	2.34
2.05	2.08	2.11	2.11	2.12	2.57	2.55	2.40	2.66	3.21	2.57
2.11	2.12	2.11	2.11	2.02	2.01	2.07	2.09	2.13	2.13	2.11
2.21	2.07	2.12	2.07	2.07	2.20	2.14	2.07	2.12	2.08	2.26
2.10	2.09	2.08	2.06	2.03	2.03	2.03	2.07	2.18	2.13	2.26
2.20	2.00	2.11	2.13	2.14	2.29	2.15	2.09	2.04	2.11	2.08
2.34	2.17	2.14	2.21	2.20	2.22	2.26	2.30	2.16	2.12	2.28
2.18	2.19	2.22	2.16	2.26	2.13	2.12	2.09	2.13	2.22	2.28
2.33	2.23	2.26	2.25	2.27	2.47	2.24	2.17	2.17	2.23	2.34

(b)

Figure 2.8: Pixel map of electronic noise FWHM on each channel before (a) and after (b) common mode noise correction. The unit is in keV and grey scale is from 2 to 4.

Table 2.1: Electronic Noise Corresponding to Fig. 2.9

	FWHM_1	FWHM_2	FWHM_3	$\sqrt{\text{FWHM}_1^2 + \text{FWHM}_2^2}$
Before CMN Correction	6.90	6.92	12.29	9.77
After CMN Correction	5.13	4.84	7.15	7.05

tronic noise is 50% lower on the current digital ASIC array system. Even though the common mode noise only contributes 15% to the overall single pixel electronic noise, the multiple pixel events energy resolution could degrade faster than the quadrature sum due to this noise correlation. In general, the variance of the sum of independent Gaussian random variables should be equal to the square sum of the variance of each variable. This can be used to test whether the common mode noise is completely removed. Table 2.1 shows the FWHM of the electronic noise distribution corresponding to Fig. 2.9. Before common mode noise correction, $\text{FWHM}_3 > \sqrt{\text{FWHM}_1^2 + \text{FWHM}_2^2}$, which indicates a positive correlation of the electronic noise between two pixel channels. The correlation coefficient, ρ, can be calculated via Eq. 2.2 and in this case the correlation coefficient is about 0.56. The second row in Table 2.1 shows that the positive correlation is totally removed after the common mode noise correction since FWHM_3^2 is very close to the sum of FWHM_1^2 and FWHM_2^2.

In addition to full readout mode, the digital ASIC array system can be operated in sparse readout mode if a higher counting rate is required. The common mode noise cannot be corrected as easily as in full readout mode. It has been experimentally observed that the energy resolution of two-pixel events using sparse readout mode is very similar to that using full readout mode with common mode noise correction. Therefore, the common mode noise in sparse readout mode is sufficiently low to be neglected. The reason for this behavior is still unknown.

$$\sigma_{1+2} = \sqrt{\sigma_1^2 + \sigma_2^2 + 2\rho\sigma_1\sigma_2} \tag{2.2}$$

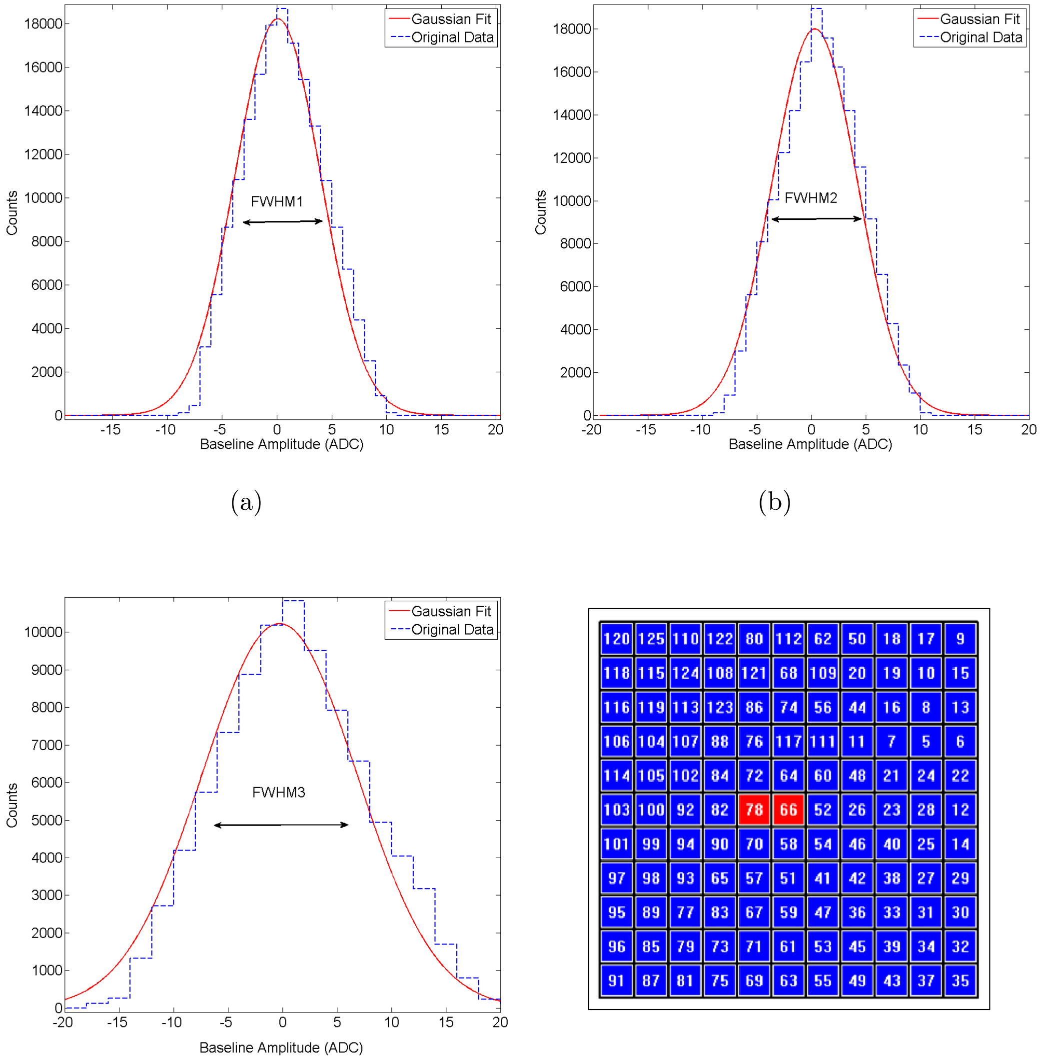

120	125	110	122	80	112	62	50	18	17	9
118	115	124	108	121	68	109	20	19	10	15
116	119	113	123	86	74	56	44	16	8	13
106	104	107	88	76	117	111	11	7	5	6
114	105	102	84	72	64	60	48	21	24	22
103	100	92	82	78	66	52	26	23	28	12
101	99	94	90	70	58	54	46	40	25	14
97	98	93	65	57	51	41	42	38	27	29
95	89	77	83	67	59	47	36	33	31	30
96	85	79	73	71	61	53	45	39	34	32
91	87	81	75	69	63	55	49	43	37	35

(a) (b)

(c) (d)

Figure 2.9: Baseline distribution on Channel66 (a), Channel78 (b) and the summation of them (c). These two channels' location is shown on pixel map (d)

.

2.1.3 Stability Measurement of ASIC Charge Sampling Cells and ADC Noise Study

In the digital ASIC array system, there are only two ADCs for four ASICs so that two ASICs share the same ADC. After the pre-amplifier signals are sampled and held by the storage cells, the ADC performs the analog-to-digital conversion to each cell one by one. There are 124(channels)×160(cells) voltages converted at 10 MHz, which implies that the longest sample holding time is on the order of a millisecond. Therefore, the ability of each cell to hold the sampled voltage value is very important. In order to study the stability, ADC conversion values of the same sample cell from different readout sequences, the corresponding time interval may vary from tens to hundreds of microseconds, were compared. Due to the sparse readout mode, the neighbor pixels will always be read out followed by the triggered pixel regardless of if there is any triggered pixel within those neighbor pixels. Fig. 2.10 shows a side-neighbor two pixel event and the pixels in the red box are read out twice due to two triggered (red) pixels. The signal difference between two times ADC represents the ADC noise and possible discharge of sample cells.

The ADC noise distribution is shown in Fig 2.11. The FWHM of the distribution is about 8 ADC channels, which is equivalent to 3.5 keV. Samples with different amplitude were also studied and there is no significant difference for the distribution, which means that the ADC noise does not depend on the sample signal amplitude. This ADC noise does not necessarily impact the final electronic noise performance since the signal amplitude is calculated by either slow shaper or system response function, which has an equivalent effect of averaging a certain number of samples. The signal amplitude correlation between two times analog-to-digital conversion are shown on Fig. 2.12. Clearly, the signal does not have observable decay, during the time interval of different ADC conversions up to several hundred microsecond, indicating very good sample hold stability.

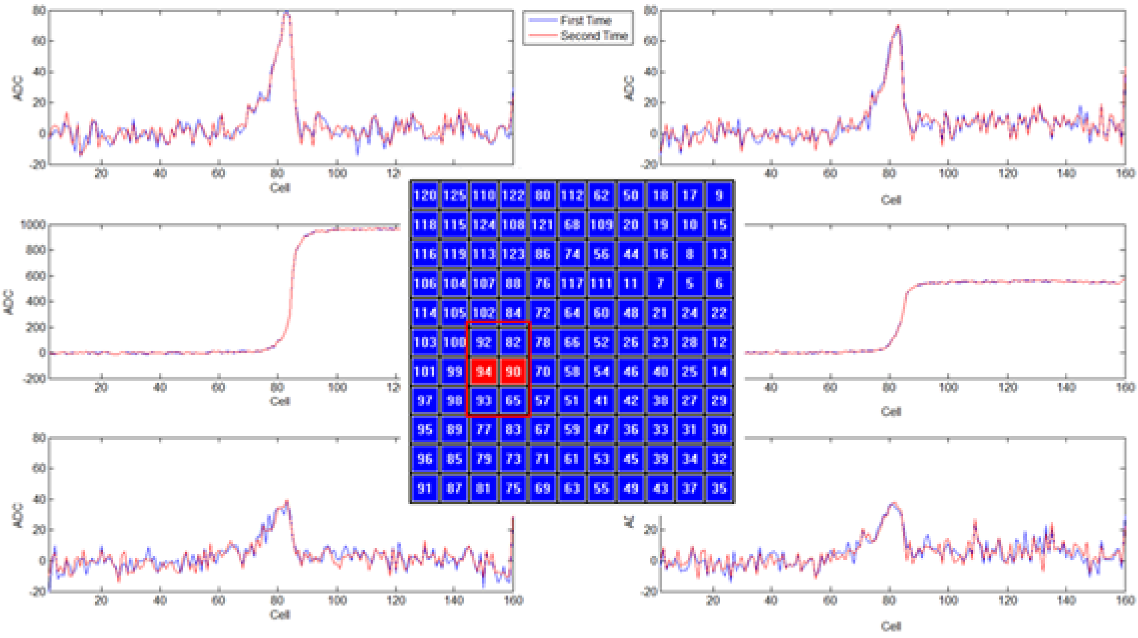

Figure 2.10: The signal comparison between two times ADC

2.2 CompuScope Gage Digitizer

In addition to CdZnTe, there are other alternative semiconductor materials, such as TlBr [52]. However, due to relatively slow mobility, the charge collection time is much longer in TlBr than that in CdZnTe. For a typical cathode side event in a 5×5×5 mm^3 TlBr detector with 1000 Volts cathode bias, the collection time is longer than 15μs [53]. In order to fully capture the pre-amplifier waveforms of both single-pixel events and multiple-pixel events, the sampling time window has to be longer than twice the charge collection time. The current digital ASIC array system cannot directly apply to TlBr detectors since the sampling time window is limited to 16μs, shorter than the 20μs required. For this reason, CompuScope cards developed by Gage Applied Technologies have been adopted as another digital readout system.

2.2.1 Hardware Description

The TlBr detector system consists of a 5×5×5 mm^3 TlBr detector, a high voltage distribution baord, 10 single charge-sensitive hybird preamplifiers and 2 CompuScope

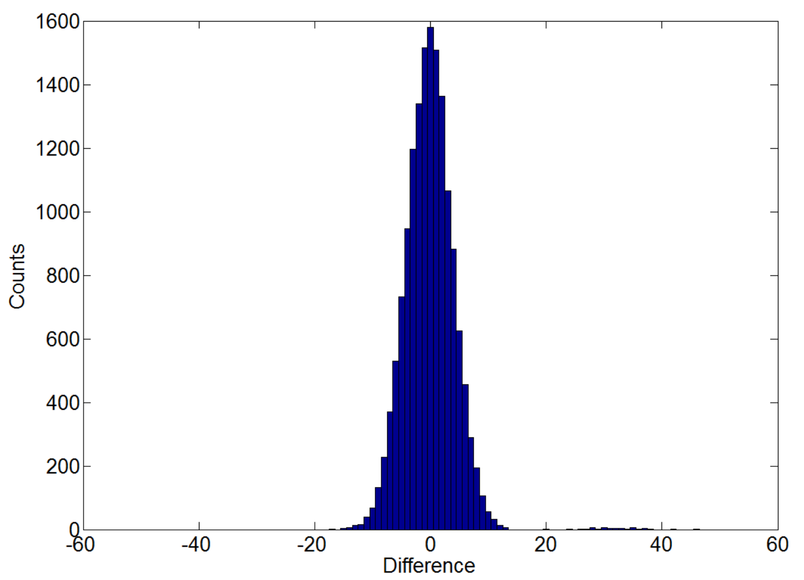

Figure 2.11: ADC noise distribution.

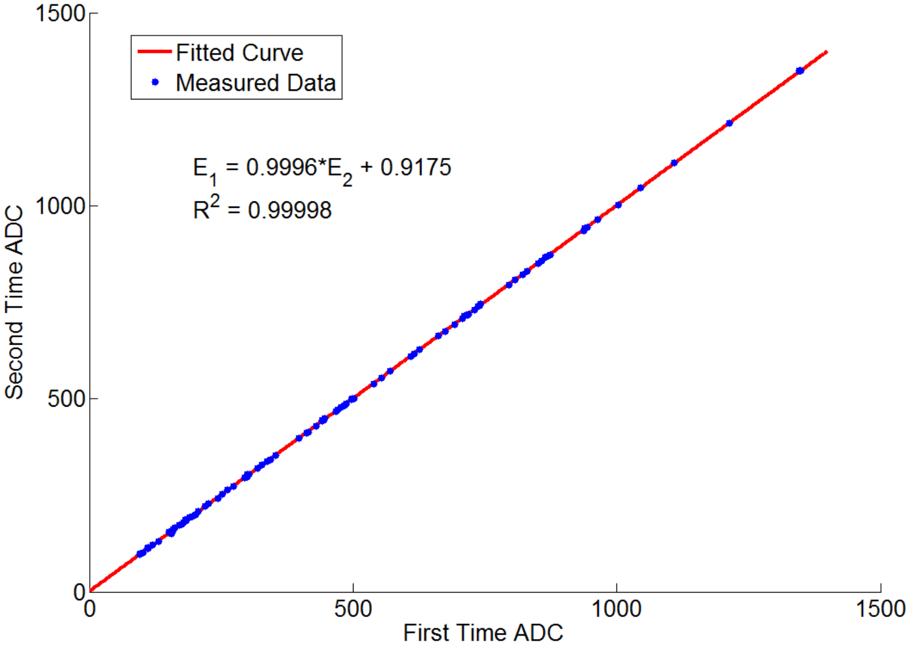

Figure 2.12: The signal amplitude correlation between two times ADC.

cards. Two CompuScope cards are required since each CompuScope has at most 8 input channels while there are 10 pre-amplifiers that need to be read out. Each CompuScope card has built-in 14 bits ADC and onboard memeory. The sampling time window can be adjusted by both the sampling frequency and the number of samples allocated. The sampling frequency can be set from 100kHz to as high as 125MHz. The number of samples allocated for each waveform is only limited by the onboard memory. Thus, the sampling time window can be set much longer than the digital ASIC array system as long as the onboard memory allows. In the TlBr detector system, each card has a memory of 128M samples shared by all input channels. If 8 channels are used on one card, then each channel can be allocated at most 16M samples. If 4 channels are used on one card, then each channel can be allocated at most 32M samples, so on so forth. Compared to 160 samples in digital ASIC array system, the CompuScope card has much more flexibility in terms of sampling time window. Typically, the sampling frequency is set at 10MHz with 512 samples allocated for each waveform in the TlBr detector system. Fig. 2.13 shows average waveforms of 20 cathode side 662 keV gamma-ray single-pixel events. The average charge collection time is about 10μs.

Two CompuScope cards are operated in master-slave mode. In this mode, the master card generates the system clock and the slave card shares this system clock via hardware connection. Two cards are also wired to share the same trigger signal in order to capture multiple-pixel events, which means that any input signal above the trigger threshold can fire both cards and all waveforms on both cards will be recorded simultaneously. Unlike the digital ASIC array system that has uniform input dynamic range for all channels, the dynamic range of CompuScope card can be set individually, which is a useful feature for sub-pixel position resolution study. In order to fully utilize these useful features, a data acquisition software based on Microsoft Foundation Classes(MFC) has been developed.

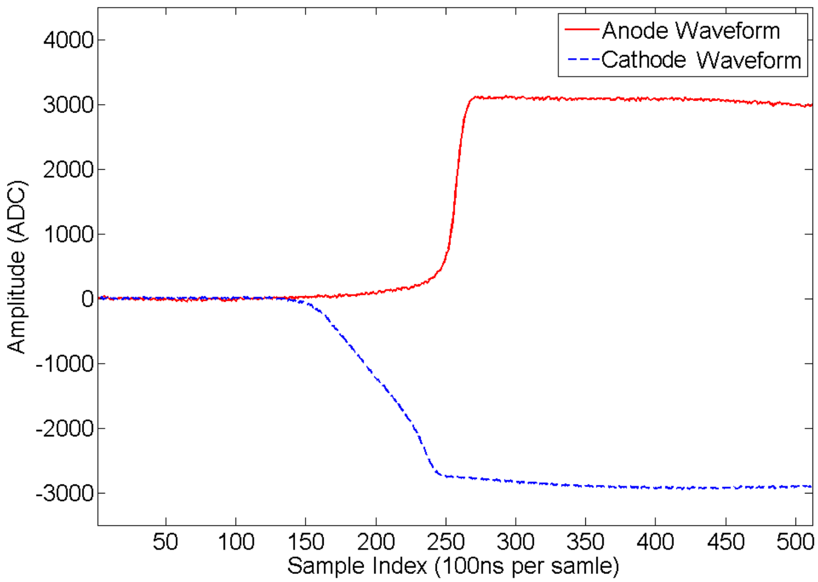

Figure 2.13: Average waveforms of 20 cathode side 662 keV gamma ray single-pixel events.

2.2.2 Data Acquisition Software

A CompuScope card was used with Matlab code previously written [49]. The matlab code works in a single thread mode as shown in Fig. 2.14. While the waveforms are saved to files, the CompuScope cards are actully ready for sampling the next event. However, until the file saving is finished, the Matlab code cannot manage the ComuScope cards to start another readout cycle, which virtually makes the system dead time longer than necessary. The system dead time is contributed from three processes shown in Table. 2.2. Usually for TlBr detectors, the system dead time due to data transfer can be neglected since the data acquisition rate is 10M Samples per second (Sa/s) and the data transfer to PC memory rate is 10 times higher. If the data saving rate is 25M Sa/s, then the system dead time is extended by 40 ns per sample. This will degrade the detector efficiency at high count rate. This is not desired if higher data collection rate are necessary to study some detectors, such as TlBr, with a limited lifetime of operation. Besides this, the Matlab code does not have a graphic user interface(GUI) so it is not user friendly to change the settings or feasible to monitor the detector response in real time. Therefore, the Matlab code was designed for post processing rather than real time operation.

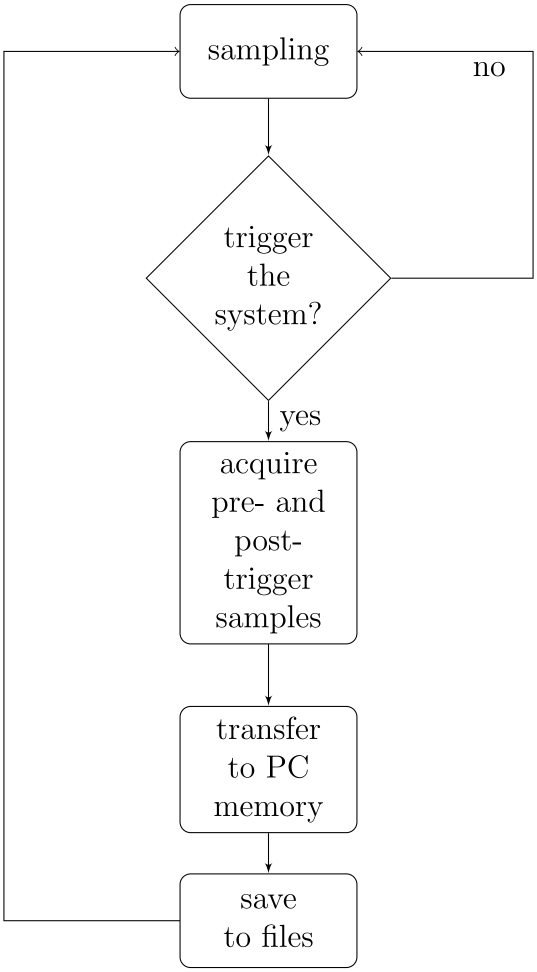

Figure 2.14: Matlab code data flow scheme

Table 2.2: Data Process Rate

	Data Process Rate
Data Acquisition	Up to 125M Sa/s
Data Transfer to PC Memory	Up to 100M Sa/s
Data Save to Hard Drive	About 25M Sa/s depending on Hardware

In order to overcome these issues and optimize the performance, a multi-thread code based on Microsoft Foundation Classes(MFC) platform has been developed. The data structure is shown in Fig. 2.15 and the major difference from the Matlab code

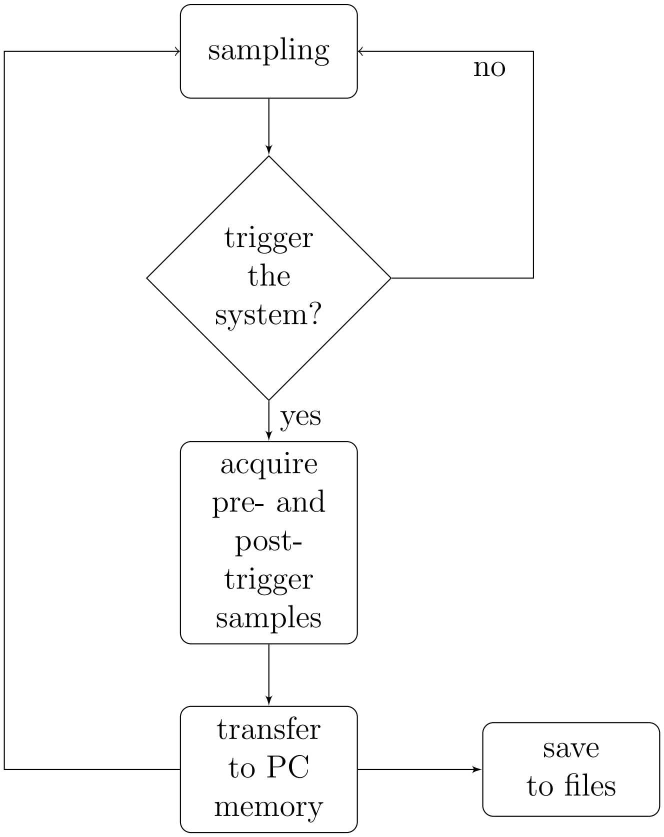

Figure 2.15: MFC code data flow scheme

is how the file saving is handled. In the MFC code, the file saving is taken care by an individual thread, which means that the CompuScope card can initiate a new readout cycle for incoming events immediately after the data are transferred from the onboard memory to the PC memory. In addition to the multi-thread design, the MFC code has exploited the capability of multiple record of the CompuScope card. In the Matlab code, data transfer from onboard memory to PC memory is executed after every data acquisition, which is single record mode. For example, every trigger will start the data transfer and 10 waveforms including 9 from pixel anodes and 1 from the cathode are transferred from the onboard memory to PC memory. Each waveform contains 512 samples and each sample takes 2 bytes of memory so the data size of each transfer is about 10kB, which is very small compared to the size of the onboard memory, 512MB. Since it takes time to start and stop the data transfer, it is not efficient to operate the system in single record mode. The CompuScope card allows the storage of a certain number of events before transferring to the PC memory, which is called multiple record mode. The number of events is only limited by the onboard memory and this mode is very useful for continuous trigger operation [54]. Fig. 2.16 shows the graphic user interface of the data acquisition code. The left part can display the real time waveforms and raw spectrum and the settings can be changed in the right part.

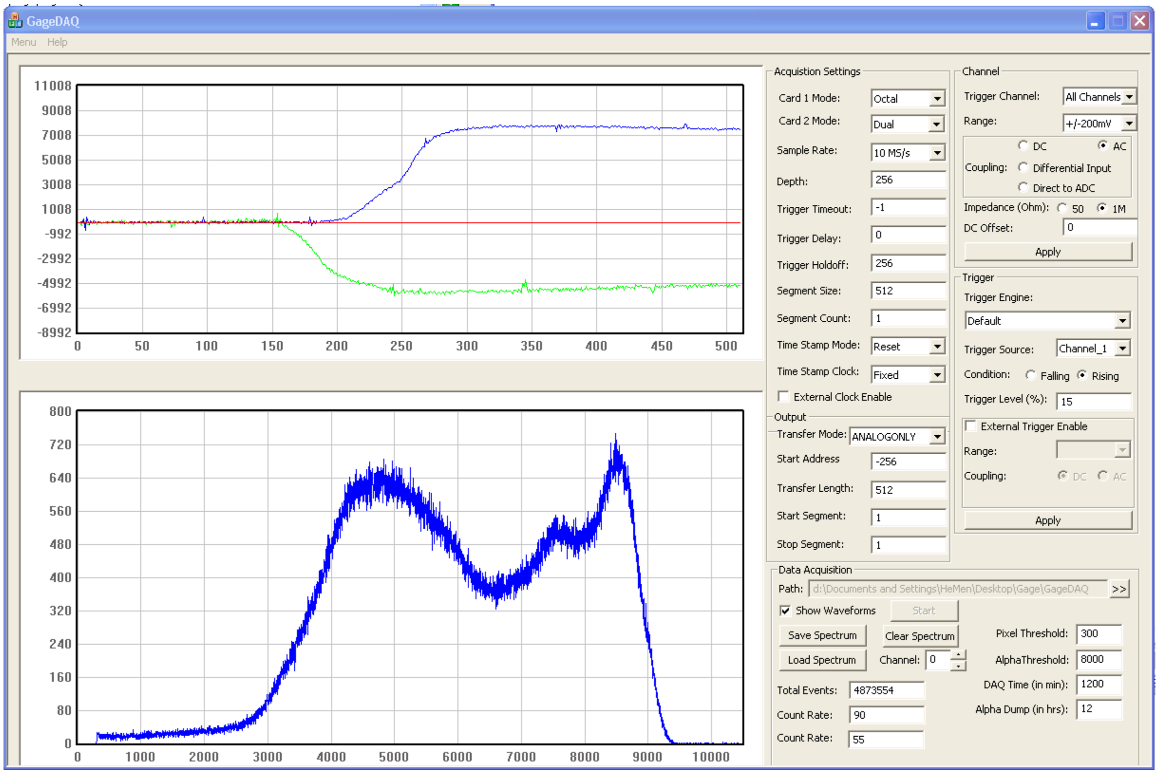

Acquistion Settings
Card 1 Mode: Octal
Card 2 Mode: Dual
Sample Rate: 10 MS/s
Depth: 256
Trigger Timeout: -1
Trigger Delay: 0
Trigger Holdoff: 256
Segment Size: 512
Segment Count: 1
Time Stamp Mode: Reset
Time Stamp Clock: Fixed
☐ External Clock Enable

Output
Transfer Mode: ANALOGONLY
Start Address -256
Transfer Length: 512
Start Segment: 1
Stop Segment: 1

Channel
Trigger Channel: All Channels
Range: +/-200mV
Coupling: ○ DC ● AC ○ Differential Input ○ Direct to ADC
Impedance (Ohm): ○ 50 ● 1M
DC Offset: 0

Trigger
Trigger Engine: Default
Trigger Source: Channel_1
Condition: ○ Falling ● Rising
Trigger Level (%): 15
☐ External Trigger Enable
Range:
Coupling: ● DC ○ AC

Data Acquisition
Path: d:\Documents and Settings\HeMen\Desktop\Gage\GageDAQ
☑ Show Waveforms
Channel: 0
Total Events: 4873554
Count Rate: 90
Count Rate: 55
Pixel Threshold: 300
AlphaThreshold: 8000
DAQ Time (in min): 1200
Alpha Dump (in hrs): 12

Figure 2.16: Graphic user interface of the data acquisition code based on MFC platform

2.3 Conclusion

This chapter summarizes two readout systems, digital ASIC array system and CompuScope card system. Both systems are capable of providing the digitized samples of the pre-amplifier signal waveforms. The electronic noise for single-pixel and multiple pixel events on the digital ASIC array system has been discussed. The common noise is found in full readout mode and able to be removed with the common mode noise correction algorithm. The advantage and limitation of CompuScope Gage digitizer used for TlBr detectors is discussed and the advanced data acquisition code based on MFC platform is introduced. Since a radiation detection system includes a readout system and a detector, the next chapter will focus on the active detection volume of the CdZnTe detectors used in this study.

CHAPTER III

CdZnTe Detector and Relative Efficiency

Excellent energy resolution has been demonstrated on large volume CdZnTe detectors. The best recorded energy resolution for single-pixel events within a 20×20×15 mm^3 pixelated CdZnTe detector was found to be 0.48% FWHM at 662 keV fabricated by eV-Products. In order to increase crystal yield and reduce the cost, different crystal growing methods have been developed by different CdZnTe vendors. Instead of High Pressure Bridgman(HPB) method used by eV-Products, Traveling Heater Method(THM) has been adopted by Redlen Technology. After several years of effort, the spectroscopic performance of Redlen detectors is very close to the best eV-Products detectors. However, good energy resolution does not necessarily indicate a fully active detection volume. In order to study the active detection volume of CdZnTe detectors, Dr. Feng Zhang designed the relative efficiency experiment and used the relative efficiency as an indicator of the active volume of the detectors. The relative efficiency is defined as the ratio of the detection efficiency of an experiment and its corresponding simulation. According to the result, the active volume of eV-Products CdZnTe detectors is more than 90%. In order to measure the active volume of Redlen detectors, a similar experiment was performed. A Geant4 simulation including the basic geometry of the detector box was used as well.

3.1 Experiment

3.1.1 Detector and ASIC

Experiments were performed on three 20×20×15 mm^3 pixelated CdZnTe detectors with a common grid between 11×11 pixels shown in Fig. 3.1. One of them was fabricated by eV-Products and the other two were from Redlen Technologies. They are named as 4E3, 4R16 and 4R33 respectively. The 11×11 anode pixels and common grid configuration are shown in Fig. 3.1(c). The pixel pad size is 1.22 mm and the two adjacent pads are separated by two 0.2 mm wide gaps and one 0.1 mm wide grid. Therefore, the size of each pixel pitch is 1.72 mm. The H3Dv2 Application Specific Integrated Circuit (ASIC) readout system developed by Brookhaven National Laboratory(BNL) was used. This ASIC has 130 channels, including 128 channels for anode pixels, 1 channel for the common grid and 1 channel for the cathode. Each channel can provide timing and amplitude information. The ASIC was operated in full readout mode so that all 130 channels were read out if any pixel is triggered. The ASIC chip is shown on Fig. 3.1(d).

Table 3.1: Activities of three gamma-ray sources used in the experiment

	^{241}Am	^{137}Cs	^{60}Co
Activity(μCi)	9.77	6.30	1.11
Uncertainty	±4%	±4%	±3%

Three un-collimated radiation sources including ^{241}Am, ^{137}Cs, and ^{60}Co were used to obtain the detection efficiency at different energies. Their activities at the time of the experiment are shown in Table 3.1. These sources were placed on the top of the detector box about 5 cm above the cathode side. The detector box was put on top of a lab bench which is about 5 feet above the floor and 3 feet away from the wall in order to reduce the back-scattering gamma-ray background. The inside of the detector box, without a cathode high voltage bias distribution board, is shown in Fig. 3.2. The cathode was biased at -3000 V in order to drift the electron-hole pairs. The common grid bias varies from detector to detector due to different material properties. In this experiment, the steering grids of two Redlen detectors were biased at -150 V and -180 V respectively while the eV-Products detector grid bias was set at -40 V. In order to provide sufficient steering effect for them, higher grid biases are needed on the two Redlen detectors.

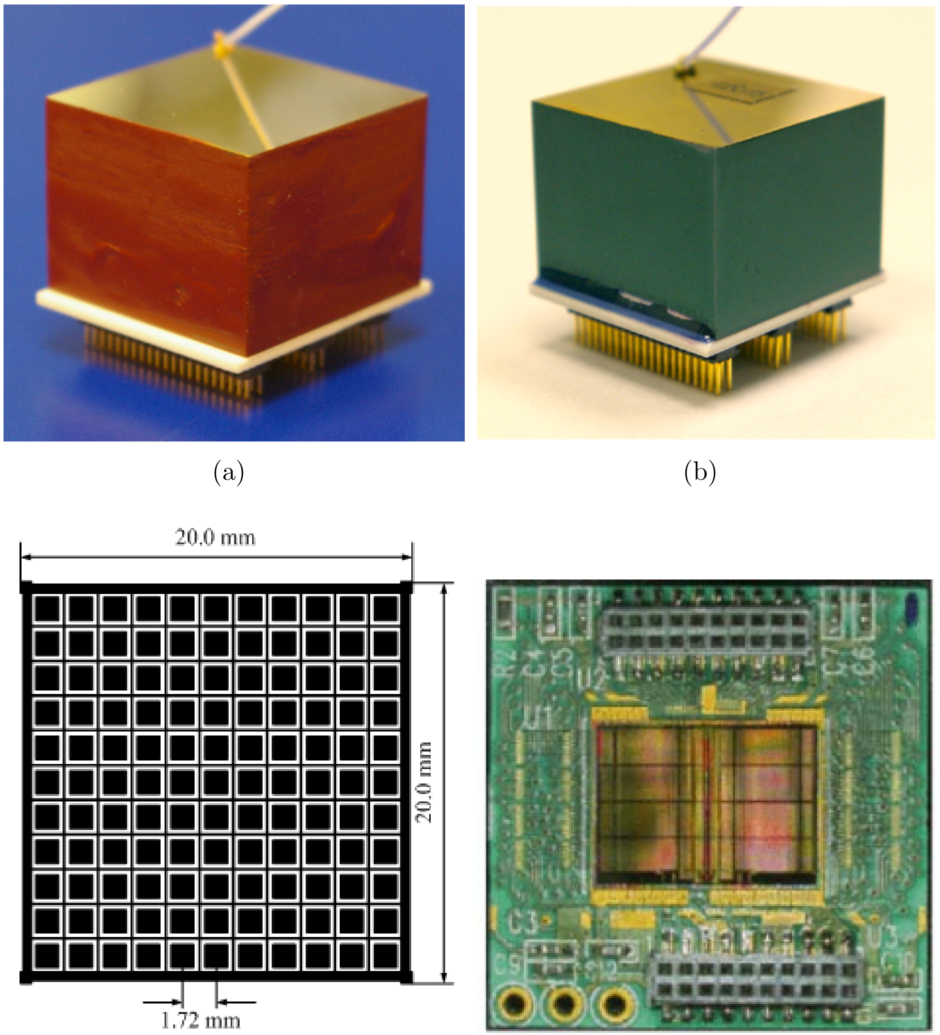

(a) (b)

(c) (d)

Figure 3.1: Detectors and the anode electrode configuration (c). eV-Products Detector (a) and Redlen Detector (b) are shown on the top. The bottom right is the BNL H3Dv2 ASIC (d). [4]

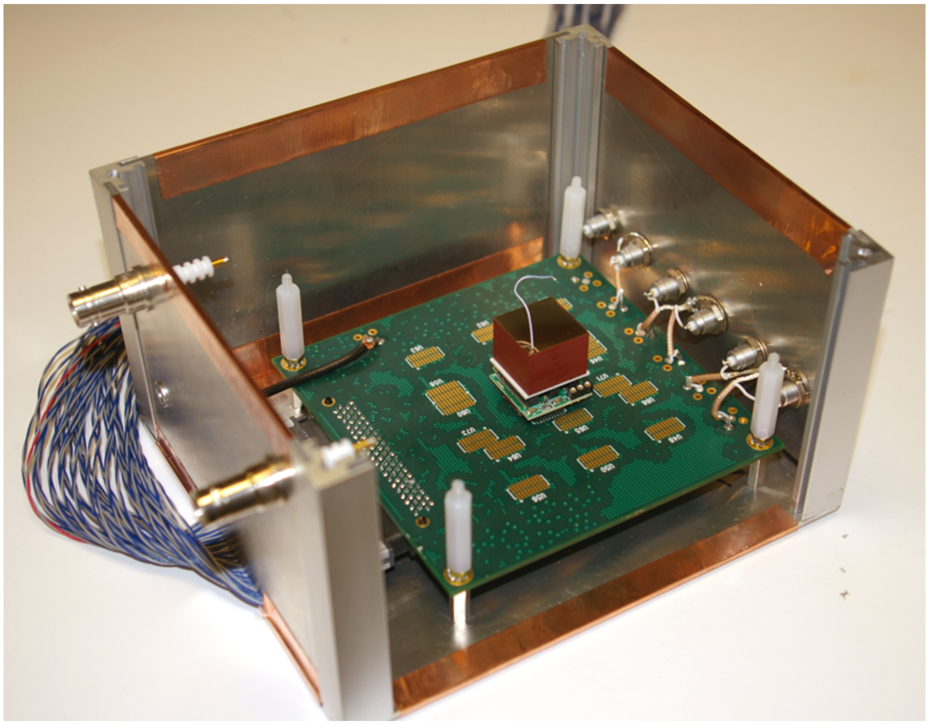

Figure 3.2: One assembled detector module plugged on the motherboard in the detector box. [4]

3.1.2 System Dead Time

In an ideal world, the detector system should be able to detect two separate events within an infinitely small time interval. However, in reality, all detector systems require a minimum time separation of two events. This minimum time interval is the system dead time, during which the system cannot register the next incoming gamma ray as a new event. Due to the random nature of incident gamma rays, it is possible that a true event will be missed because it is not separated enough in time from the previous event. In order to measure the detection efficiency, the system dead time has to be considered. In this experiment, a nonparalyzable system response model was used. The true interaction rate can be calculated via Eq. 3.1 [10], where n is the true interaction rate, m is the recorded count rate and τ is the system dead time.

$$n = \frac{m}{1 - m\tau} \tag{3.1}$$

The system dead time was measured using the ASIC internal test pulse. By increasing the test pulse frequency until the system cannot resolve two adjacent test pulses, the system dead time can be approximated by the inverse of that maximum test pulse frequency. Although the test pulse has a slightly different pulse shape than the gamma interaction pulse, it should still be an accurate estimate of the dead time. Through this method, the system dead time was measured to be 118μs. With the ^{137}Cs source, the average recorded count rate was 1268 cps. Using Eq. 3.1, the true interaction rate was calculated to be about 1491 cps. The true interaction rate of ^{241}Am and ^{60}Co was calculated in a similar way.

3.1.3 Background Subtraction

All radiation detectors record some background signal due to the cosmic radiation from space and the existence of natural radioactivity in the environment. For example, in this experiment, the CdZnTe detector had a count rate about 22 cps without any lab sources nearby so these events were not from the source. Since the detection efficiency is defined as

$$\text{Detection Efficiency} = \frac{\text{number of pulses recorded}}{\text{number of radiation quanta emitted by source}}, \tag{3.2}$$

the detection efficiency will be overestimated if the background counts are not removed. Therefore, the background was also measured for each detector. Since the count rate of background radiation was very low, a long measurement time was required to achieve reliable statistics. The background count rate does not change significantly over time in our laboratory, so one background measurement can be used for all three sources for each detector. The background counts were normalized to the measurement time of each source and subtracted from the source spectra.

3.2 Simulation

3.2.1 Physics Process Model

The gamma-ray interaction and electron ionization was simulated using Geant4.9.0[1]. A simplified detector box geometry was modeled, including the aluminum box with 2.0 mm thick walls, two PCB board representing the high voltage supply board and the motherboard, and one CdZnTe detector, shown in Fig. 3.3. The isotropic gamma-ray point source was placed on top of the detector box and 5.2 cm above the cathode surface of the detector. Weighting potential was generated by Maxwell and calculated along the centerline of the collecting pixel. Since the weighting potential variation within one pixel should not affect detection efficiency, the weighting potential was used for all sub-pixel positions. The weighting potential crosstalk was also not included in the model to simplify the simulation and there is no impact on detection efficiency.

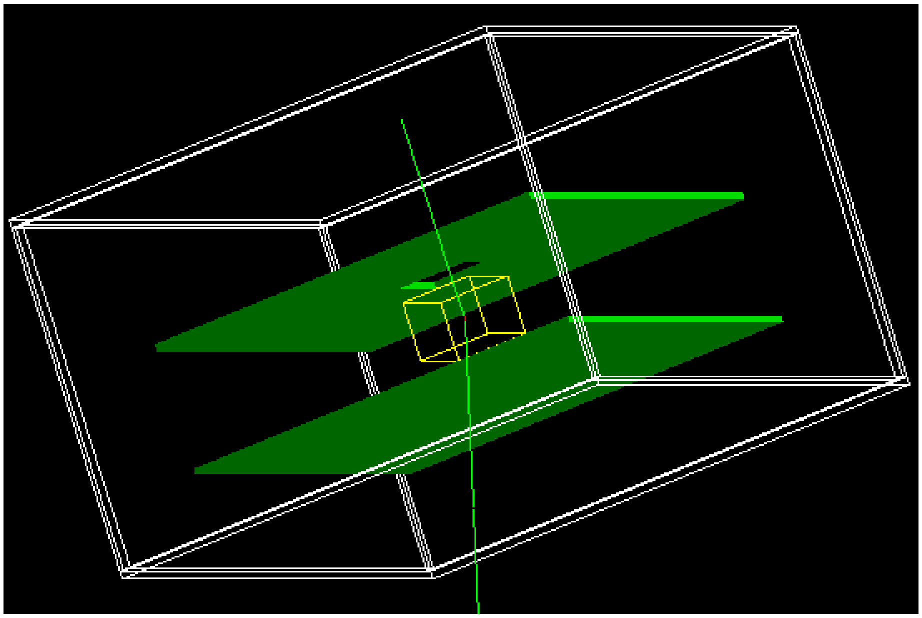

Figure 3.3: Detector box geometry in simulation.

---

[1] CERN, Geant4. 2003: Geneva, Switzerland

3.2.2 Electron Cloud Diffusion

After the electron-hole pairs are generated, they will drift in opposite directions, driven by the electric field; electrons towards the high potential and holes towards the lower potential. Since the mobility of holes is more than ten times smaller than that of electrons in CdZnTe detectors, the holes can be considered stationary throughout the charge collection time. Due to random thermal motion, the electrons usually diffuse away from their point of origin. In the Geant4 simulation, the gamma-ray energy was deposited along the track of the secondary electron and there are many energy deposition sites along the track. These energy deposition sites were used as the initial electron cloud distribution. However, in reality, the electrons have a broadened distribution due to the diffusion. Therefore, the electron cloud diffusion has to be modeled. The cross section of this distribution can be approximated by a Gaussian function [10],

$$\sigma = \sqrt{2Dt} \tag{3.3}$$

where σ is the standard deviation, D is the diffusion coefficient and t is the elapsed time. The diffusion coefficient D can be calculated via Eq. 3.4 [10],

$$D = \mu \frac{kT}{e} \tag{3.4}$$

where μ is the mobility of electrons, k is the Boltzmann constant, T is the absolute temperature and e is the unit charge. In the diffusion model, the internal electric field,E, of the CdZnTe detector was assumed to be uniform, which lead to constant drift velocity, v, since $v = \mu E$. Therefore, the elapsed time can be calculated by

$$t = \frac{x}{v} = \frac{x}{\mu E} \tag{3.5}$$

where x is the drift distance. Combining Eqs. 3.3, 3.4 and 3.5, the standard deviation due to the diffusion can be predicted from

$$\sigma = \sqrt{\frac{2kTx}{eE}} \tag{3.6}$$

In the experiment, the size of the CdZnTe detector is 20×20×15 mm^3 and it was biased at -3000 V. Thus, the maximum value of x is 15 mm and E is equal to 200 V/mm. According to Eq. 5.1, at room temperature, the standard deviation σ is about 62 μm. To simplify the model, the shape of electron cloud was assumed to be square with a side length of 2.35 σ and the charge was uniformly distributed over the square.

3.2.3 Readout Electronics and Detector Pixelation

Since the readout circuitry only contributes to the energy resolution, not the detection efficiency, the pre-amplifiers and slow shapers were not modeled. The signal induction was simply calculated using the Shockley-Ramo theorem and 1% energy resolution at 662 keV uncertainty was added to represent all the electronic noise. The triggering mechanism was simulated with a constant threshold at 40 keV. Any pixel with an energy deposition of more than 40 keV will be registered as a valid event. The pixelation was also included since the electron cloud has a finite size and it will change the fractions of single-pixel events and multiple pixel events. The size of a pixel pitch was set at 1.72 mm. A 20 keV software threshold was used to check how many pixels have true induced signals above it after the initial trigger. This feature also helps determine an event to be a single-pixel event or multiple pixel event.

3.3 Results

Fig. 3.4 shows the measured and simulated spectrum for events from the ^{137}Cs source. The overall energy resolution for both spectra was about 1%. The simulated

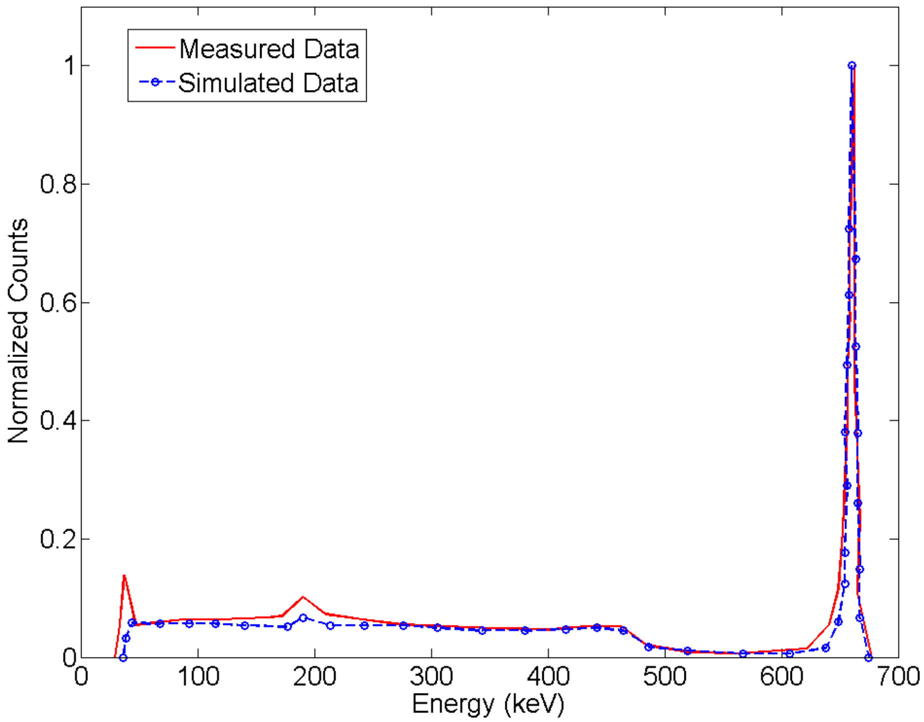

Figure 3.4: Measured (4E3) and Simualted spectrum for ^{137}Cs source. The counts are normalized to their maximum peak counts respectively.

spectrum has all the features the measured spectrum does except the tiny peak around 35 keV. This peak could be caused by the characteristic x-rays from the ^{137}Cs source. A similar peak was shown in Fig. 2.7 as well. Since these x-rays were not considered in the simulation, the peak did not show up in the simulated spectrum. Therefore, the energy window used to calculate total efficiency for ^{137}Cs was chosen from 50 keV to 700 keV to avoid the contribution of these X-rays. Besides the characteristic x-ray peak, the backscatter peak was also more prominent in measurement than that in simulation, which is likely due to the absence of the walls and floor surrounding the detector in the simulation. Other than these discrepancies, the simulation model worked as expected without significant model mismatch.

Fig. 3.5 and Fig. 3.6 are the simulated and measured absolute photopeak efficiency for three detectors. As expected, the absolute photopeak efficiency decreases when the energy of the incident gamma rays increases. This also proves that the physical process model was correct in the simulation since the cross section for high energy gamma-rays is smaller than low energy gamma rays. The efficiency for the 59.5 keV gamma rays from ^{241}Am in detector 4R16 is smaller than that in the other two detectors due to its higher electronic noise. In order to reduce the noise trigger rate, the trigger threshold in 4R16 was set higher than the other two detectors. Since the detection efficiency is very sensitive to the triggering threshold for low energy gamma rays, the threshold in the simulation was also set higher for 4R16 than the other two detectors. In order to minimize the statistical uncertainty, more than a million events were used for every source and every detector. Therefore, the error bars for both simulation and measurement were very small. Since the activities of three sources had uncertainty around 3%, they became the major contributors to the uncertainties of the relative efficiencies. For a fair comparison, the activity uncertainty was not included in either Fig. 3.5 or Fig. 3.6 since it was not considered when the point source in the simulation was designed. However, the activity uncertainty was included in the relative efficiency calculation.

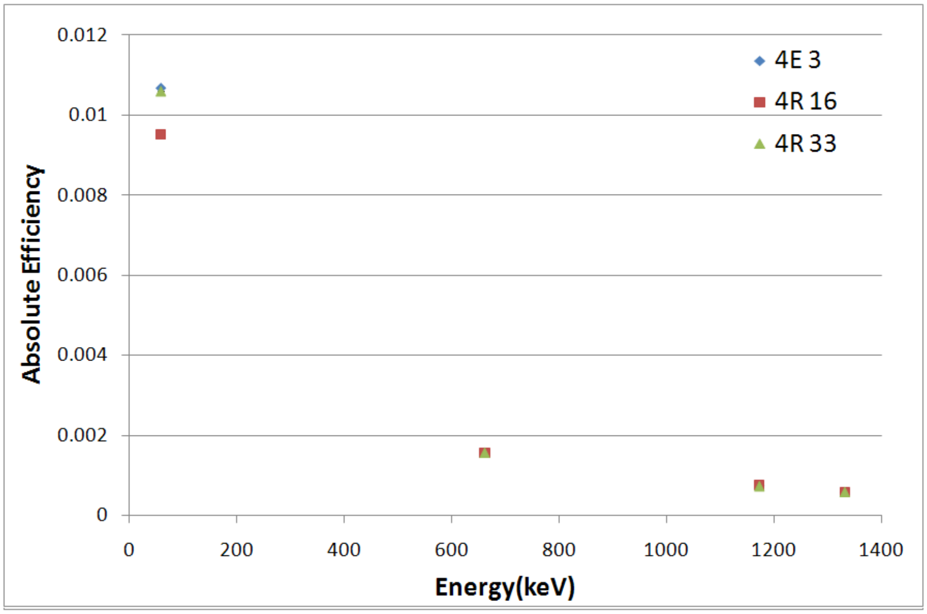

Figure 3.5: Simulated photopeak efficiencies for three detectors

If the detector bulk is fully active, the relative efficiency should be 1.0. The overall

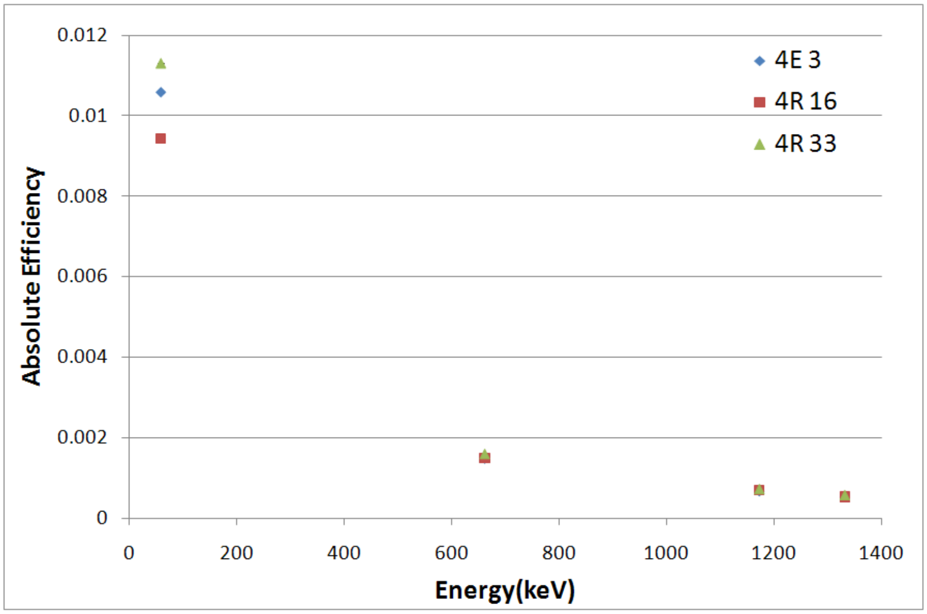

Figure 3.6: Measured photopeak efficiencies for three detectors

relative efficiencies for three detectors at different gamma-ray energies are shown in Table 3.3. As seen in Table 3.3, for the ^{241}Am, the relative efficiency is very close to 1.0 for all three detectors, which indicates that there is no inactive layer at the cathode side of each detector since the mean free path for 59.5 keV gamma-rays in CdZnTe detectors is smaller than 1 mm. For higher energy gamma-rays, the absolute efficiency for total counts agrees with the simulation while the photopeak efficiency has a 5-10% deficit. This means that the missing photopeak events ended up in the Compton continuum. Dr. Feng Zhang had investigated several possible reasons, including the dead layer region near the anode side and electron trapping in the gap between pixel anodes and the steering grid electrode or underneath the steering grid. The most probable reason for the loss of photopeak events is the incomplete charge collection in the peripheral pixels of the detector. Since the weighting potential of the edge pixels and the side surface trapping were not considered, the incomplete charge collection events were underestimated in the simulation model. This has been verified by the incomplete charge collection events identification algorithm. The detailed algorithm will be presented in Chapter V. The result shows that about 10% of single-pixel events were incomplete charge collection photopeak events. Since 35% of the events were single pixel events for 662 keV gamma rays, the missing photopeak events were about 3 to 4%. Adding these events back to the photopeak region will make the relative efficiency of ^{137}Cs close to 1.0. The gamma-ray energies of ^{60}Co are higher so the electron cloud size is bigger and the average number of interactions is greater than the 662 keV gamma-rays from ^{137}Cs. Therefore, the fraction of incomplete charge collection events will be higher for ^{60}Co than that for ^{137}Cs (detailed analysis see page 91 of Chapter V).

Table 3.2: Relative efficiency (measured efficiency/simulated efficiency) of total counts and photopeak counts for three detectors at different gamma-ray energies.

Sources	^{241}Am	^{137}Cs		^{60}Co		
Detector	Photopeak	Total	Photopeak	Total	Photopeak	Photopeak
Energe Range (keV)	50-75	50-700	550-700	50-1400	1120-1230	1230-1400
4E3	0.99±4%	0.98±3%	0.95±4%	0.96±4%	0.92±3%	0.92±3%
4R16	0.99±4%	1.00±3%	0.96±4%	0.98±4%	0.92±3%	0.91±3%
4R33	1.07±4%	1.04±3%	1.02±4%	1.02±4%	1.00±3%	0.99±3%

Table 3.3: Relative efficiency (measured efficiency/simulated efficiency) of total counts and photopeak counts for three detectors at different gamma-ray energies.

Sources	^{241}Am	^{137}Cs	^{60}Co
4E3	99%	98%	96%
4R16	99%	100%	98%
4R33	107%	104%	102%

3.4 Conclusion

The active detection volume of three 20×20×15 mm^3 pixelated CdZnTe detectors was studied with the BNL-H3Dv2 ASIC readout system. A Geant4 simulation was developed to benchmark the absolute efficiency of the detector system. The relative efficiency, defined as the ratio of the measured efficiency and simulated efficiency, of all three detectors was very similar, which indicates the Redlen detectors have similar active detection volumes to eV-Products detector. The relative efficiency of 4R33 larger than the other two detectors may be due to different crystal sizes since each dimension of the detector has a 0.2 mm tolerance. The extra volume could easily increase the detection efficiency by a few percent. For all three detectors, the total efficiency is higher than the photopeak efficiency. This is caused by the incomplete charge collection events underneath the peripheral pixels and the most outside guard ring electrode. Since 10% of detection volume is underneath the guard ring electrode and events interacted in this region are more likely to be recorded as incomplete charge collection events, these incomplete charge collection events are not negligible. This photopeak efficiency loss could be reduced by using narrower guard ring electrode and changing the electric field near the side surface to steer the electrons toward the interior of the detector to minimize the trapping of electrons on the side surface. Overall result shows that the active detection volume of Redlen CdZnTe detectors is greater than 90% at multiple gamma-ray energies.

CHAPTER IV

Digital ASIC Array Nonlinearity

In a linear system, the input and output should follow the superposition principle $S(x_1 + x_2) = S(x_1) + S(x_2)$, where S is the output and x_1 and x_2 are the inputs. In order to fully calibrate such a system, only two sets of input and output responses are needed. After calibration, the system output response is predicted as long as the input is known. For instance, if a detector system has linear response, then the response for 1333 keV gamma rays should be approximately double the output for 661.7 keV gamma ray. However, it has been experimentally observed that the digital array system has a nonlinear response even after it was calibrated at 59.5 keV and 662 keV. This nonlinear response does not change the energy resolution of single-pixel events, but the photopeak centroid, or the energy of the incident radiation, will be recorded inaccurately. For multiple pixel events, this will degrade the spectroscopic performance significantly since energy depositions of the same incident energy may exhibit different responses. For example, a two-pixel event with 100 keV and 552 keV energy depositions will have a different recorded energy from one with 200 keV and 442 keV energy depositions even though both events have a total of 662 keV deposited. Since the digital ASIC array system has a dynamic range from 30 keV to 3 MeV, its nonlinearity has to be studied and calibrated for this energy range. In this chapter, the nonlinearity will be calibrated and the spectroscopic performance improvement will be presented.

4.1 Single-Module Single-Pixel Event Non-linearity

4.1.1 Baseline Offset Correction

In the analog ASIC system, the output signals have been observed to have some baseline offsets due to the peak hold drop, which means that the peak amplitude of the shaped signal cannot be held perfectly. However, in the digital ASIC system, the signal amplitude can be obtained via applying different digital filters directly to the preamplifier signals. Therefore, there is no peak hold circuitry involved and the issue of non-zero baseline offsets should no longer exist in the digital ASIC system. If the digital ASIC system has very good linearity, a two-point calibration with different gamma-ray energies should be able to fully calibrate the baseline offset for each pixel. A low gamma-ray energy, 59.5 keV from ^{241}Am, and a high gamma-ray energy, 662 keV from ^{137}Cs, were used in the calibration setup. In order to eliminate the trapping effect variation, only cathode side photopeak events were chosen for 662 keV gamma-rays since the interaction of 59.5 keV can only happen at the cathode side of the CdZnTe detector. Since there are 121 anode pixels and every pixel may have different baseline offsets, the 662 keV and 59.5 keV gamma-ray photopeaks were measured pixel by pixel. Fig. 4.1 shows the baseline offsets for all 121 anode pixels and most of the pixels have an offset around 1 keV. Compared to 3 MeV dynamic range, the offset is very insignificant.

4.1.2 Non-linear Response Observation

Since the assumption for the baseline correction is that the system is linear, the spectra for two sources can also be used for the energy calibration with the same assumption. The spectra of ^{241}Am and ^{137}Cs for one of the anode pixels are shown

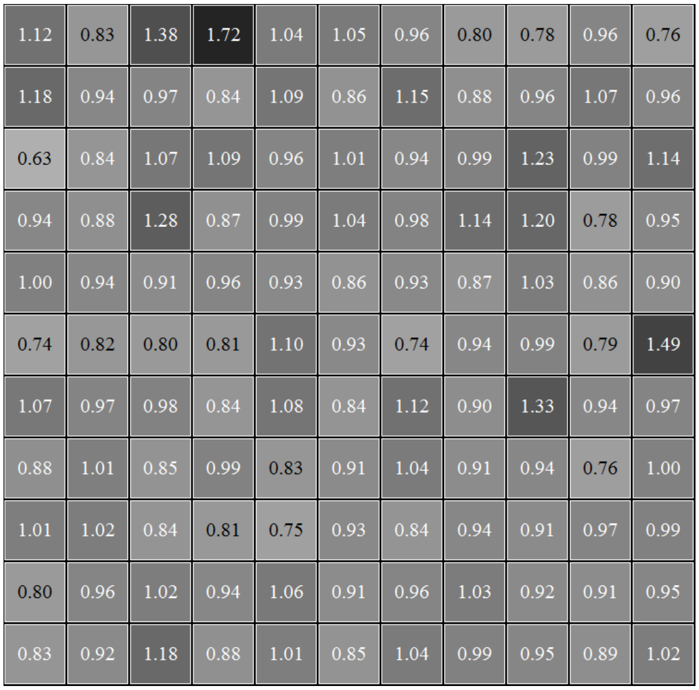

1.12	0.83	1.38	1.72	1.04	1.05	0.96	0.80	0.78	0.96	0.76
1.18	0.94	0.97	0.84	1.09	0.86	1.15	0.88	0.96	1.07	0.96
0.63	0.84	1.07	1.09	0.96	1.01	0.94	0.99	1.23	0.99	1.14
0.94	0.88	1.28	0.87	0.99	1.04	0.98	1.14	1.20	0.78	0.95
1.00	0.94	0.91	0.96	0.93	0.86	0.93	0.87	1.03	0.86	0.90
0.74	0.82	0.80	0.81	1.10	0.93	0.74	0.94	0.99	0.79	1.49
1.07	0.97	0.98	0.84	1.08	0.84	1.12	0.90	1.33	0.94	0.97
0.88	1.01	0.85	0.99	0.83	0.91	1.04	0.91	0.94	0.76	1.00
1.01	1.02	0.84	0.81	0.75	0.93	0.84	0.94	0.91	0.97	0.99
0.80	0.96	1.02	0.94	1.06	0.91	0.96	1.03	0.92	0.91	0.95
0.83	0.92	1.18	0.88	1.01	0.85	1.04	0.99	0.95	0.89	1.02

Figure 4.1: Baseline offsets of one digital ASIC in the array system for 11×11 pixel anodes. The unit is keV and the gray scale is from 0 to 2 keV.

in Fig. 4.2. With the known recorded energies and true energies for both sources, a linear fit can be calculated as the linearity response of this pixel as shown in Fig. 4.2 as well. Since the digital ASIC array system has a dynamic range up to 3 MeV, if the system has good linearity, this linearity calibration curve should be applicable to the entire dynamic range. In order to verify this, an experiment was performed with two sources, ^{137}Cs and ^{60}Co. The ^{137}Cs source was used to make sure that the system gain did not change and ^{60}Co would reveal the non-linear response if any existed. The spectrum of these two sources is shown in Fig. 4.3 and three photopeaks can be seen. Clearly, the 662 keV photopeak for ^{137}Cs is at the right energy while the measured photopeak centroids for ^{60}Co were not at expected energies. For the 1173 keV gamma-rays, the measured photopeak centroid is at 1181.8 keV, which is an 8.8 keV offset. The 1332 keV photopeak was measured at 1344.5 keV, which has 12.5 keV offset. Since the ^{137}Cs photopeak is at the correct energy, there should not be any reconstruction error or system gain shifting. Therefore, the energy offsets for higher

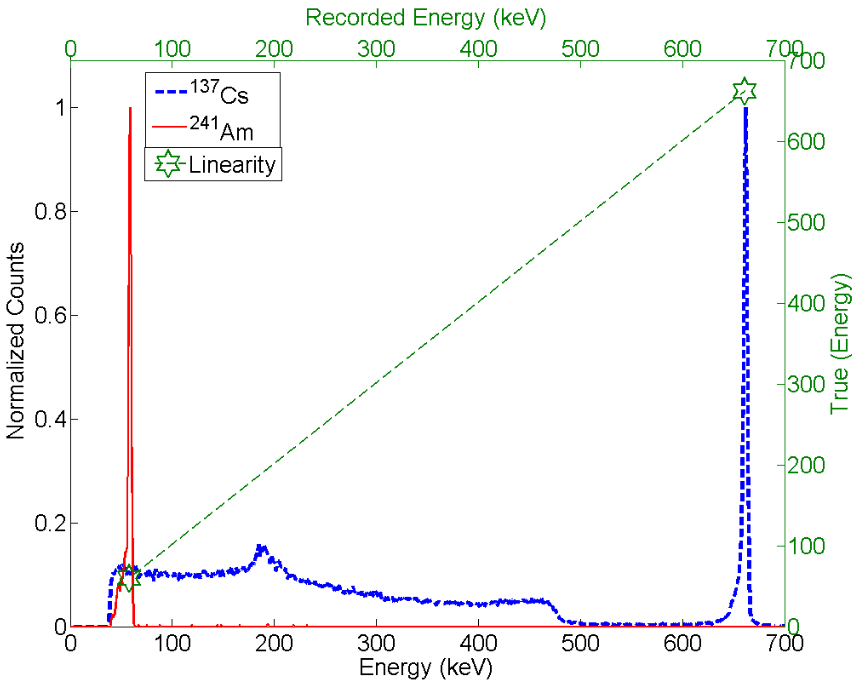

Figure 4.2: The cathode side events spectra for ^{241}Am and ^{137}Cs sources and the corresponding linearity calibration curve.

energy gamma-rays was due to the system non-linearity. This is a direct indication that the digital ASIC array system does not have perfect linear response.

4.1.3 Non-linearity Calibration

In order to correct the non-linear response of the digital array system, several gamma-rays sources were used to study the response of energy deposition over the whole dynamic range up to 3 MeV. In the experiments, ^{50}Co, ^{133}Ba, ^{22}Na, ^{60}Co, ^{152}Eu and ^{228}Th were used besides ^{241}Am and ^{137}Cs. Since there were many gamma-rays with different energies from those sources, only some of them were picked out for calibration. The major calibration lines are shown in Table. 4.1.

Table 4.1: Major gamma-ray energies used for non-linearity calibration

Source	^{241}Am	^{57}Co	^{133}Ba	^{60}Co	^{152}Eu	^{228}Th
Energy(keV)	59.5	122.1 136.5	81.0, 276.4, 302.9 356.0, 383.9	1173.2 1332.5	778.9, 964.1 1408.0	1592.5 2614.5

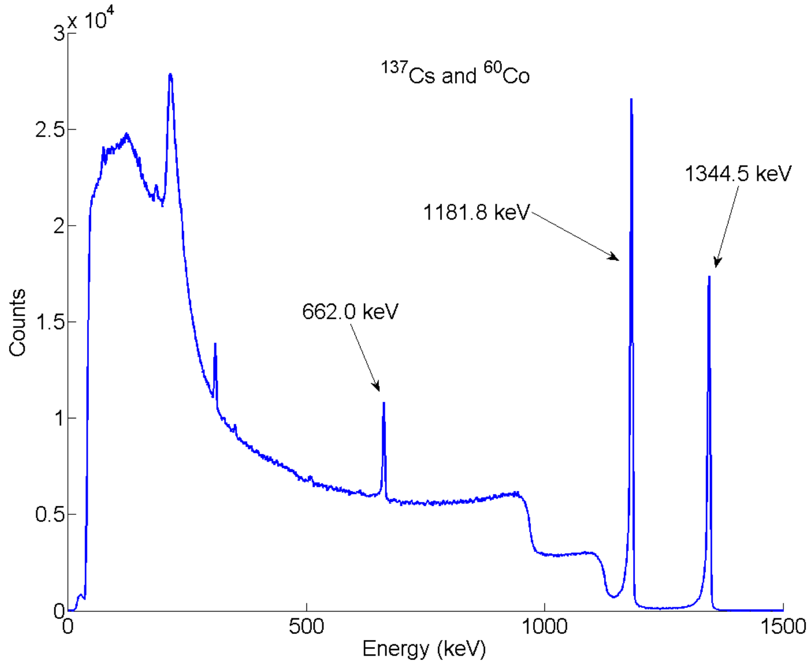

Figure 4.3: The spectrum for centroids of ^{137}Cs and ^{60}Co sources after applying the linearity calibration curve in Fig. 4.2

.

For every calibration experiment, the source was placed about 5 cm above the cathode surface so that all 121 pixels could see the low energy gamma rays. The detection efficiency of high energy gamma rays is significantly lower than that of low energy gamma rays. Therefore, in order to get enough photopeak counts on every pixel, the data collection time for high energy sources was much longer than that for low energy gamma rays. The detection efficiency of 2.6 MeV gamma rays from ^{228}Th was especially low, and the size of the electron cloud generated by these gamma-rays was comparable to the pixel pitch so there were not enough single-pixel photopeak events for pixel by pixel non-linearity calibration. Thus, for this energy, the overall single-pixel photopeak centroid was used for every pixel in order to have reliable statistics. In order to ensure this was a good approximation, the double escape peak of 2.6 MeV gamma rays at 1.6 MeV on each pixel were studied. The photopeak centroid variation is shown in Fig. 4.4. Each number stands for the photopeak centroid

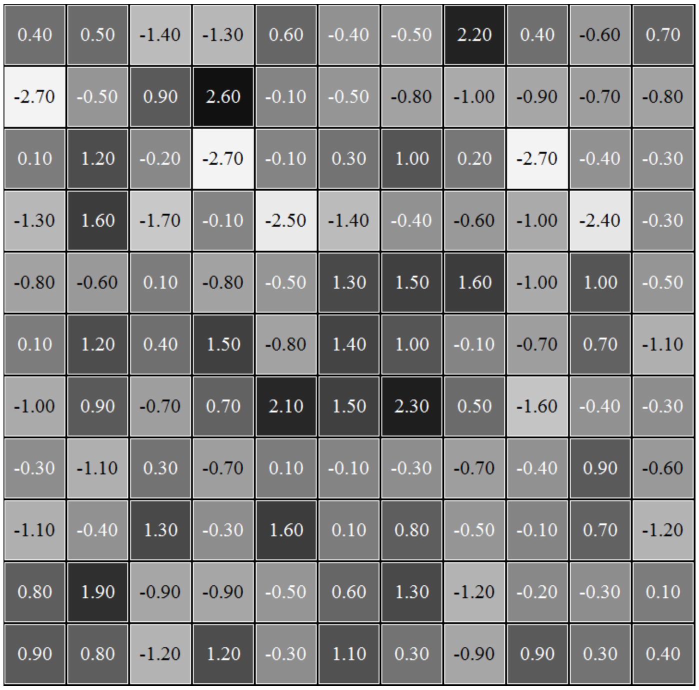

0.40	0.50	-1.40	-1.30	0.60	-0.40	-0.50	2.20	0.40	-0.60	0.70
-2.70	-0.50	0.90	2.60	-0.10	-0.50	-0.80	-1.00	-0.90	-0.70	-0.80
0.10	1.20	-0.20	-2.70	-0.10	0.30	1.00	0.20	-2.70	-0.40	-0.30
-1.30	1.60	-1.70	-0.10	-2.50	-1.40	-0.40	-0.60	-1.00	-2.40	-0.30
-0.80	-0.60	0.10	-0.80	-0.50	1.30	1.50	1.60	-1.00	1.00	-0.50
0.10	1.20	0.40	1.50	-0.80	1.40	1.00	-0.10	-0.70	0.70	-1.10
-1.00	0.90	-0.70	0.70	2.10	1.50	2.30	0.50	-1.60	-0.40	-0.30
-0.30	-1.10	0.30	-0.70	0.10	-0.10	-0.30	-0.70	-0.40	0.90	-0.60
-1.10	-0.40	1.30	-0.30	1.60	0.10	0.80	-0.50	-0.10	0.70	-1.20
0.80	1.90	-0.90	-0.90	-0.50	0.60	1.30	-1.20	-0.20	-0.30	0.10
0.90	0.80	-1.20	1.20	-0.30	1.10	0.30	-0.90	0.90	0.30	0.40

Figure 4.4: Photopeak centroid difference for 11×11 pixel anodes. The unit is keV and the gray scale is from -3 to 3 keV.

difference between that pixel and all pixels' spectrum. Clearly, the pixel by pixel photopeak centroid variation was not severe even for the 1.6 MeV gamma-ray peak and the maximum difference was no more than 3 keV. Therefore, that was a reasonable approximation to use the photopeak centroid of the overall spectrum as for each pixel for 2.6 MeV gamma-ray peak. If the pixel by pixel non-linearity needs to be accurately calibrated for the high energy gamma rays, the alternative way is to use a lab-made high activity Na-24 source, which emits gamma rays at energy of 2754 keV. In the following experiments, 2.6 MeV gamma rays from ^{228}Th were used and the centroid of the overall spectrum was applied to all pixels.

After conducting experiments with each of the sources in Table. 4.1, 16 true photopeak energies are known and their recorded energies on the digital ASIC system is also known, so the non-linearity can be thoroughly examined. Since the non-linearity behaves differently from pixel to pixel, the fitting is also done pixel by pixel. Fig. 4.5 shows the 3rd order polynomial fitting for one of the anode pixels. Each data point

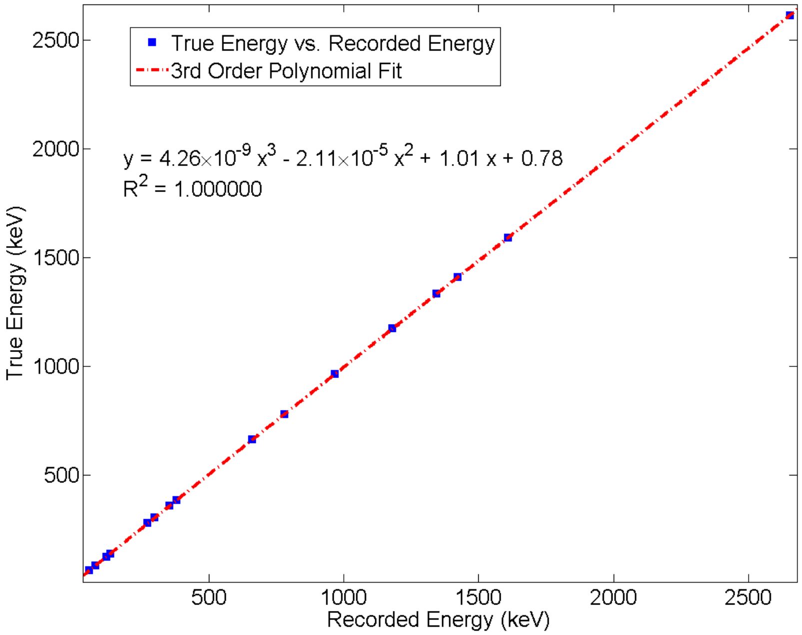

Figure 4.5: 3rd order empirical polynomial fitting for 16 measured photopeak centroids as the calibration of the non-linearity on one anode pixel over the entire dynamic range.

represents the photopeak centroid on that pixel except the last point, which is the photopeak centroid of the overall spectrum of 2614 keV. The overall non-linearity calibration performance is shown in Fig. 4.6. Clearly, the digital ASIC array system has a good linearity for energy below 1 MeV. However, when the energy deposition is above 1 MeV, it starts to show some significant energy offset. Especially for depositions of 1.6 MeV and above, the offset is more than 25 keV, which is more than 1% of the total energy deposition. The red curve shows that all the energy offsets are within 2 keV for the 16 energy lines after applying the non-linearity calibration.

Even though the red curve on Fig. 4.6 shows that the fitted energies are very close to the true energy, it does not mean the non-linearity calibration works since these peaks are from the calibration sources. In order to verify its performance, gamma rays with other energies besides the calibration lines should be used. There were two detectors used in this experiment and both of them were manufactured by Redlen,

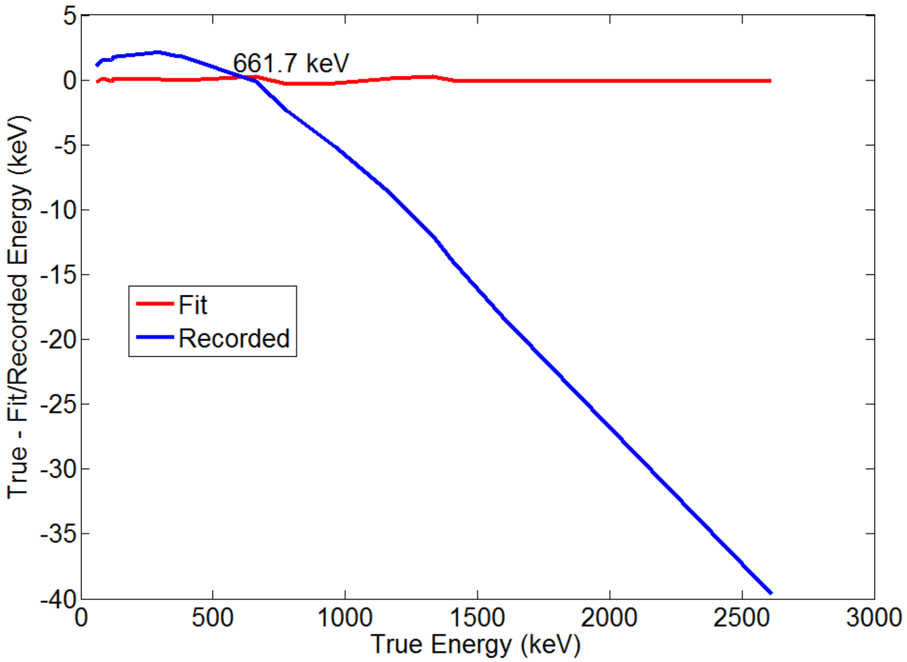

Figure 4.6: Overall non-linearity calibration performance for calibration energies

4R100 and 4R185. Since ^{152}Eu has many gamma-ray lines with different energies other than the three used in the calibration (see Table. 4.1), these gamma-rays can be used to test the performance of the non-linearity calibration. The non-linearity calibration performance is shown in Fig. 4.7. Both detectors have much smaller energy offsets after non-linearity reconstruction compared to the blue curve in Fig. 4.6 so this means that the empirical 3rd order polynomial fitting can represent the non-linear response of the digital ASIC array system. 4R100 has a narrower offset range than 4R185 since it exhibits better spectroscopic performance. The single-pixel energy resolution of 4R100 at 662 keV is 0.6% compared to 0.7% for 4R185. However, both detectors show the energy offset smaller than 2 keV after the non-linearity correction. Since ^{152}Eu does not have any energy lines above 1.4 MeV, ^{228}Th was used instead to verify the non-linearity correction performance for the higher gamma-ray energies. Fig.4.8 shows all the gamma-rays energies up to 2.1 MeV, the single escape peak of 2.6 MeV from ^{228}Th in 4R100. Clearly, after the non-linearity correction, the single-pixel photopeak energy offset can be limited within 2 keV through the whole dynamic

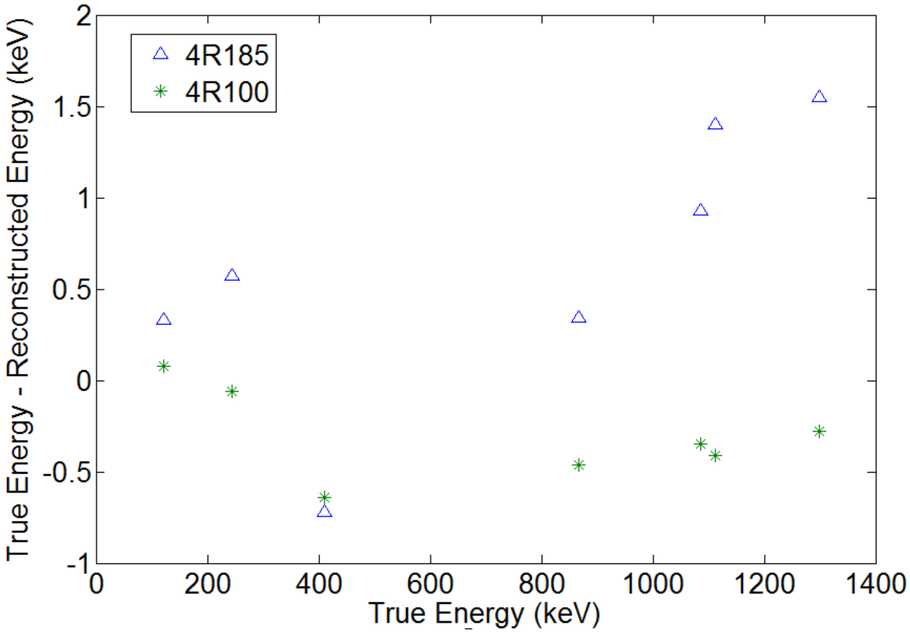

Figure 4.7: Overall non-linearity calibration performance for non-calibration energies for two Redlen detectors.

range of the digital ASIC array system.

4.2 Inter-Module Event Reconstruction

4.2.1 Non-linear Response Observation

Since there were two detectors populated in the digital ASIC array system, some gamma rays may deposit a portion of their energies in both detectors. If the gamma-ray interaction happens in more than one ASIC module, this type of event is classified as an inter-module events. If there is only one pixel triggered in each detector, the event is called an inter-module two pixel event. Even though they are only a fraction of inter-module events, they are very useful to study both the non-linearity of the system and the reasons of multiple pixel events energy degradation in single detector system.

An experiment was performed with a ^{137}Cs source above the cathode side of both detectors. The spectra for the single-module events and inter-module events are

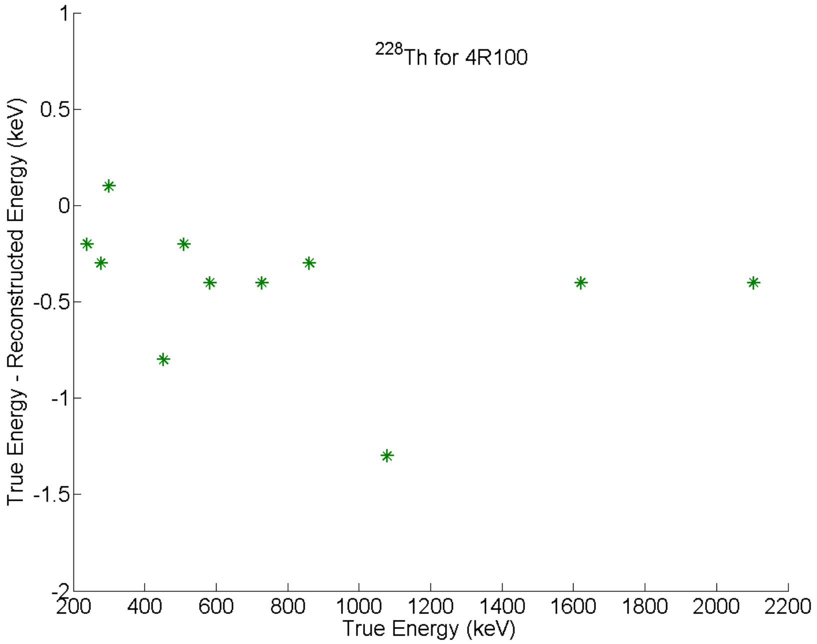

Figure 4.8: Overall non-linearity calibration performance for ^{228}Th in 4R100.

shown in Fig. 4.9. Clearly, the photopeak centroid of inter-module events is slightly smaller than the single-module events. The photopeak of inter-module events is at 657.7 keV while that of single-module events at 661.6 keV. The photopeak centroid has a deficit of about 4 keV, lower than expected. Since both detectors have very good energy resolution and inter-module two pixel events were calculated using C/A ratios, each individual energy deposition should be reconstructed correctly. Therefore, the photopeak centroid shift is very likely due to the system non-linearity. According to Fig. 4.6, when the energy deposition is around 300 keV, the system non-linearity will lead to a 2 keV energy offset. Since most inter-module two pixel photopeak events have average about 300 keV energy deposited in each detector, the sum of two energy deposition will inherently have about 4 keV energy offset, which is illustrated in Fig. 4.9. The same behavior has also been observed in the analog ASIC array system since it has non-linear response through its dynamic range. Thus, this is another indication that the digital ASIC array system has a non-linear response.

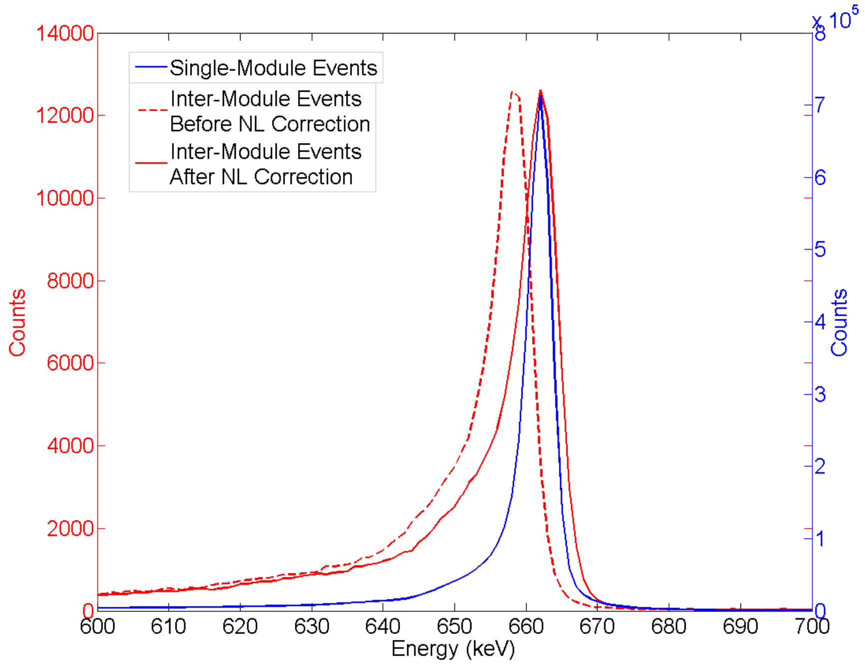

Figure 4.9: The photopeak centroid comparison between single-module events and inter-module events and the performance of non-linearity correction on inter-module events.

4.2.2 Non-linearity Correction

In order to correct the energy shift of these inter-module two pixel events, the non-linearity calibration was applied to each individual energy deposition. The spectrum of inter-module events after non-linearity correction is shown in Fig. 4.9. The photopeak centroid is corrected from 657.7 keV to 661.6 keV. The FWHM of inter-module events is greater than that of the single-module single-pixel events due to the electronic noise summed from two pixels.

Fig. 4.9 only illustrates the performance of non-linearity at one particular energy (661.7 keV). In order to fully evaluate the overall non-linearity calibration for inter-module two pixel events, the ^{152}Eu source was used since it has many gamma-ray energies up to 1.4 MeV. To simplify the analysis, only single-pixel events and inter-module two pixel events were selected because single-module multiple pixel event reconstruction requires weighting potential cross talk correction, which may not help

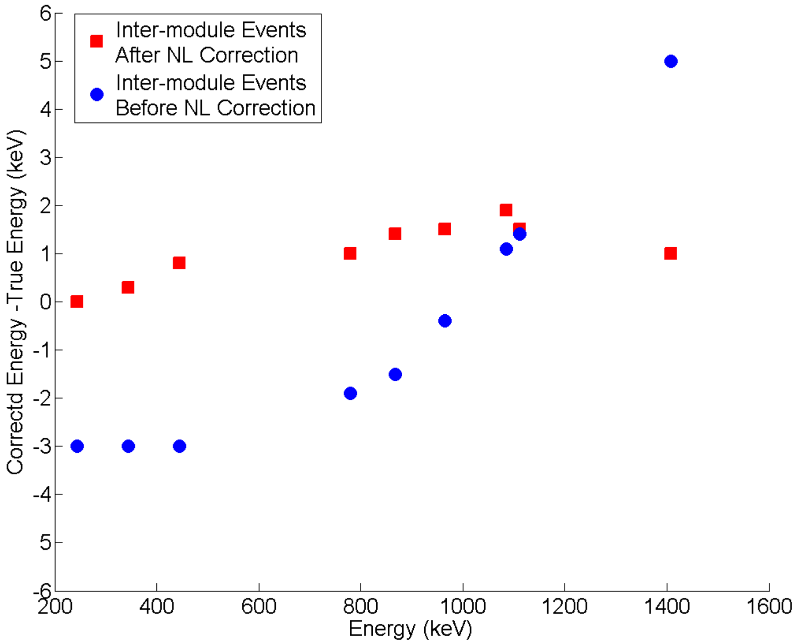

Figure 4.10: The non-linearity correction performance on inter-module two pixel events of ^{152}Eu source spectrum.

reveal the non-linearity correction. The weighting potential cross talk correction will be discussed in the single-module two pixel event non-linearity section. There are 9 energy lines used from ^{152}Eu, 224.7, 344.3, 444.0, 778.9, 867.4, 964.1, 1085.9, 1112.1, and 1408 keV. Fig. 4.10 shows that the non-linearity correction performance on these 9 energy lines. The blue dots show that before non-linearity correction, the photopeak centroid of high energy gamma rays can be off by 5 keV. However, after the non-linearity correction, the difference between correct energy and true energy is no more than 2 keV. Therefore, the non-linearity calibration generated from the single-module single-pixel events have proven to be useful. Interestingly, when the gamma-ray energies are around 1200 keV, the inter-module two pixel event photopeak does not have significant offset. The reason is very simple. when the gamma-ray energies are around 1200 keV and split in 2 detectors, their individual energy deposition is around 600 keV on average. Since the system is calibrated at 662 keV, when the energy deposition is around 662 keV, the non-linearity does not have significant effect. According to Fig. 4.6, the energy deposition smaller than the calibration energy will have a negative offset while the other one greater than 661.7 keV will have a positive offset. The overall effect of non-linearity is canceled out due to this. Therefore, gamma-ray energies around 1200 keV do not show significant offset even without non-linearity correction.

4.2.3 Inter-module Chance Coincidence Events

According to Fig. 4.9, the energy resolution of the inter-module two pixel events at 662 keV is 1.03% before the non-linearity correction and 1.02% after. It seems that the non-linearity correction does not improve the energy resolution for two pixel events. However, the inter-module two pixel event reconstruction does not include any weighting potential cross talk correction, which could be affected by non-linearity correction. This will be discussed in the next section. The two pixel event energy resolutions of 4R100 and 4R185 are 0.97% and 1.18% respectively. The inter-module two pixel event energy resolution is better than that of 4R185 because the system noise of 4R100 is better than 4R185 and part of the energy deposition is in 4R100 for the inter-module events. Nevertheless, the inter-module two pixel event reconstruction only involves C/A depth correction so the energy resolution of these events should follow the quadrature sum principle if there is no cross-talk noise between modules.

Since the energy deposition in each detector will vary from event to event and the energy resolution changes over different energy depositions, inter-module two pixel events at 662 keV are not the best candidate to study the energy resolution degradation. Therefore, an experiment with ^{133}Ba was performed. The spectra of ^{133}Ba for single-pixel events and inter-module events are shown in Fig. 4.11. Clearly, the spectrum of inter-module two pixel events has two more peaks than that of single-pixel events, which are highlighted in green dashed box. Those events are chance coincidence events from two different gamma rays. The lower peak is chance coincidence

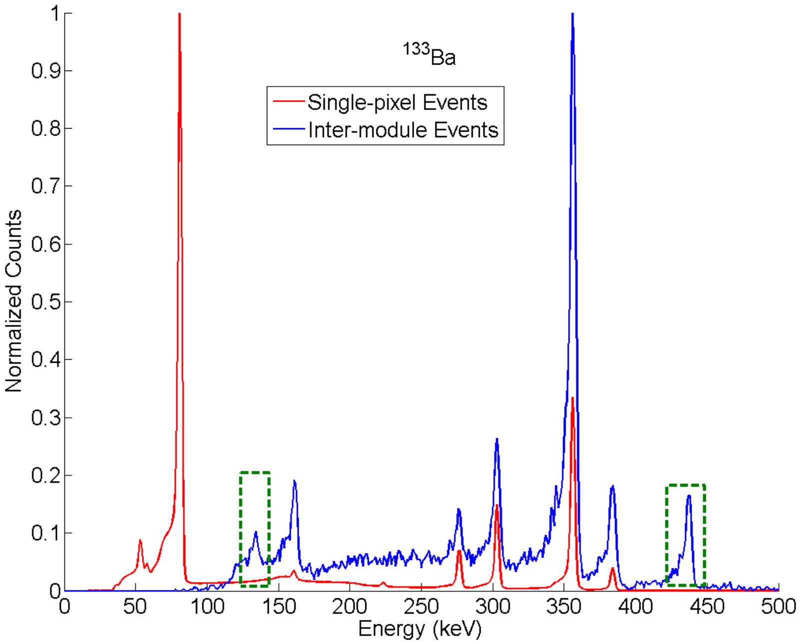

Figure 4.11: The photopeak centroid comparison between single-module events and inter-module events and the performance of non-linearity correction on inter-module events.

events from 53 keV and 80 keV while the higher peak is the chance coincidence events from 80 keV and 356 keV. There are not sufficient events to calculate the FWHM of the lower peak therefore the 436 keV chance coincidence peak is selected to verify the existence of cross-talk noise between modules. There are about 3500 events underneath that peak and the FWHM of the peak s 4.93 keV. From the single-pixel event spectrum, the FWHM of 80 keV and 356 keV are estimated to be 3.24 keV and 3.63 keV. According to the quadrature sum principle, the FWHM of the coincidence peak should be around 4.87 keV. It is very close to the measured FWHM, which indicates that there is no significant cross-talk noise over different ASIC modules which could degrade the spectroscopic performance. Therefore, the single-module multiple pixel event energy resolution degradation is due to imperfect weighting potential cross-talk correction, non-linear response and errors of drift time to C/A ratio conversion. The next section will focus on the energy resolution improvement of single-module multiple pixel events with the non-linearity correction and modified weighting potential cross-talk correction.

4.3 Single-Module Multiple Pixel Event Reconstruction

4.3.1 Multiple Pixel Event Energy Resolution Degradation

It has been experimentally observed that the single-module multiple pixel event energy resolution degrades faster than the quadrature sum predication from single-pixel events energy resolution. Multiple pixel event reconstruction is not as simple as that of single-pixel since it involves the drift time to C/A ratio conversion, weighting potential cross-talk, non-linearity, incomplete charge collection etc. In order to find the primary factor of the energy resolution degradation, the data of detector 4R100 from the inter-module experiment was used. Detector 4R100 is a very good detector with single-pixel energy resolution 0.6% FWHM at 662 keV. However, two pixel events energy resolution degrades to 0.96% FWHM without non-linearity correction. If the multiple pixel event reconstruction was perfect, the quadrature sum principle should give a two-pixel event energy resolution around 0.82%. Table. 4.2 shows the overall spectroscopic performance of detector 4R100. The non-linearity correction does not change the energy resolution of single-pixel events while it improves that of multiple pixel events. Moreover, with the non-linearity correction, the energy resolution of multiple pixel events are closer to the quadrature sum predication.

Table 4.2: Spectroscopic performance of 4R100

	1-pixel	2-pixel	3-pixel	4-pixel	Overall
Before NL Correction	0.57%	0.96%	1.23%	1.53%	0.81%
After NL Correction	0.58%	0.87%	1.14%	1.43%	0.76%
Quadrature Sum	-	0.82%	1.00%	1.16%	-

4.3.2 Drift Time to C/A Ratio Conversion

For single-pixel events, the depth reconstruction relies on the C/A ratio. However, for multiple pixel events, the C/A ratio does not tell the individual interaction depth any more. Therefore, the depth correction has to depend on the measurement of the drift time. In order to convert the drift time to C/A ratio, single-pixel photopeak events are used to create a drift time to C/A ratio mapping, which can be applied to multiple pixel events. The mapping of detector 4R100 is shown in Fig. 4.12.

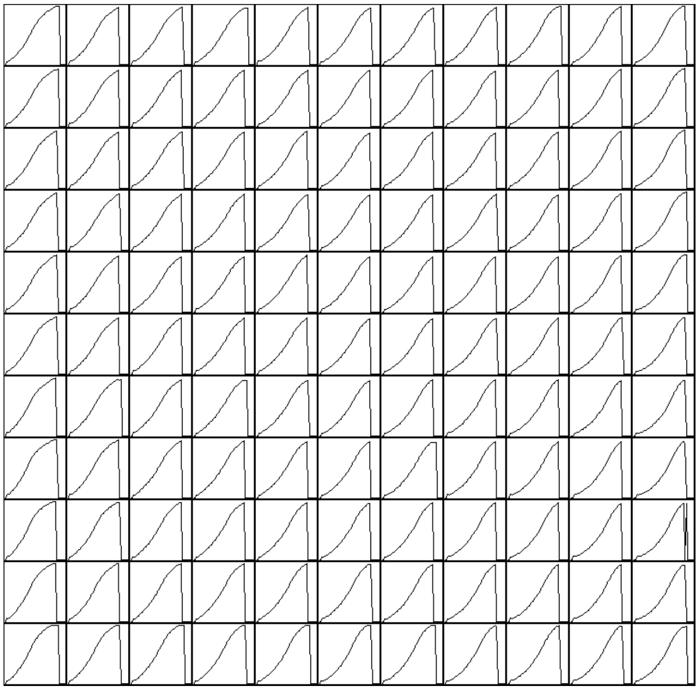

Figure 4.12: The drift time to C/A ration mapping of detector 4R100 on 121 anode pixels. The horizontal axis is the C/A ratio depth and the vertical axis is the drift time.

As long as the drift time is known, the interaction depth can be calculated from this mapping. For every single-pixel event, the interaction depth can be calculated by two different methods. One is the C/A ratio and the other is the drift time. Fig. 4.13 shows that for the same data set, using the drift time to C/A ratio mapping does not degrade the energy resolution significantly. In cases that the drift time measurements of multiple-interaction events are accurate, the drift time to C/A ratio conversion

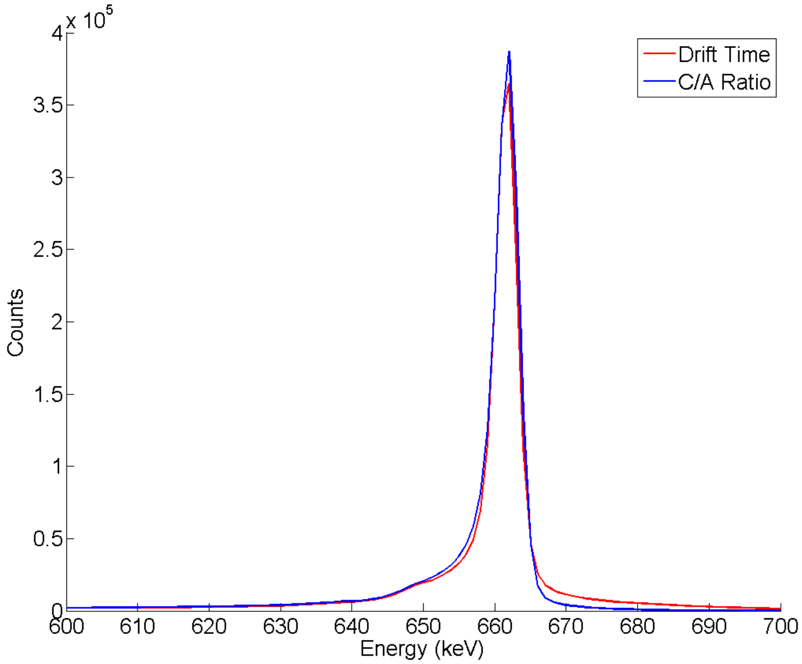

Figure 4.13: Comparison of C/A ratio reconstruction and drift time reconstruction of single-pixel events for 661.7 keV gamma-rays.

should not be the major factor of the energy resolution degradation of multiple pixel events in a single detector.

4.3.3 Weighting Potential Cross-talk Correction and Non-linearity Correction

As introduced in Chapter I, the induced signal can still occur even if the charges are not collected by the electrode. For multiple pixel events, the motion of one electron cloud will induce signals on all other pixels. The amplitude of the induced signal on other pixels depends on the energy deposition in each pixel, the separation between pixels and the interaction depth of each electron cloud. This type of signal induction is called weighting potential cross-talk (WPCT). In order to visualize WPCT, two pixel events are grouped by their x-y separations and the photopeak centroid of each separation spectrum is an indication of the WPCT effect. Fig. 4.14 illustrates the photopeak centroid change over different x-y separation and it shows that the

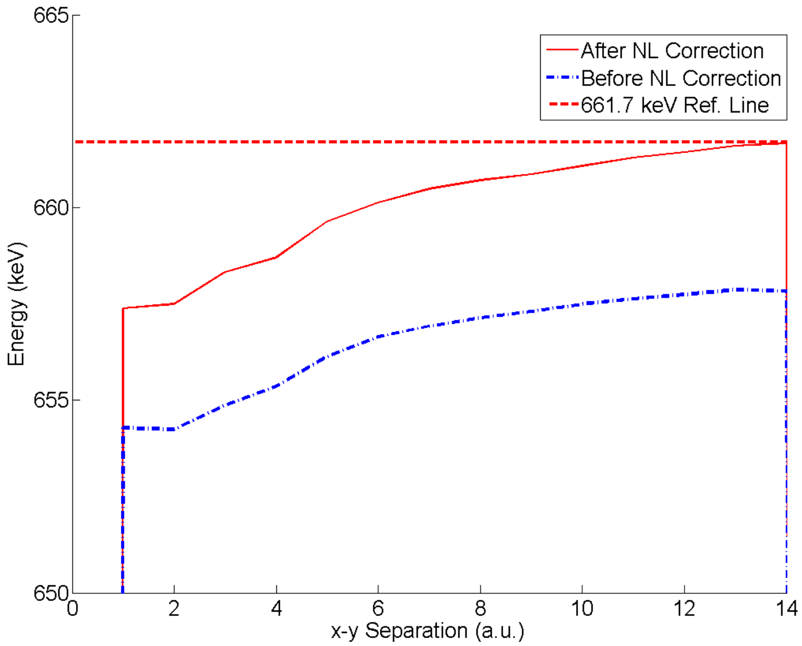

Figure 4.14: Weighting potential cross-talk correction curvee improvement after non-linearity correction. The depth is weighted by the energy deposition of each interaction.

energy of the measured photopeak centroid increases while the x-y separation gets bigger due to the reduced effect of WPCT. If two pixels are far away, the WPCT effect should be insignificant and the photopeak centroid of this type of events should be very close to the full energy 661.7 keV. However, the blue dashed curve shows that the photopeak centroid is at about 658 keV for the furthest separation before non-linearity correction. Clearly, after the non-linearity correction, the photopeak centroid of those events with bigger separation is much close to 661.7 keV. Therefore the non-linearity is not a negligible factor when calibrating WPCT. Dr. Feng Zhang invented an algorithm to correct this weighting potential cross-talk by binning the two-pixel full energy events into 2-D matrix, which depends on the pixel separation and the weighted interaction depth.

Table. 4.2 shows that the energy resolution of two pixel events get improved from 0.96% to 0.87% after the non-linearity correction. Without the non-linearity correction, the weighting potential cross-talk cannot be calibrated accurately since the signal deficit is caused by a combined effect. Usually, the weighting potential cross-talk will lead to underestimate of the energy deposition since the cross-talk signal has a negative amplitude tail. According to Fig. 4.6, the non-linearity also causes the recorded signal amplitude to be smaller than it should be. However, the non-linearity offset does not depend on either the pixel separation or the weighted interaction depth. Therefore, these two factors have to be corrected separately. Fig. 4.15 shows the weighting potential cross-talk calibration curve corresponding to separation 7 on Fig. 4.14. The summed photopeak centroid is increased by about 3 keV due to the underestimating of the energy deposition on each pixel. After the non-linearity correction, the weighting potential cross-talk calibration curve is not a combined effect any more. It can also be applied to multiple pixel events based on the pixel separation and weighted interaction depth as a first order approximation. Even after the non-linearity correction, according to Fig. 4.7 and Fig. 4.8, the recorded energies still have some residual energy offsets. The effect of these offsets has been studied using a Geant4 simulation. Since the relationship between the residual energy offset and true energy is known and the Geant4 simulation can provide the true energy deposition, photopeak broadening caused by the effect of the residual energy offsets can be isolated. Fig. 4.16 shows that the FWHM at 662 keV caused by the residual energy offsets after the non-linearity correction is about 0.8 keV, which is not a significant contribution to the energy degradation of single-detector multiple-pixel events.

According to the discussion about inter-module chance coincidence events of ^{133}Ba spectrum, the energy resolution should follow the quadrature sum principle after the non-linearity correction, and it has also been proven that neither the drift time to C/A ratio conversion nor the residual energy offset of the non-linearity correction degrades the energy resolution significantly. The conclusion can be drawn that the current weighting potential cross-talk correction model most likely is the major cause

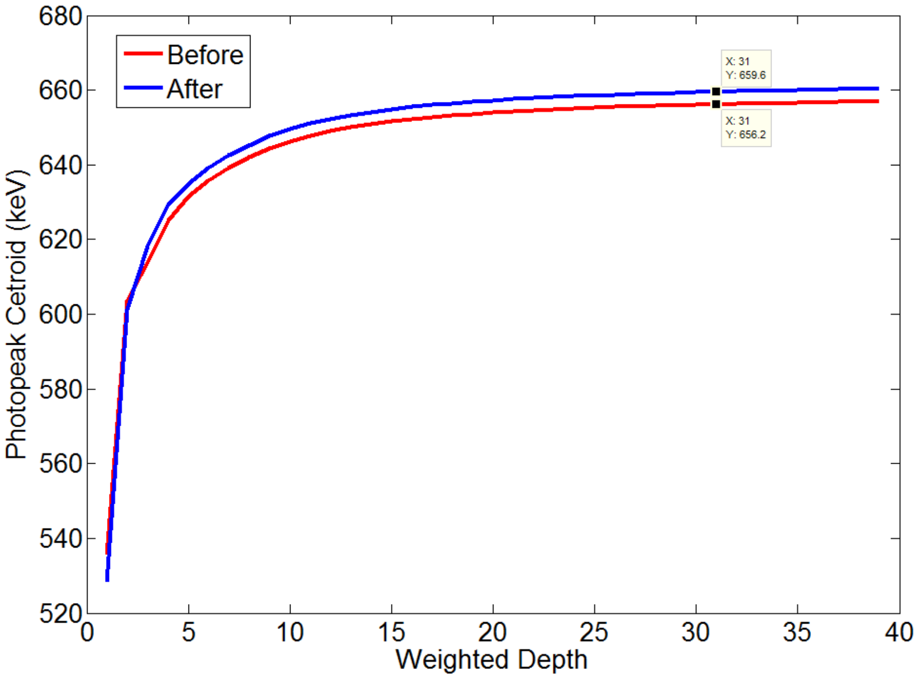

Figure 4.15: Weighting potential cross-talk correction curvee improvement after non-linearity correction.

of the energy resolution degradation of single-module multiple pixel events.

4.4 Conclusion

The non-linear response of the digital ASIC array system has been observed. The non-linearity effect on different types of events has been studied, including single-pixel events, multiple pixel events and inter-module events. In order to correct these effects, Dr. Feng Zhang's non-linearity calibration experiment design has been adopted and the improvement is significant, especially for high energy gamma-rays. Since there are multiple modules in the array system, the cross-talk noise between modules are undesirable for inter-module events. The chance coincidence events of ^{133}Ba has successfully proven that the cross-talk noise between modules is insignificant. The multiple pixel energy resolution degradation has also been investigated and the weighting potential cross-talk effect and non-linearity effect are separated. The current WPCT correction model is most likely the major cause for the multiple pixel

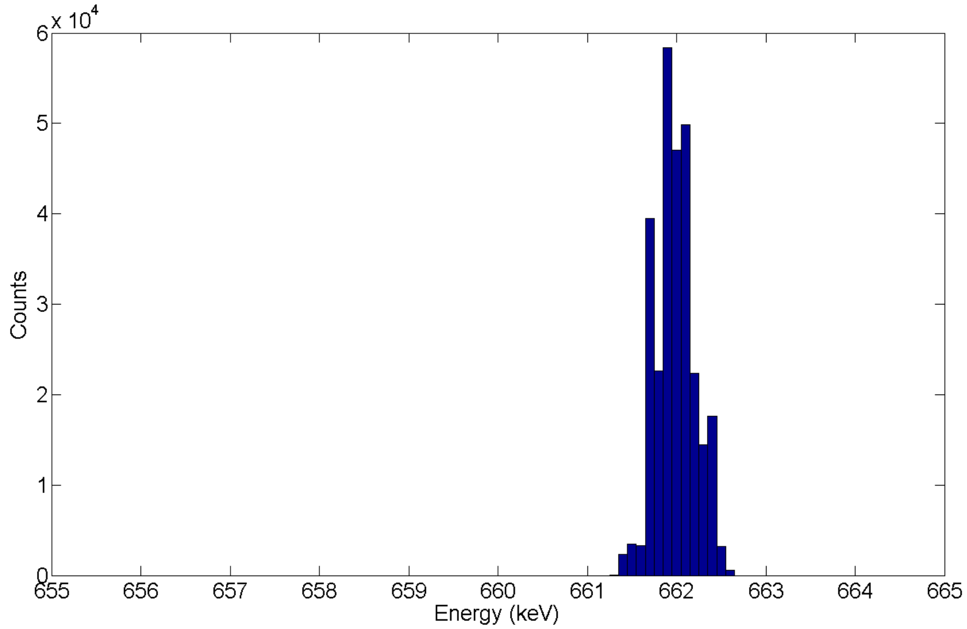

Figure 4.16: Simulated photopeak of two-interaction events with 662 keV energy deposition only considering the effect of the residual energy offsets after non-linearity correction.

event energy resolution to degrade faster than the quadrature sum prediction.

CHAPTER V

Event Classification and Improved Event Reconstruction

Gamma rays do not carry any charge so in order to be detected, they must first transfer their energy to a charged particle or create a charged particle. An example is the creation of electron-hole pairs in semiconductor materials. There are a large number of possible interaction mechanisms known for gamma rays in semiconductor materials, but only three types of them are of great interest in our radiation detection measurements: (1) photoelectric absorption, (2) Compton scattering, and (3) pair production. Each of these three processes will transfer partial or complete gamma-ray energy to charged particles, such as electrons and positrons and electron-hole pairs are generated during the ionization of these charged particles. Different interactions have different signatures on their waveforms and knowing the event type can improve the reconstruction of that event since the physics associated with it can be modeled and its effect can be included in the reconstruction process. This chapter will discuss three types of events due to the detector pixelation and the signal induction mechanism, (1) single-pixel multiple-interaction events, (2) incomplete charge collection events, and (3) side-neighbor charge leak events. Both the identification and reconstruction algorithms will be discussed and the performance improvement will also be demonstrated.

5.1 Single-Pixel Multiple Interaction Events

As introduced in Chapter I, the x and y interaction location is determined by which pixel triggers the system. Detectors used in the following experiments have 11 by 11 anode pixels with a pixel pitch size 1.72 mm×1.72 mm. Since each pixel has a finite size, multiple interaction can happen underneath the same pixel, which results in a single pixel multiple interaction event. These single pixel multiple interaction events have been analyzed using the preamplifier signals from each anode pixel. When multiple interactions occur underneath one pixel, an analog ASIC readout system cannot identify the unique interaction locations because only the total energy deposition and earliest trigger time are recorded. However, the digital ASIC can digitize the entire pre-amplifier signal waveforms, which have unique signatures for this type of events. An algorithm has been developed to identify this kind of events and a new reconstruction method has been employed to extract the interaction location and energy deposition information of each individual electron cloud of these events [55]. Since the digital ASIC can record the neighbor pixel waveforms along with the collecting pixel, the sub-pixel position information can also be extracted. In order to verify the confidence level of this event identification algorithm, the preamplifier signal from a pixelated CdZnTe detector has been modeled [56].

5.1.1 Experiment

Experiments were performed on a pixelated CdZnTe detector with a common steering grid between pixels. The detector volume is 20 mm×20 mm×15 mm and was manufactured by Redlen Technologies. Bias voltages of -3000 and -110 were applied to the cathode and grid electrodes respectively to drift and steer the generated electron clouds. In order to study single-pixel multiple interaction events at different energies, two radiation sources were used: ^{137}Cs and ^{60}Co. Each source was placed about 5 cm above the cathode surface, as shown in Fig. 5.1. The digital ASIC array and readout

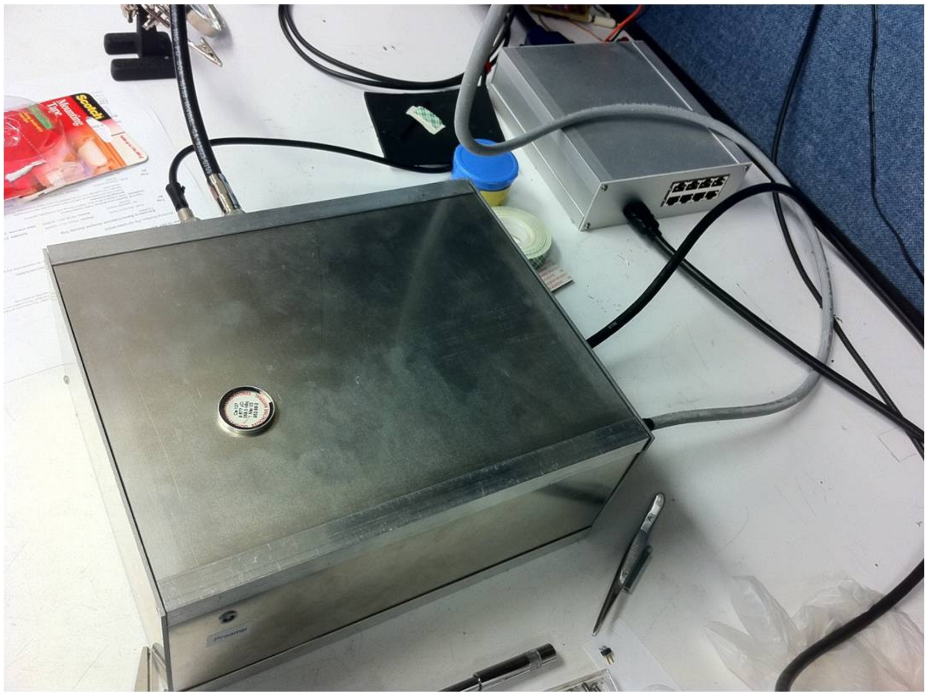

Figure 5.1: Experiment Setup

board were sitting inside the aluminum box.

5.1.2 Event Identification Algorithm

Fig. 5.2 shows an illustration of a single-pixel single-interaction event and single-pixel multiple-interaction event. The two corresponding waveforms are shown in Fig. 5.3. The sampling frequency was set at 40 MHz in the experiment so each cell index represents a 25 ns time interval. Clearly, the anode waveform has a double-step profile for single-pixel multiple interaction event due to the different collection times of each electron cloud. The time interval between two leading edges is determined by the interaction depth separation of these two electron clouds. The cathode waveform, although noisier, also has two different rising slopes. The second slope is less than the first one since it is only induced by one of the electron clouds. The analog ASIC can only provide the amplitude for the overall signal since there is only one slow shaper in each pixel channel. The C/A ratio will not be able to reconstruct the interaction

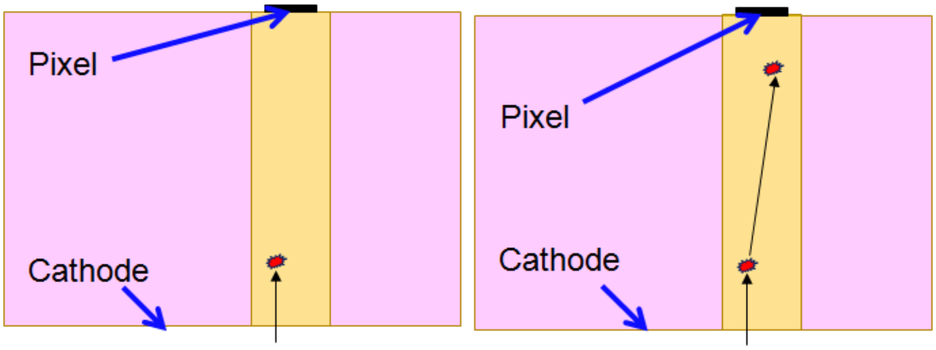

(a) (b)

Figure 5.2: Illustration of single-pixel single interaction (a) event and single-pixel multiple interaction (b)event.

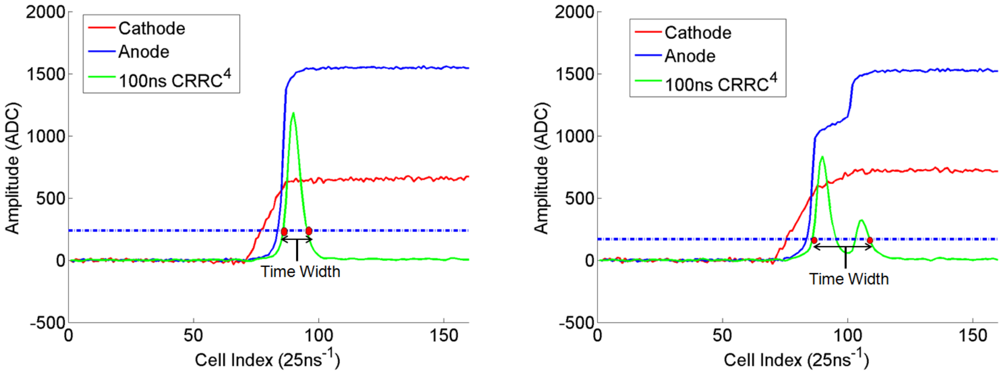

(a) (b)

Figure 5.3: Waveforms of single-pixel single interaction event (a) and single-pixel multiple interaction event (b).

depth since more than one interaction occurred.

In order to reconstruct these events correctly, an alternative reconstruction algorithm was sought. The double-stage profile can be identified by using a faster CR-RC^4 filter. The after-shaping waveforms are illustrated by the green curves on Fig. 5.3 and the peaking time constant was 100 ns. The response of a step voltage input after a CR-RC^n filter can be calculated via Eq. 5.1, where $E_{out}(t)$ is the after shaped signal over time t, E is the input step voltage input amplitude, τ is the time constant, n is the order of the integration circuitry. Eq. 5.1 assumes the differentiation and n

integration time constants are identical. The derivative of Eq. 5.1 equal to zero gives the time required for the shaped pulse to reach the maximum amplitude, which is equal to $n\tau$. For the simplified model, the induced signal of the single-pixel single interaction event anode waveform can be approximated by step voltage $E(t)$ in Eq. 5.3. If a constant fraction threshold is set for the shaped signal, the time width between the passing threshold can be mathematically calculated via Eq. 5.1 and 5.2, where a is the constant fraction. The time width is marked out in Fig. 5.3 with red dots. In Fig. 5.3 (a), n is set at 4 and τ is set at 25 ns, which is equivalent to 100 ns peaking time, and a is set at 25%. According to Eq. 5.1 and 5.2, t_0 and t_1 have values of 0.88τ and 10.98τ separately and the time width is about 10τ, which does not depend on the input signal amplitude. If there are multiple interactions underneath the same pixel, the corresponding anode waveform can be approximated by $E(t) + E(t + \Delta t)$, where Δt is the delay time due to the different interaction depths. Since the filtering is a linear process, the shaped signal should be the sum of two step voltage signals, $E_{out}(t) + E_{out}(t + \Delta t)$. Thus, the time width could be any number greater than 11.5τ as indicated by Fig. 5.3 (b). The upper boundary of the time width is determined by the maximum depth separation, which is 15 mm in the experiment. Therefore, the time width has been selected as the signature of these single-pixel multiple interaction events.

$$E_{out}(t) = E(\frac{t}{\tau})^n e^{-\frac{t}{\tau}} \tag{5.1}$$

$$E_{out}(t_0) = aE, E_{out}(t_1) = aE \tag{5.2}$$

$$E(t) = \begin{cases} 0, & t < 0 \\ E, & t \geq 0 \end{cases} \tag{5.3}$$

Fig. 5.4 shows the time width distribution of single-pixel events from ^{137}Cs and ^{60}Co. It is consistent with the predication that the time width should not depend on the signal amplitude, which leads to the similar distribution from different gamma-ray energies. Since the calculated time width is about 10τ and τ is 15 ns, the distribution reaches its maximum at about 10 samples. Theoretically, the distribution should be a delta function if the input signal was a step voltage. In fact, the anode pulse waveform does have a finite rise time, which causes the broadening of the peak. The most probable time width does heavily depend on the selection of the constant fraction threshold a. The threshold could not be set arbitrarily low since the electronic noise could pass the threshold and cause over estimation of the time width. It cannot be set arbitrarily high as well since the smaller of the two energy depositions may not be able to pass the threshold. In this experiment, the constant fraction threshold was set to 25% of the highest signal amplitude of shaped pulse. Fig. 5.4 also shows that the distribution has a high end tail for both gamma-ray energies, which is primarily caused by the single-pixel multiple interaction events. The threshold for the high end tail is the figure of merit to determine the event type and can be obtained through a calibration process. This fixed threshold strongly depends on the separation of each interaction. Since each electron cloud has a finite size, if two electron clouds are close to each other, they virtually become one electron cloud. In this experiment, the threshold was set at 13 sample time intervals (325 ns), which is equivalent to about 1.25 mm separation between the two interactions. After the threshold of a detector is calibrated, the event identification algorithm can be performed event by event and real time event classification is demonstrated feasible.

Fig. 5.5 shows two interesting single-pixel multiple interaction events picked by the event classification algorithm. Fig. 5.5 (a) is a typical waveform for the events with two electron clouds close to each other. The waveform on Fig. 5.5 (b) is very similar to that of a large separation Compton scattering event [10]. However, since the ^{137}Cs

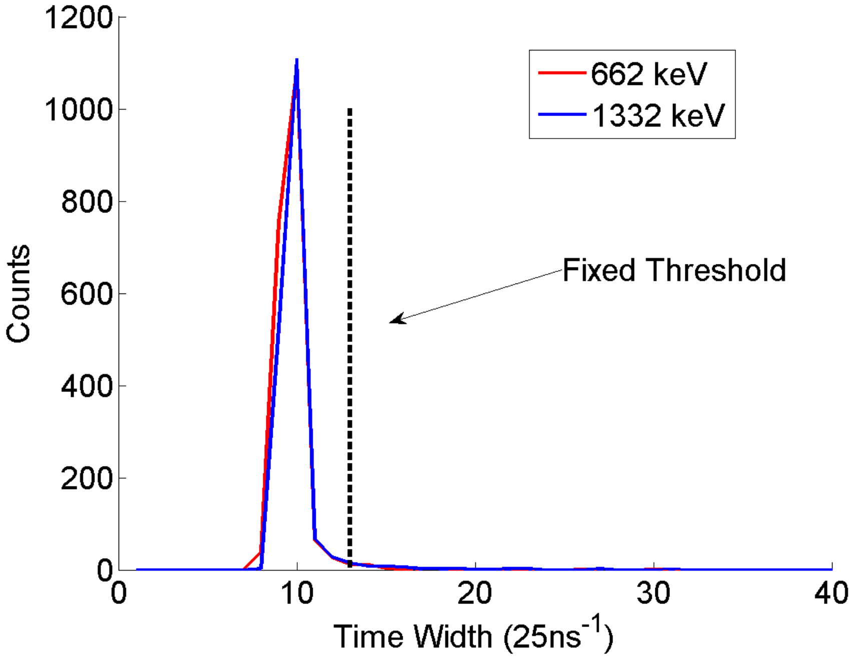

Figure 5.4: Time width distribution of single-pixel events from ^{137}Cs and ^{60}Co

source was placed above the cathode surface, the electron cloud closer to the anode has an energy distribution shown in Fig. 5.6. The minimum energy deposition for the interaction closer to the anode side is about 288 keV for a Compton scattering based on the Compton scattering equation. The waveform on Fig. 5.5 (b) shows that the first collected electron cloud has an energy deposition below 200 keV, which is physically impossible for a single Compton scattering event. According to the simulation results, the waveform is from a bremsstrahlung event. The smaller electron cloud is generated by the bremsstrahlung X-ray while the bigger one is generated through photoelectric absorption interaction of the incident gamma ray. Fig. 5.6 also shows that the energy deposition of the first collected electron cloud does not change significantly when the scattering angle θ is large. In other words, the back scattering gamma rays carry similar energy, which leads to a greater $d\theta/dE$. For instance, an energy deposition at 475 keV, $\pm$ 2 keV will cause $\pm10°$ angular uncertainty. Even though the Compton scattering open angle for single-pixel two-interaction Compton scattering events is

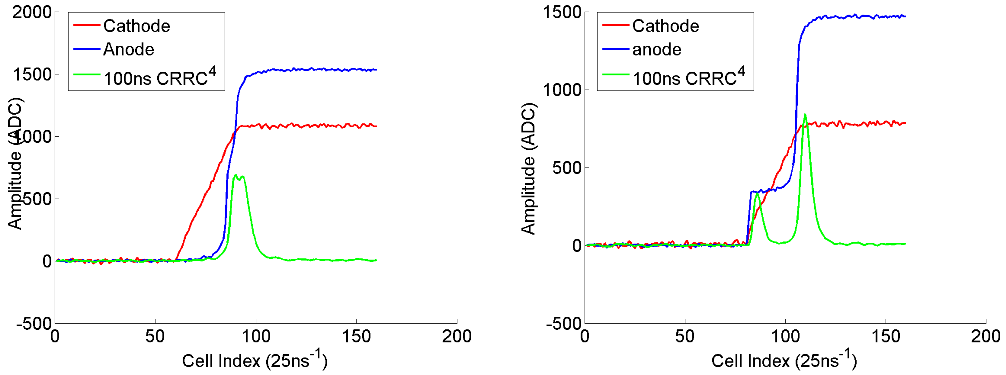

(a) (b)

Figure 5.5: Two interesting events picked by the event identification algorithm. (a) is a multiple interaction event with two electron clouds close to each other. (b) is a bremsstrahlung event.

very small, the angular resolution of these events could still be very poor.

5.1.3 Event Reconstruction Algorithm

In order to reconstruct the energy deposition and interaction depth of each interaction, the system response function developed by Dr. Yuefeng Zhu has been used [5] as an alternative gamma-ray event reconstruction method. Similar to the concept of system response in signal processing, the system response function of a radiation detector system describes the output when a unit energy deposition occurs within the detector. Since analytical expression cannot fully represent the real experimental system model, the system response function was generated experimentally. Each detector has 121 anode channels and the entire bulk is divided into 40 depth bins so overall there are about 5000 voxels' responses that need to be generated. An example of system response function for one anode pixel is shown on Fig. 5.7 [5]. After the system response matrix for every voxel is generated, the gamma-ray energy and interaction position can be calculated via least-square fitting between recorded waveforms and the system response functions.

Fig. 5.8 illustrates the system response function reconstruction for a single-pixel

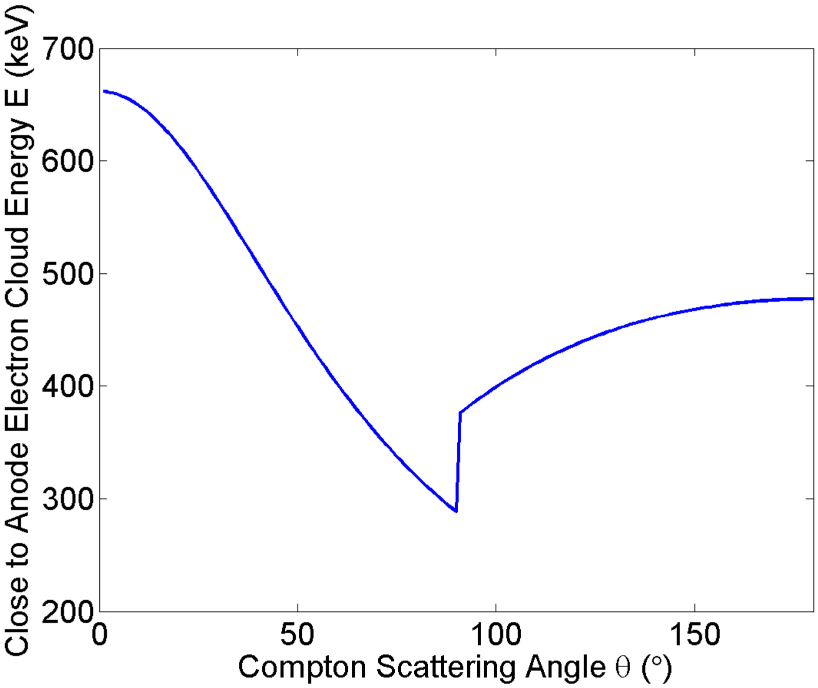

Figure 5.6: Energy deposition of the first collected electron cloud over different Compton scattering angle.

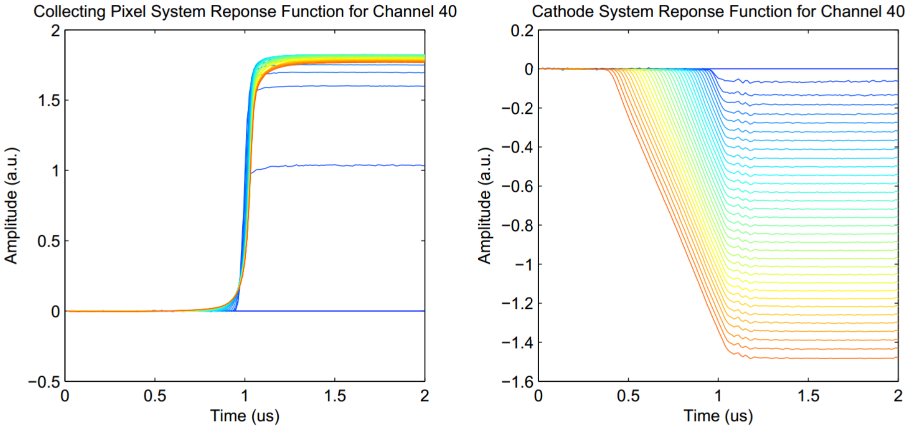

Figure 5.7: An illustration of the system response function for one anode pixel. The color code from blue to yellow to red represents the different depths in the detector. [5]

single interaction event and a single-pixel multiple-interaction event. For single interaction events, there are only three degrees of freedom in the fitting parameters, interaction depth d, energy deposition E and trigger time amplitude walk t. After iterations, a set of (d, E, t) can be solved for every gamma-ray event waveforms. Waveforms corresponding to the set of (d, E, t) are shown in pink and green in Fig. 5.8. Intuitively, if there are multiple interactions underneath the same pixel, there should be six degrees of freedom in the fitting parameters, (d_1, E_1, t_1, d_2, E_2, t_2). One missing consideration is the correlation between multiple interactions. With the current counting rate, the chance coincidence event rate is relatively low. Thus, most of these multiple interaction events should be correlated, which means that the multiple interaction event should be generated by the same incident gamma-ray and the cathode response of each individual interaction should share the same starting time since the flight time of gamma-ray in 15 mm thick detector is negligible. The cathode timing constraint should be added to the reconstruction algorithm reducing the degrees of freedom to five. The anode and cathode waveforms for each interaction can be reconstructed separately and the effect of the cathode constrain is shown on Fig. 5.8 (c). Clearly, the two cathode waveforms in green have the same starting time. Fig. 5.8 (d) illustrates the ballistic deficit of the reconstructed signal in blue if the single-pixel multiple interaction events are recorded using an analog ASIC. Both anode waveforms represent experimental data and the shaping time of the simulated CR-RC^4 shaper is 1.2 μs. With the system response function, the full signal amplitude can be reconstructed correctly so that the ballistic deficit is avoided. Fig. 5.9 shows the spectra comparison for only single-pixel multiple interaction events between the slow shaper reconstruction and system response function reconstruction. Even though the energy resolution did not improve, the photopeak centroid is closer to 661.7 keV using the system response function reconstruction since slow shaper causes signal ballistic deficit.

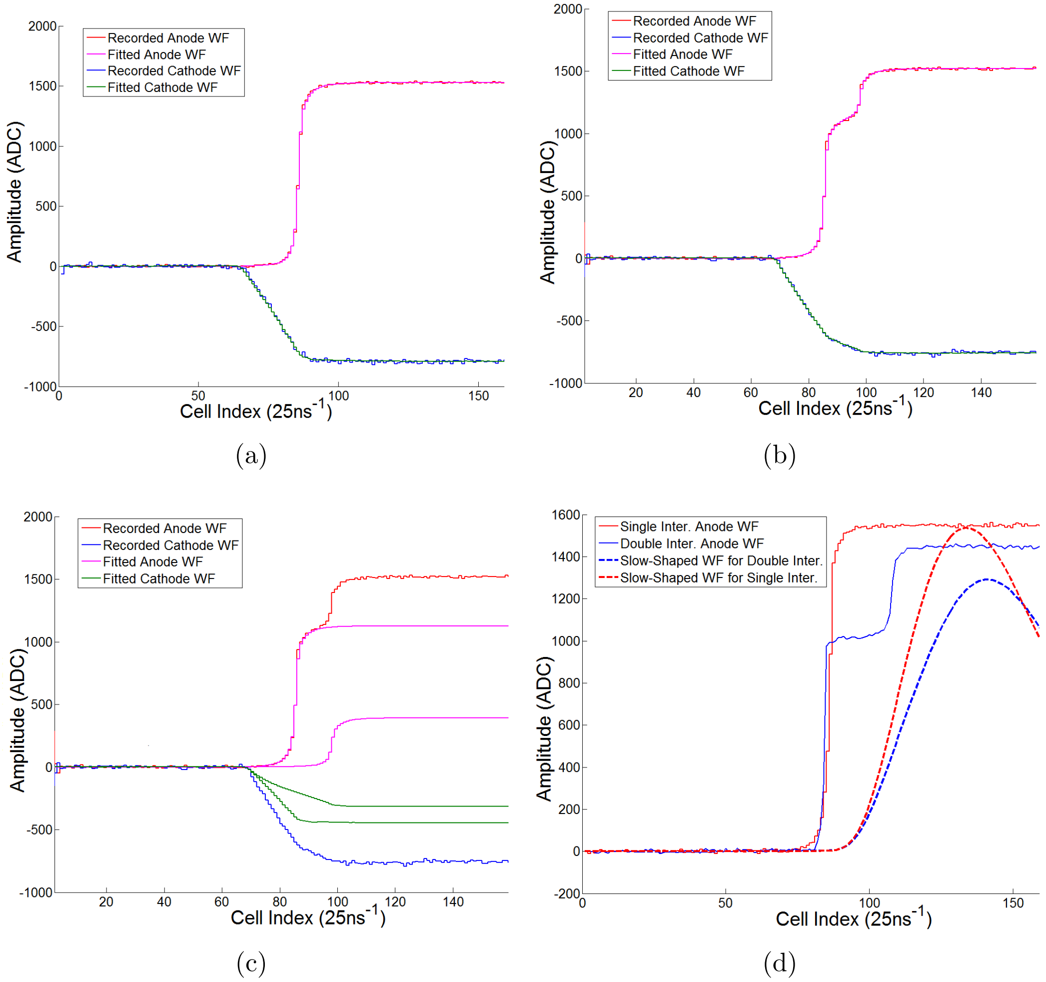

Figure 5.8: Illustration of system response function reconstruction algorithm. (a) is for a single-pixel single interaction event and (b) is a single-pixel multiple interaction event. (c) shows the fitted anode and cathode waveforms for each interaction. (d) shows the ballistic deficit due to the double-step profile.

Since the energy deposition of each interaction can be reconstructed separately according to Fig. 5.8 (c), the distribution of each energy deposition is shown in Fig. 5.10. All the events are chosen with a depth separation above 375 μm, which is the width of one depth bin (15mm/40bins). If the separation is smaller than one depth bin width, it is difficult to classify it as multiple electron clouds. For every event, there are two electron clouds, one closer to the anode side and the other further away. Interestingly, there are two peaks in the energy deposition distribution indicating a preference of interaction. The centroid of both peaks are measured at 186 keV and 476 keV re-

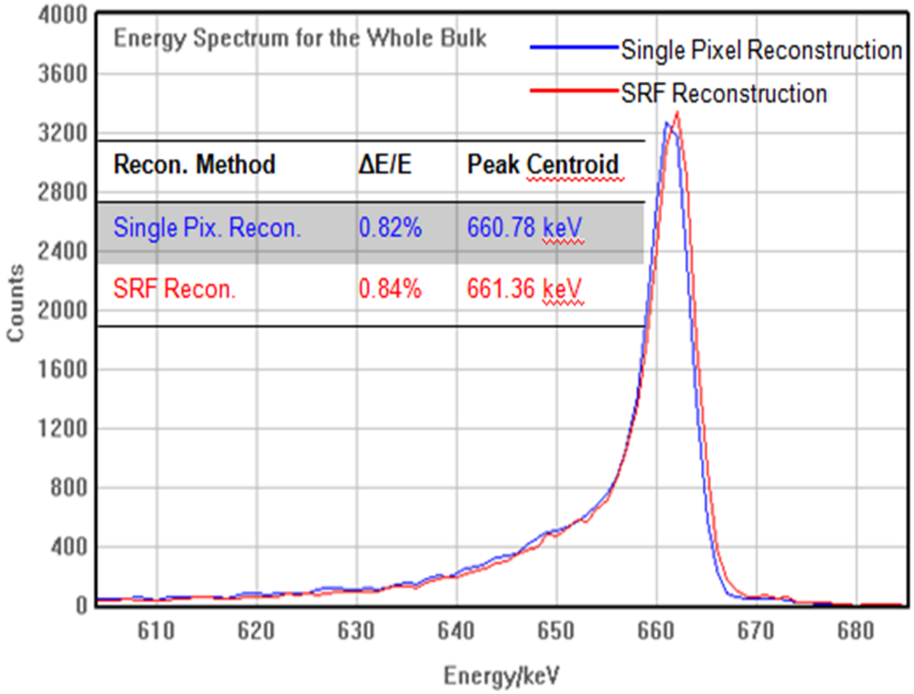

Recon. Method	ΔE/E	Peak Centroid
Single Pix. Recon.	0.82%	660.78 keV
SRF Recon.	0.84%	661.36 keV

Figure 5.9: The spectra comparison between slow shaper reconstruction and system response function(SRF) reconstruction.

spectively. Using Compton scattering equation or Fig. 5.6, the scattering angle can be calculated and is close to 180°, which means most of the single-pixel multiple interaction events are back scattering events since the ^{137}Cs source was placed on the cathode side. For single-pixel multiple interaction events, the Compton scattering angle should be either very small or fairly large, otherwise the scattered gamma-ray can easily escape to the neighbor pixels. The preference scattering angle tends to be back scattering rather than forward scattering because the mean free path of 190 keV gamma rays is about 5 mm while that of 500 keV is about 2 cm. Fig. 5.6 shows that if the scattering angle is smaller than 40°, the energy of the scattered gamma-rays is greater than 500 keV, which has a lower probability of being captured in the same pixel than that of 190 keV gamma rays.

With the digital ASIC system, not only can the collecting pixels' waveforms be recorded, but the neighbor pixels up to eight for each collecting pixel can also be

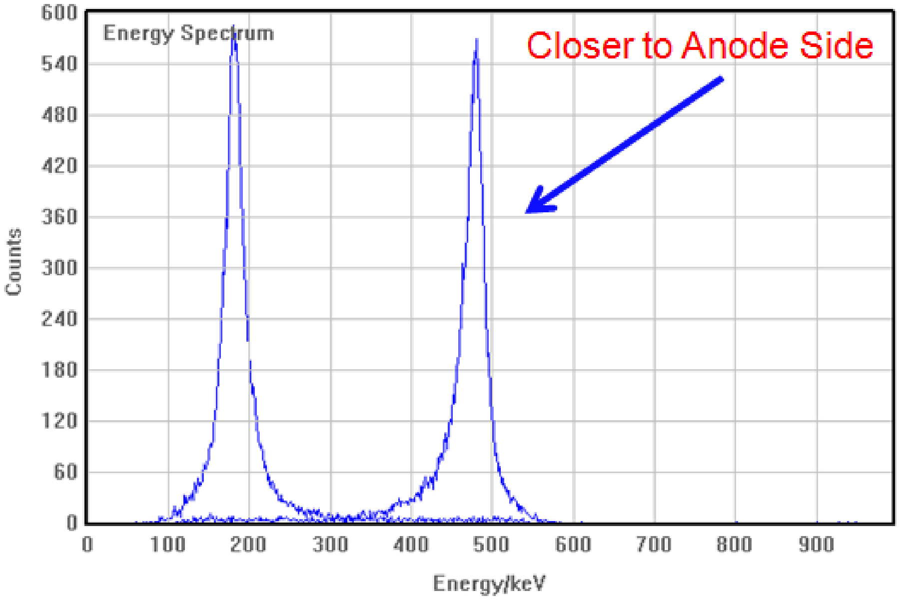

Figure 5.10: Individual energy deposition distribution of single-pixel multiple interaction events.

recorded. The signal on the neighbor pixels, called a transient signal, is very useful to improve the lateral position resolution of each gamma-ray event. Compared to the pixel pitch size of 1.72 mm, the size of the electron cloud generated by several hundred keV gamma-rays is fairly small, which means the collecting position of the electron cloud can vary from event to event even under the same pixel. An algorithm has been develop to calculate the sub-pixel position of each electron cloud by making use of the transient signals. This will be explained in the next chapter. Since the neighbor pixel waveforms of these single-pixel multiple interactions events are recorded as well, the sub-pixel position of each interaction can also be calculated via the system response function. Similar to the generation of the system response matrix for the collecting pixel, the system response matrix for the neighbor pixels was also obtained experimentally. Fig. 5.11 illustrates the sub-pixel position reconstruction for single-pixel multiple interaction events. Clearly, the transient signal peak for each interaction can be resolved by system response function. Since the transient signal amplitude is very small, the electronic noise plays an important role in the sub-pixel position

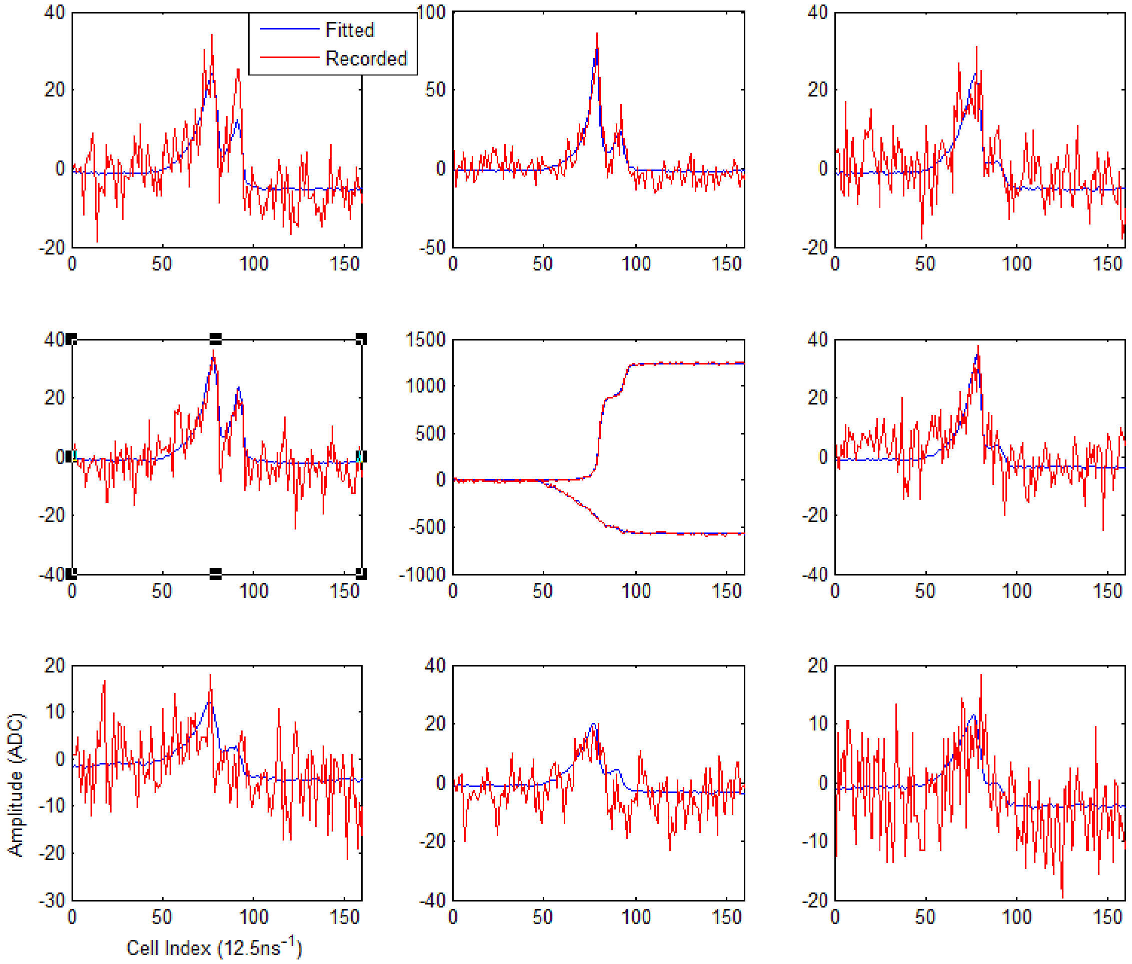

Figure 5.11: Illustration of sub-pixel position reconstruction for single-pixel multiple interaction event using system response function.

resolution. From the recorded neighbor pixel waveforms, there is a high frequency noise superimposed on the transient signal. This should be able to be improved by designing a better anti-aliasing filter in the next ASIC design iteration.

5.1.4 Simulation Validation

A simulation package has been developed to model the preamplifier signal from each electrode of a pixelated CdZnTe detector [56]. There are two major components in this package, GEANT4 simulation and waveform generator. GEANT4 has been used to generate list-mode data containing gamma-ray interaction positions and

Table 5.1: Confidence Level of the Event Identification Algorithm

Reconstruction Method	Separation	Simulation	Experiment	Confidence Level
Digital Filter	>3.75 mm	0.69%	0.61%±0.06%	88.4%
System Response Function	>1.25 mm	4.8%	4.5%±0.2%	93.8%

energy depositions and the waveform generator considers gamma-ray interaction positions and energy depositions within the CdZnTe detector, electron drift trajectories, charge induction due to weighting potential, and ASIC electronic noise to generate the waveforms. The simulated anode waveforms have been tested by the same event identification algorithm that was applied to the experimental waveforms. Since the interaction history of each simulated event is provided by GEANT4, the confidence level of the event identification algorithm can be measured with the simulated events.

Based on the simulation result, this algorithm can identify more than 85% of the single-pixel multiple interaction events correctly for 662 keV gamma rays, shown in Table 5.1. The ratio can be affected by the source position and the readout system noise. Since in this experiment the source was placed above the cathode surface, a fraction of those single-pixel multiple interaction events could be forward Compton scattering. For those forward Compton scattering events, one of the energy depositions is relatively small, which could be below the preset constant fraction threshold, which was set at 25%. Once the single-pixel multiple-interaction events are identified, they can be reconstructed more accurately in terms of energy depositions and interaction positions, including interaction depths and sub-pixel positions. There are two different methods to reconstruct the individual interaction depths and energy depositions: the digital filter and the system response function. However, the digital filter method can only be applied to the events with an interaction separation above 3.75 mm, although the identification algorithm can identify the events with a smaller interaction separation. Fig. 5.12 shows the event ratio of different interaction separation. There are two sets of curves on Fig. 5.12. On the left is the linear scale

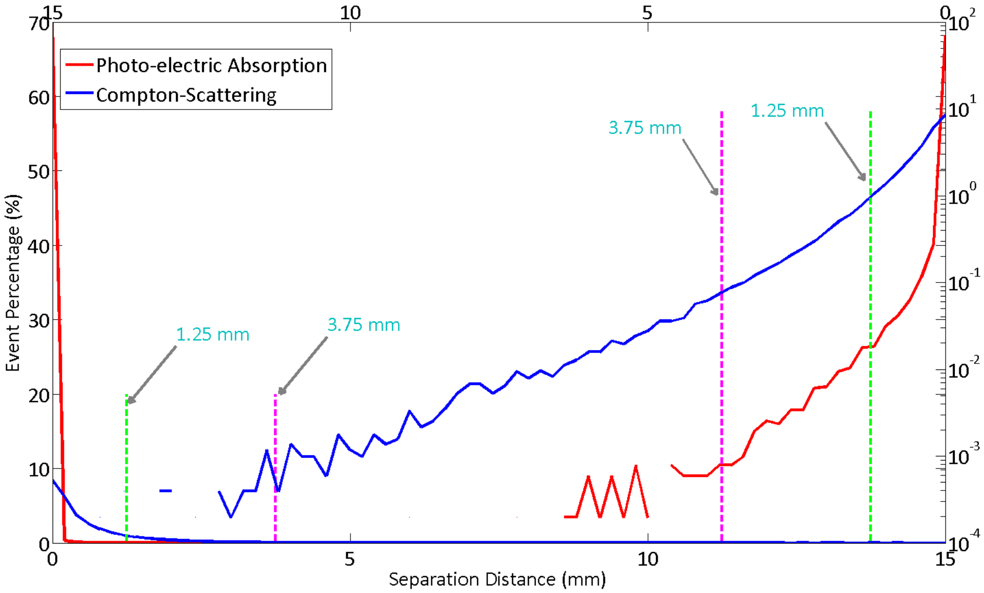

Figure 5.12: Events distribution vs. interaction separation for simulation.

y-axis and on the right is the log scale y-axis for the same data. The blue curve indicates that digital filter reconstruction algorithm can be applied to a very small fraction, 0.69%, of the total single pixel multiple interaction events while the classification algorithm using system response function can identify 4.8% of them shown in Table 5.1. In order to reconstruct the events with a small interaction separation, the system response function method has been used and the confidence level is more than 90% as shown in Table 5.1. Moreover, the digital filter construction method cannot reconstruct the individual sub-pixel position for each interaction while the system response function is capable of that as discussed in previous sections. The identification and reconstruction algorithms can extend the Compton scattering imaging capability to some single-pixel events with depth separation larger than 1.25 mm.

5.2 Single-Pixel Incomplete Charge Collection Events

In an ideal semiconductor detector, the electron-hole pairs generated by the incident gamma rays should be fully collected. Since the hole mobility is orders of magnitude smaller than electron mobility in CdZnTe detectors, only electrons are collected during the charge collection time. However, the electron cloud diffuses during the drifting and can spread over multiple pixels. In order to improve the charge collection in pixelated CdZnTe detectors for multiple pixel events, a common steering grid has been added between pixels. Usually, the steering grid is biased at a negative voltage to steer the electron cloud towards the anode pixels during operation. When an electron cloud is generated between two pixels, the electron cloud will be split and collected by two neighboring pixels. However, the steering grid around the edge pixels, also known as the guard ring, may not steer the entire electron cloud to be collected by edge pixels. Unlike the inner pixels, there are no anode pixels outside this guard ring which could collect the fraction of the electron cloud not collected by the pixel anode. As a consequence, the electron cloud of some events cannot be completely collected by anode pixels. These events are called incomplete charge collection events and they tend to take place on the edge pixels. If those events are full energy deposition events, the photopeak efficiency of the detector will have a deficit due to the loss of electrons collected on the guard ring or trapped on the surfaces of the CdZnTe detector. Since large volume high quality CdZnTe crystal is still difficult to grow, every full energy deposition event in CdZnTe detector is important to be reconstructed correctly in order to maximize photopeak efficiency.

Since the current single-pixel event energy reconstruction algorithm is based on the anode signal amplitude and the cathode-to-anode signal amplitude ratio(C/A), these events will be reconstructed to the wrong depth and energy bins. An algorithm has been developed to reconstruct these special events based on the system response function [57]. With this algorithm, both the interaction depth and energy deposition can be reconstructed correctly in the absence of a reliable anode amplitude. This reconstruction algorithm improves the single-pixel photopeak counts by close to 10%. The electron cloud size for 662 keV was also estimated with a square shaped model

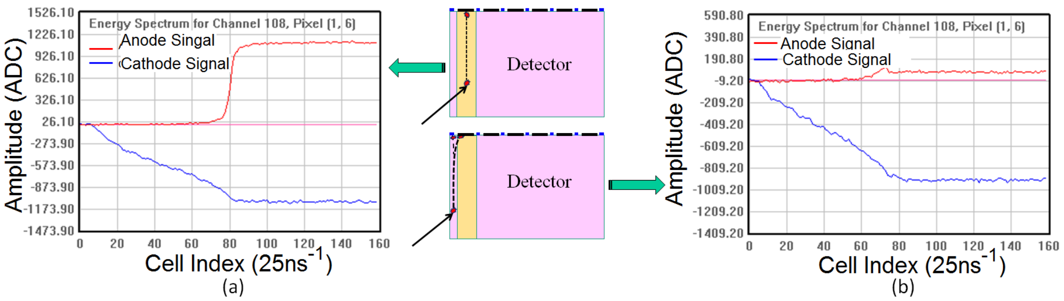

Figure 5.13: Recorded pre-amplifier output pulse waveforms for (a) a complete charge collection event and (b) an incomplete charge collection event using the digital readout system

based on the improvement of photopeak efficiency, and showed consistent results with Geant4 simulations.

5.2.1 Experiment Setup and Observation

Experiments were performed on a pixelated $20\times20\times15$ mm^3 CdZnTe detector with a common grid between pixels manufactured by Redlen Technologies. The steering grid was biased at -100 V. A ^{137}Cs source was placed on the cathode side. Fig. 5.13 illustrates two sets of signals obtained from the experiment for complete charge collection event and incomplete charge collection event respectively. Clearly, the anode waveform for the incomplete charge collection event does not carry useful energy deposition information. In order to develop the algorithm to reconstruction those events, they have to be identified out first.

5.2.2 Event Identification

From the Shockly-Ramo theorem, in a pixelated CZT detector, the induced cathode signal amplitude depends on both the interaction depth and energy deposition while the anode signal amplitude is primarily determined by the energy deposition. Therefore the C/A should not be greater than unity if the whole electron cloud is collected by the anode pixel after the electronic gain of the pre-amplifiers is normalized. However, if the electron cloud is only partially collected by the anode pixel, the C/A value could be greater than 1 since the cathode signal amplitude is not affected by the collection of electrons on the anode electrode. Thus, the C/A can be used as the signature of these incomplete charge collection events. This technique is shown mathematically below.

As an example, assume that the energy deposition is E_0, the interaction depth is d and a fraction of the electron cloud, denoted by a, is collected by one anode pixel. The value of a is 1 if the whole electron cloud is collected. The anode signal amplitude for this event can be approximated by

$$A = E_0 \cdot a \tag{5.4}$$

Similarly, the cathode signal amplitude can be approximated by

$$C = \frac{E_0 \cdot d}{D} = E_0 \cdot b \tag{5.5}$$

where b is the fraction of the detector thickness that the electron cloud drifts through. The C/A ratio can then be calculated using Eq. (5.4) and Eq. (5.5).

$$\frac{C}{A} = \frac{E_0 \cdot b}{E_0 \cdot a} = \frac{b}{a} \tag{5.6}$$

For complete charge collection events, Eq. (5.6) gives the value of C/A $= b$. Since the electron cloud cannot drift longer than the entire thickness of the detector, b has to be smaller than 1, thus C/A ≤ 1. In the case of C/A > 1, a has to be smaller than 1 corresponding to incomplete charge collection.

In this experiment, the threshold for C/A was set slightly higher than 1.0 at 1.1 to account for the fluctuation of C/A value due to the variation on electronic gain of different channels, and to correctly identify the incomplete charge collection

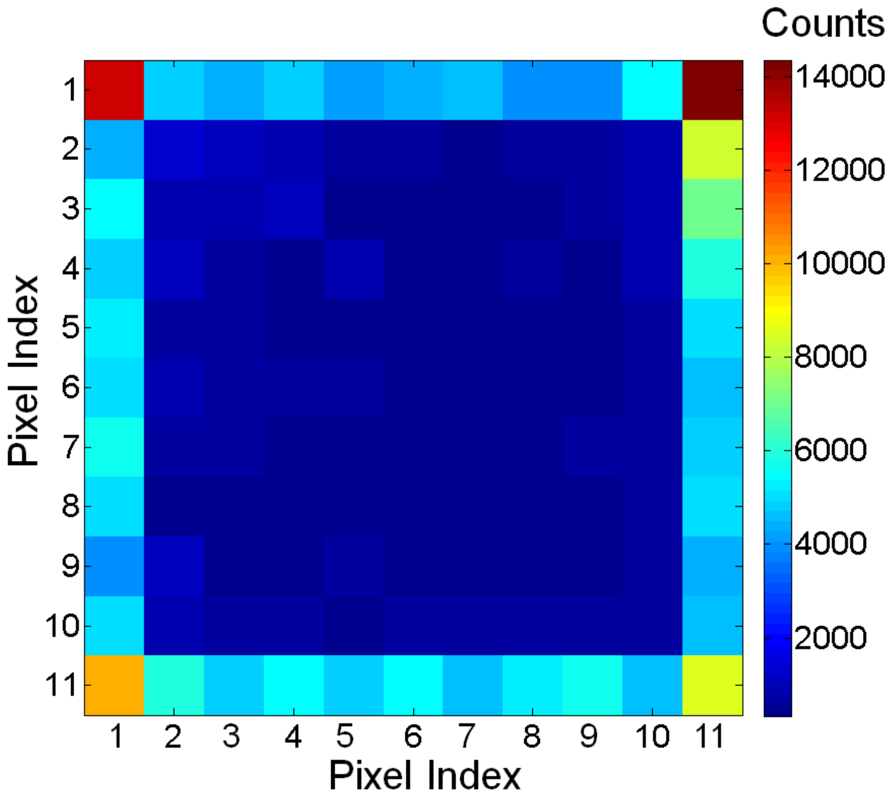

Figure 5.14: Distribution of incomplete charge collection events among 11×11 pixel anodes

event. The distribution for these incomplete charge collection events among 11×11 pixel anodes is shown in Fig. 5.14. Clearly, most of these events take place on edge pixels as expected because of the insufficient steering effect on the outer guard ring electrode. The incomplete charge collection can happen on the inner 9×9 pixels if a fraction of the electron cloud is collected by the grid or the neighbor pixels below the trigger threshold. However, these cases happen much less frequently as shown in Fig. 5.14. Most of the time, the steering grid splits the entire electron cloud and steers them to be completely collected by multiple pixels.

5.2.3 Event Reconstruction

For incomplete charge collection, the anode signal cannot be used to reconstruct the true energy deposition. However, the cathode signal is not affected by the col-

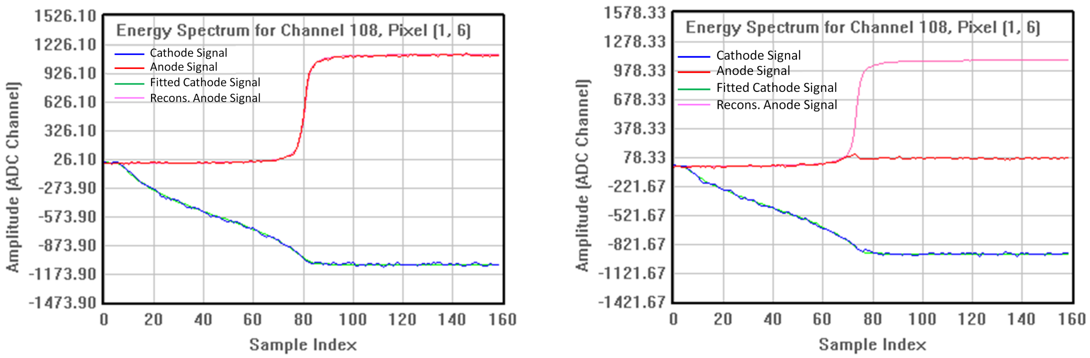

(a) (b)

Figure 5.15: Reconstructed signals for (a) complete charge collection event and (b) incomplete charge collection event in Fig. 5.13 respectively using system response function

lection of electrons by anode pixels, both the interaction depth and initial energy deposition can be reconstructed from the cathode signal alone. A reconstruction algorithm has been developed based on a set of cathode signals calculated for events at various depth. Then, through the least-squares fitting method, the best match to the measured waveform will be used to determine the depth of interaction and the energy deposition. The assumption for this reconstruction algorithm is that the system response is constant for all events collected by the same anode pixel. The Levenberg-Marquardt algorithm has been adopted for fast convergence. The reconstructed signals for events in Fig. 5.13 are shown in Fig. 5.15, respectively. Clearly, for the complete charge collection event, the reconstructed anode signal has the similar signal amplitude while for the incomplete charge collection event, there is a huge deficit on the measured signal due to charge loss. With this algorithm, the amplitude of incomplete charge collection event can be reconstructed to its correct value.

Fig. 5.16(a) proves that the reconstructed cathode signal amplitude is very similar to the measured signal amplitude, which verifies that the cathode signal is independent on charge collection on the anode electrode. In contrast, Fig. 5.16(b) shows that the reconstructed anode signal amplitude is greater than the recorded signal

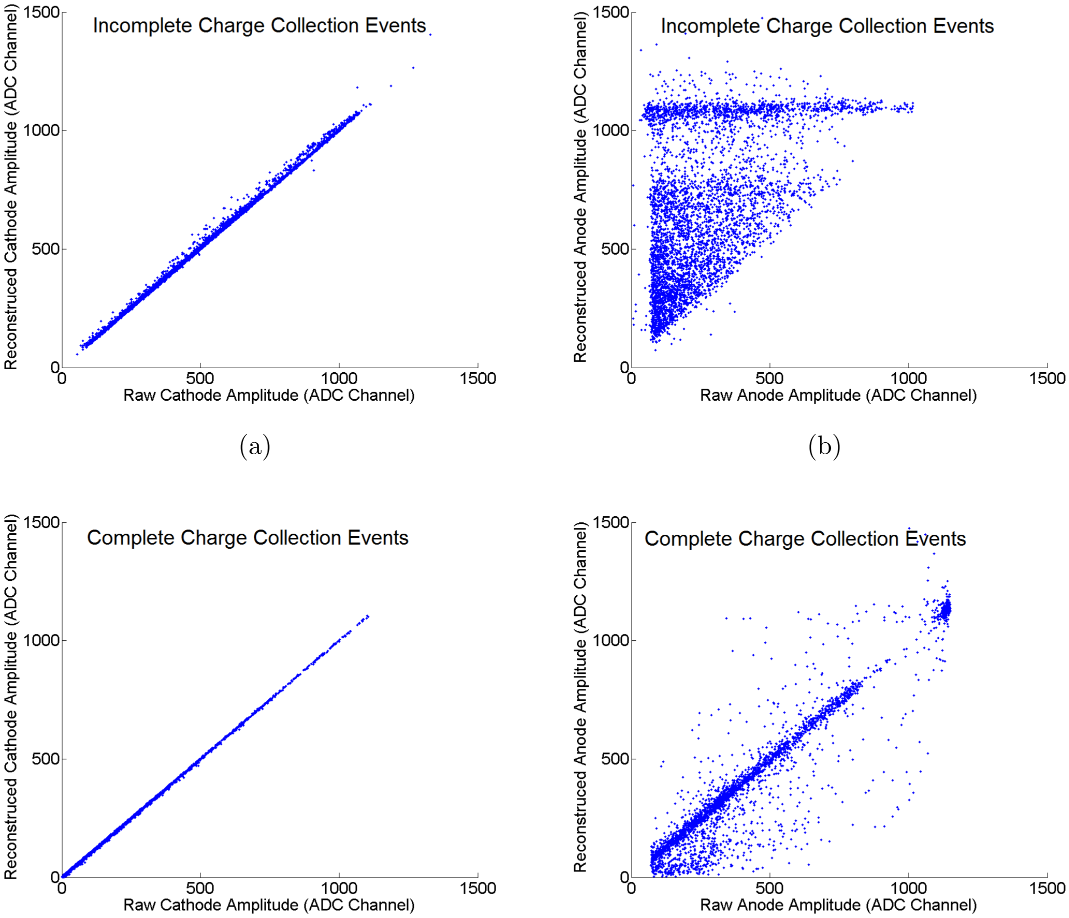

(a) (b)

(c) (d)

Figure 5.16: The correlation between raw cathode and anode signal amplitude and reconstructed signal amplitude for complete charge collection events and incomplete charge collection events

amplitude, which has signal deficit due to incomplete electron collection. The maximum reconstructed depth of interaction for the incomplete charge collection events is on the cathode surface, which indicates that the electron cloud can drift through the entire thickness of the detector without severe charge trapping. This also proves that Redlen CdZnTe detectors have very good charge transportation property even very close to the side surfaces of the crystals. The validity of this reconstruction algorithm has been proven by applying it to complete charge collection events. Since the anode waveforms for complete charge collection events have the correction signal amplitude, the reconstructed amplitude should be very close to raw amplitude, which is illustrated in Fig. 5.16(d).

5.2.4 Photopeak Efficiency Improvement

With the help of this technique, some of the incomplete charge collection events, especially the full energy deposition events, can be reconstructed to the correct energy, which improves the photopeak efficiency. Fig. 5.17 demonstrates that the full energy deposition events can be recovered using this reconstruction algorithm. On the recorded signal spectrum (Fig. 5.17(a)), there are almost no counts in the energy range of 600-700 keV while there is a clear photopeak at 662 keV on the reconstructed spectrum (Fig. 5.17(b)). The reconstructed spectrum for incomplete charge collection events has a poor energy resolution compared to that for complete charge collection events (Fig. 5.17(c)) due to worse signal-to-noise ratio of the cathode signal, which is used for reconstruction alone. The energy resolution for the reconstructed incomplete charge collection events is 4.7% FWHM at 662 keV compared to 0.7% FWHM for complete charge collection events. Fig. 5.18 shows that a clear photopeak stands out in every spectrum of all edge pixels after the reconstruction. The increase in photopeak efficiency can be calculated by the added photopeak counts of the spectrum in Fig. 5.17(b) in addition to that in Fig. 5.17(c). Table 5.2 shows that the photopeak efficiency is improved by about 20% for all edge pixels. The improvement of overall single-pixel photopeak efficiency improvement is close to 10%, which is lower than edge pixels, since only 40 edge pixels contribute most to the improvement. As shown in Table 3.3, the photopeak efficiency for ^{137}Cs is about 4% to 5% lower than simulation while the overall efficiency is very consistent with it. Considering single-pixel event fraction for 662 keV gamma rays is about 35%, the incomplete charge collection event reconstruction can improve the overall photopeak efficiency by $35\%\times 9.6\% = 3.4\%$. This makes the overall photopeak efficiency closer to the simulation predica-

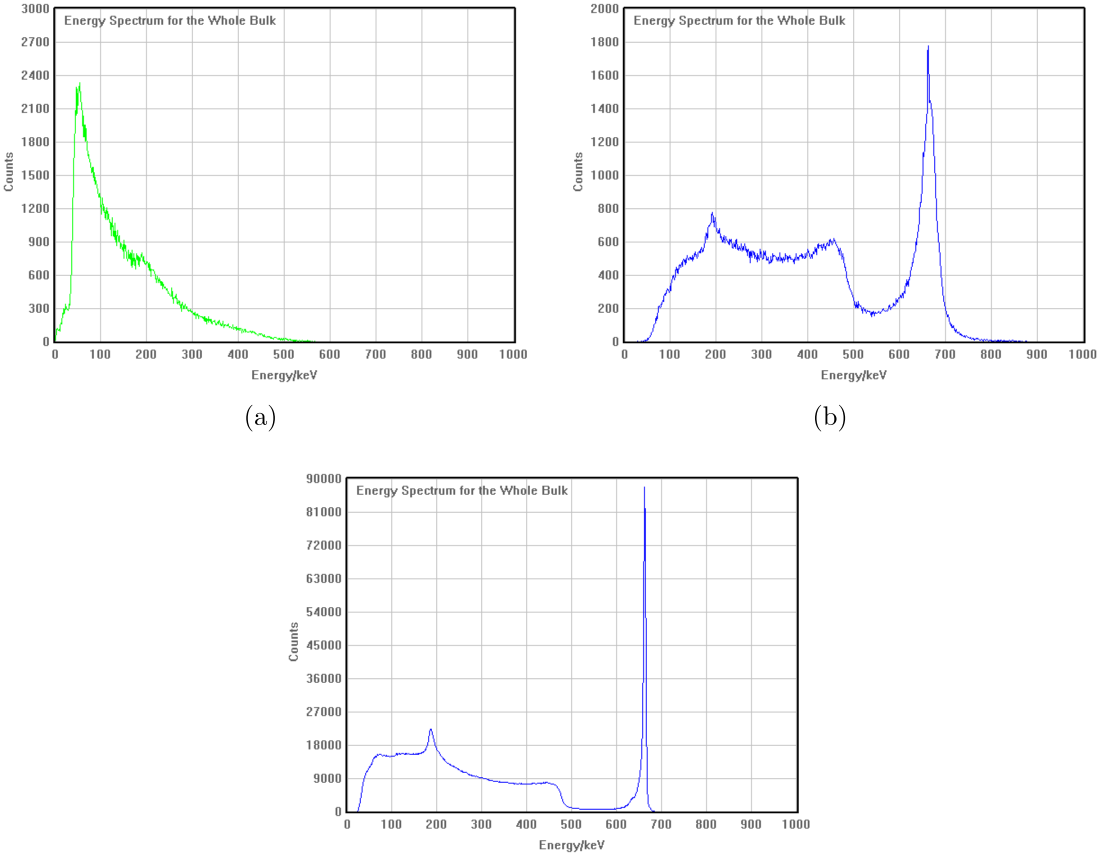

(a) (b)

(c)

Figure 5.17: Comparison between recorded spectrum (a), reconstructed spectrum for incomplete charge collection events (b) and reconstructed spectrum for complete charge collection events (c)

tion.

5.2.5 Estimation on Electron Cloud Size

For a single-pixel photopeak event, the centroid of each electron cloud has to be within a central region of each pixel electrode illustrated by the red squares in Fig. 5.19. If the centroid is outside this region, it will be recorded as a multiple-pixel event. The size of that central region strongly depends on the electron cloud size, therefore, the electron cloud size can be estimated by the increase of photopeak counts. Since the actual electron cloud shape is determined by so many factors, such

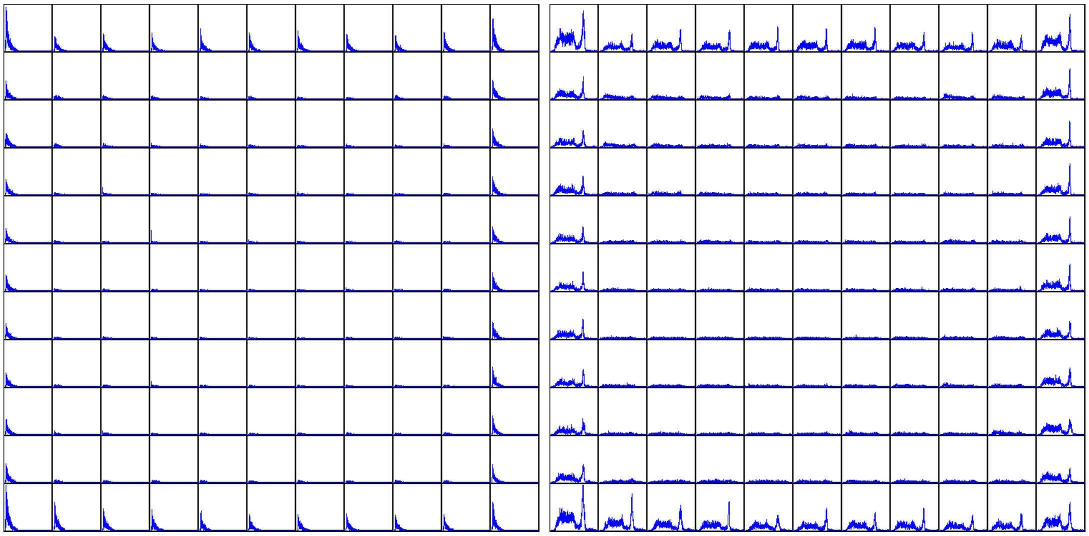
(a) (b)

Figure 5.18: Comparison between recorded spectrum (a) and reconstructed spectrum (b) for incomplete charge collection events on 11×11 pixel map

Table 5.2: Single-pixel Photopeak Counts Improvement

Photopeak Counts	Before Reconstruction	After Reconstruction	Efficiency Improvement
Edge Pixels	256724	304407	18.57%±0.05%
Corner Pixels	36047	48505	34.6%±0.2%
All Pixels	746133	817802	9.61%±0.04%

as incident gamma-ray angle, energy, type of interaction, etc, it is very impractical to describe it analytically. In this study, a simplified square shaped model has been used as a first order estimation. The 11×11 pixels are classified into three different categories based on their locations, 9×9 inner pixels, 4 corner pixels and 36 edge pixels. For the inner 9×9 pixels, if the electron cloud centroid of a photopeak event is sitting out of the red square in Fig. 5.19(a), that electron cloud will be collected by multiple pixels. For edge and corner pixels, since the incomplete charge collection photopeak events can be reconstructed to the correct energy, the effective collection area plotted by red squares in Fig. 5.19(b) and (c) is bigger than that of an inner pixel. The increase of effective collection area should be proportional to the increase

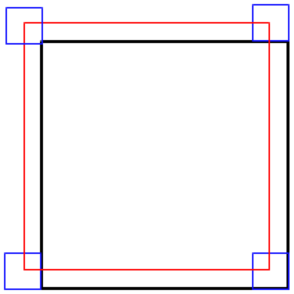
(a) Inne Pixel (b) Edge Pixel (c) Corner Pixel

Figure 5.19: Square shaped electron cloud model on three different located pixel. Black squares stand for boundaries of each pixel anode. Blue squares are the simplified electron cloud and red squares are the electron cloud centroid distribution of single-pixel photopeak event

in photopeak counts, which can be obtained from Table 5.2. Assuming that the diameter of the electron cloud size is x, since the pitch of pixel anode is 1.72 mm, for edge pixels, the relationship can be written as

$$\frac{256724}{304407} = \frac{(1.72 - x) \times (1.72 - x)}{1.72 \times (1.72 - x)} \tag{5.7}$$

and for corner pixels, the relationship can be written as

$$\frac{36047}{48505} = \frac{(1.72 - x) \times (1.72 - x)}{1.72 \times 1.72} \tag{5.8}$$

The average electron cloud size for 662 keV gamma-ray can be estimated using Eq. (5.7) and Eq. (5.8), which is about 260μm. The histogram of electron cloud size derived from 36 edge pixels and 4 corner pixels is shown in Fig. 5.20. The estimation of the electron cloud size for most of the 40 edge and corner pixels is on the order of 200-300μm, which is consistent with the value from Geant4 simulations. The discrepancy between the estimation of the electron cloud size from different pixels could be due to near field source irradiation, non-uniform effective pixel area and approximation in the electron cloud shape model.

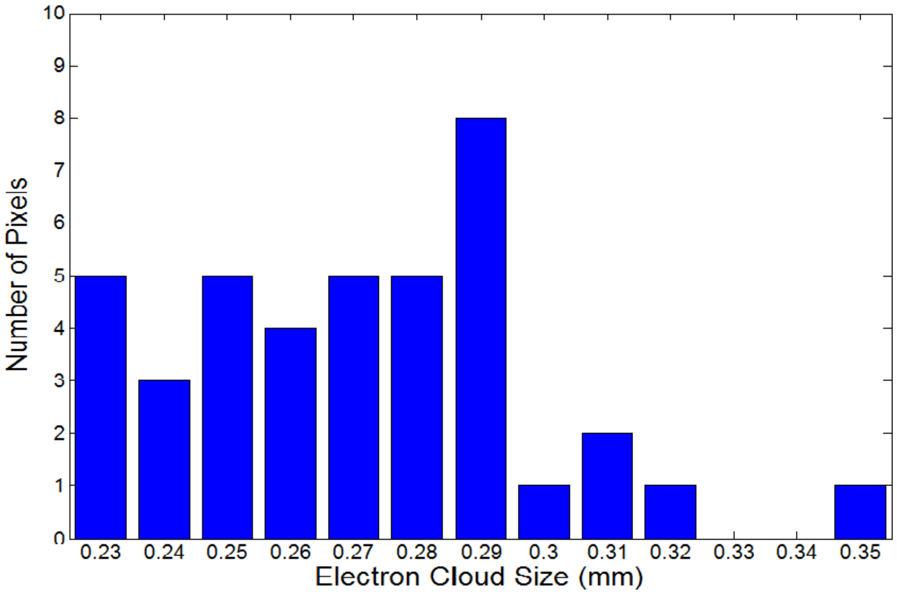

Figure 5.20: Histogram of 40 edge and corner pixel electron cloud size estimation

5.3 Side-Neighbor Charge Leak Events

5.3.1 Motivation

Excellent energy resolution of better than 0.5% FWHM at 662 keV has been achieved for single-pixel events with an analog ASIC readout system developed by Brookhaven National Laboratory [4]. However, false peaks above the photopeak energy have been observed for side-neighbor multiple-pixel events due to transient signals induced on neighbor pixel anodes as shown in Fig. 5.21 [6]. The induced transient signal can be as high as about 10% of that on the collecting pixel according to the Maxwell simulation result [6], depending on the sub-pixel location of the electron cloud. Sometimes the after-shaping transient single can pass the trigger threshold, which can be recorded as a charge collection signal. In order to eliminate these false peaks, signals induced on side-neighbor pixels must be identified as either an induced transient signal due to the drift of electrons in the vicinity of the anode pixel or due to the collection of a small fraction of the electron cloud. The top left plot in Fig. 5.22 shows the after-shaping transient signal of a real gamma-ray event with an equivalent

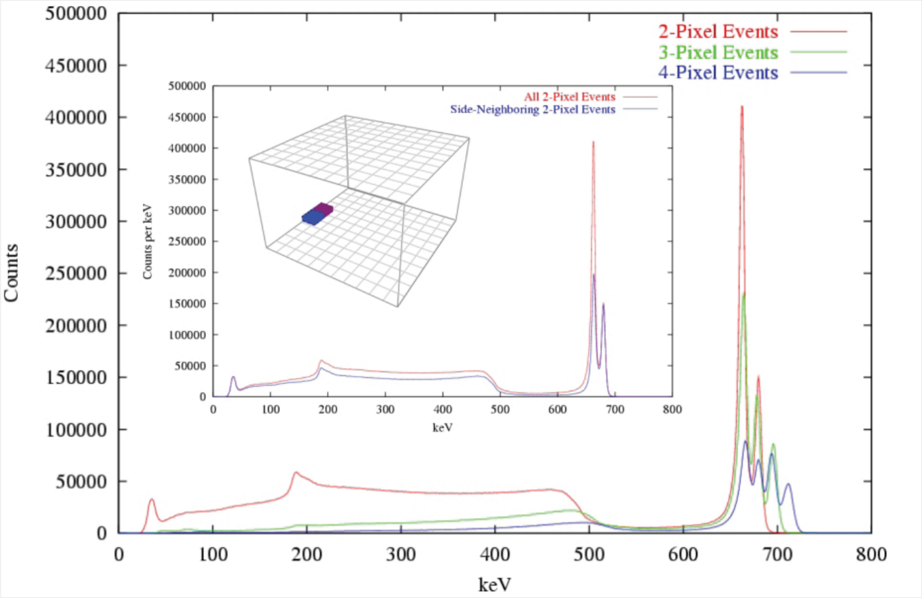

Figure 5.21: False peaks in multiple-pixel events energy spectra caused by transient signals induced on neighboring pixels. The inset spectra show that the events in the false peak all occur on side-neighboring pixels. [6]

amplitude about 30 keV. Increasing the software threshold can correct false peak events back to the correct photopeak energy, with a price of mistakenly shifting some photopeak events to lower energies. This signal deficit occurs because small energy depositions on side-neighbor pixels are ignored. Fig. 5.23 shows that a transient signal has the same signal amplitude as a true charge collection signal after a slow shaper. If the threshold is set above the amplitude of the after-shaping transient signal, the true charge collection signal will also be ignored, which leads to side-neighbor charge leak events. Dr. Yuefeng Zhu has already developed an algorithm to identify and reconstruct charge leak events which are 5 mm or more from the anode surface of the detector based on the averaged neighbor pixel system response function of all inner 9×9 anode pixels. However, when interactions get closer to the anode side, the averaged neighbor pixel system response function is no longer a good approximation. Therefore, the neighbor pixel system response function on a pixel-by-pixel basis was used to reconstruct these events. This work was studied to extend Dr. Yuefeng Zhu's work and further improve the lower tail asymmetry of the photopeak.

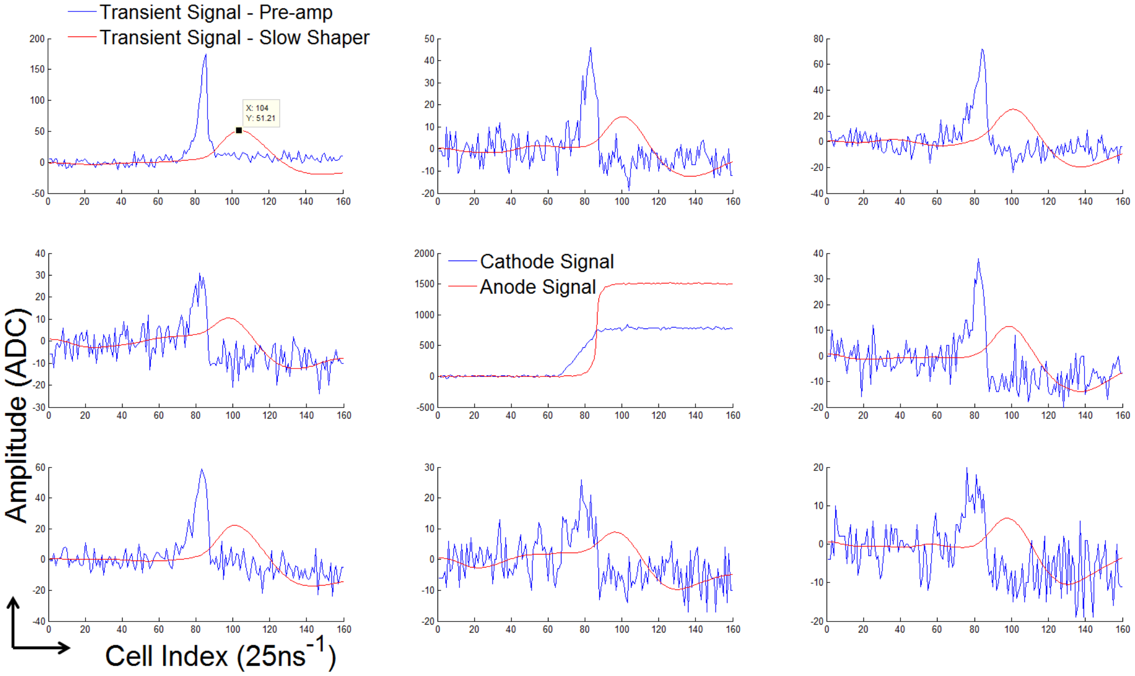

Figure 5.22: The transient signal of a cathode side gamma-ray event has an equivalent amplitude about 30 keV for one gamma-ray event after slow shaper.

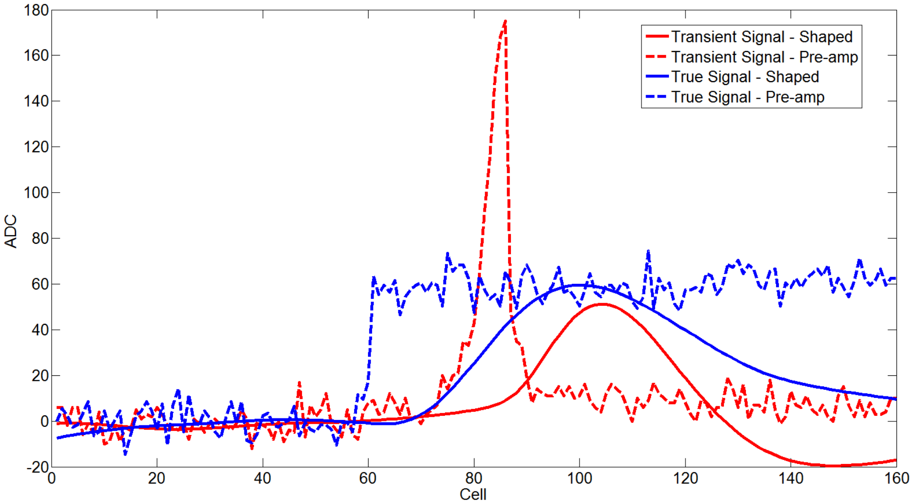

Figure 5.23: Tranisent signal and charge collection singal have the same amplitude after slow shaper for analog ASIC.

5.3.2 Event Identification and Reconstruction

Since the neighbor pixel system response function has been calibrated, the neighbor pixel signal can be predicted as long as the sub-pixel position is known. Simply comparing the recorded neighbor pixel signals to the prediction by the system response function can tell whether there is charge leak or not. If there is charge leak, the signal difference between the recorded signal and the system response function can be used to reconstruct the leaked charge. It has been observed that for the events close to cathode side, the neighbor pixel system response function does not greatly vary. Thus, the average neighbor pixel system response function of all inner anode pixels is sufficient to identify side-neighbor charge leak events for cathode side events. However, when the interaction gets close to the anode side, the neighbor pixel system response function does have pixel-by-pixel variation so a neighbor pixel system response function generated on a pixel-by-pixel basis was used instead as shown in Fig. 5.24. Fig. 5.25 shows an anode side event with charge leaking to the bottom middle pixel. Since the signal amplitude difference is very small, the average neighbor pixel system response will not be able to identify it. The transient signal on Fig. 5.25 also shows a noticeable negative tail amplitude of the transient signal, which allows more charge leak without triggering the system. When the interaction depth gets very close to the anode side, below a pixel pitch size 1.72 mm, the interaction depth becomes very difficult to determine. As a result, only events with interaction depths of more than 1.8 mm from the anode surface were considered in this study.

5.3.3 Photopeak Improvement

Since the tail amplitude of the transient signals depends on the interaction depth and gets more negative for events closer to the anode side, the lower energy tail of the photopeak becomes more prominent as the interaction depth is closer to the anode side. Fig. 5.26 shows the photopeak events at different interaction depths. Before

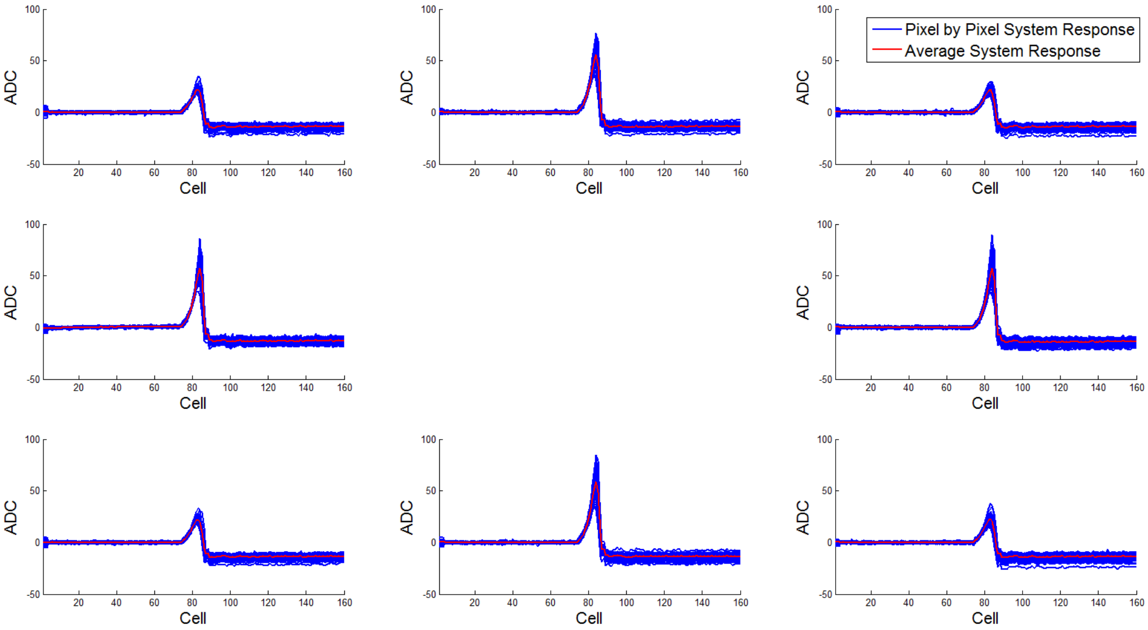

Figure 5.24: System response function for events with interaction depth 5.6 mm and sub-pixel position at the center of each pixel.

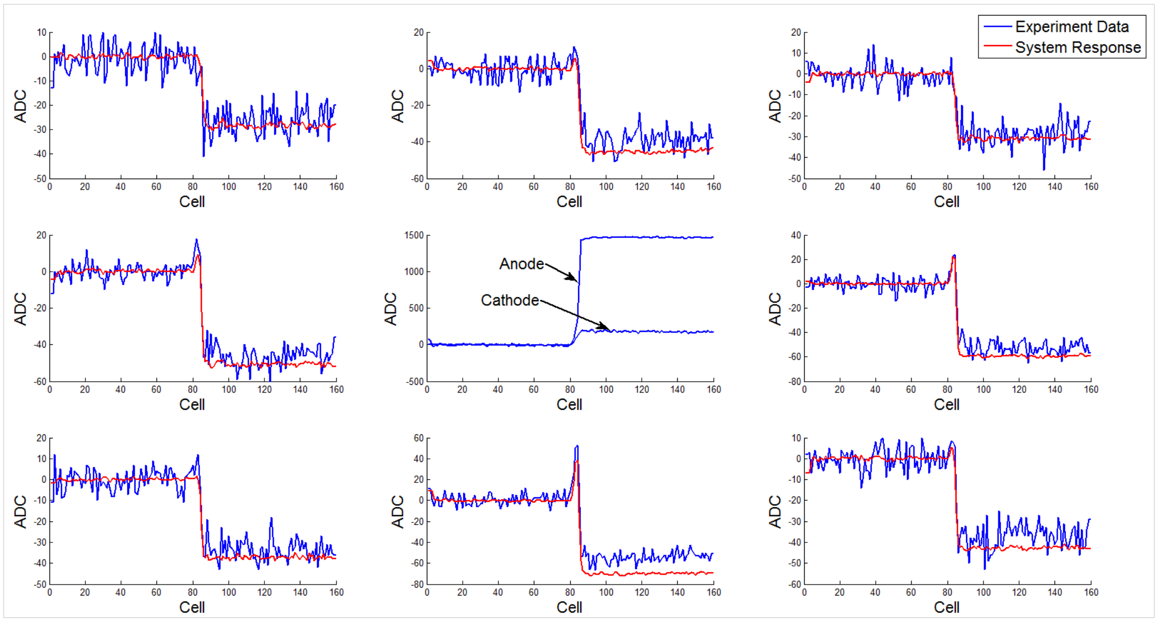

Figure 5.25: A charge leak event with interaction depth about 2 mm from anode surface of the detector

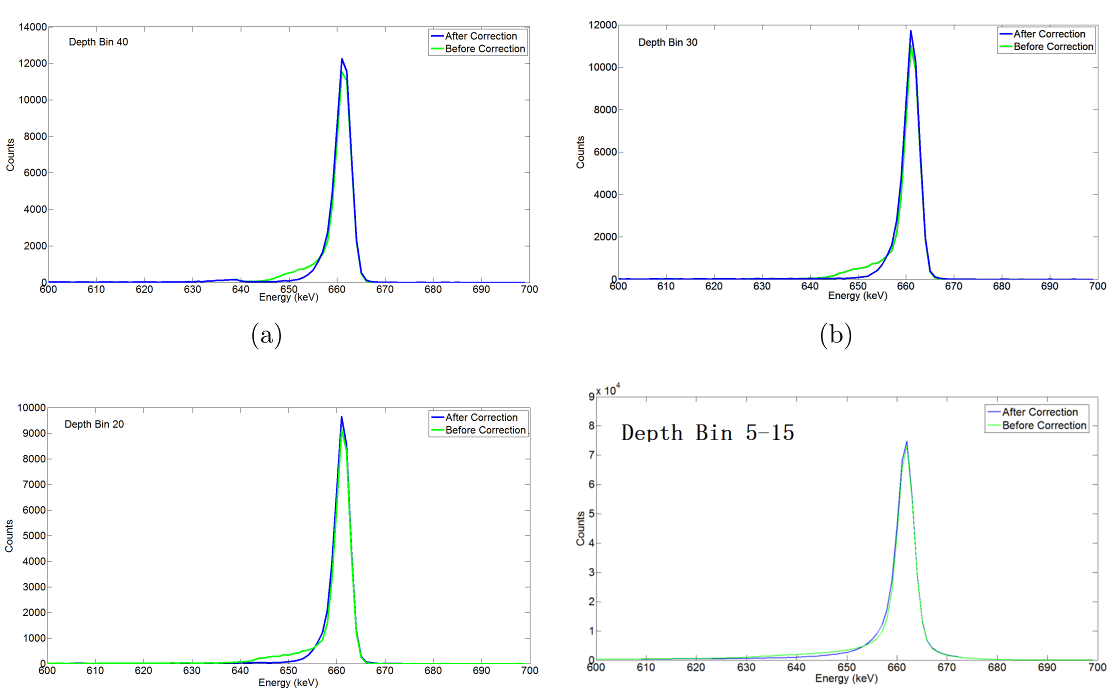

(a) (b)

(c) (d)

Figure 5.26: Full energy deposition events at different interaction depth with and without charge leak reconstruction comparison. Each depth bin has a width about 0.3 mm.

the charge leak correction, every photopeak has a low energy tail as discussed before. The spectrum for depth bins 5-15 has the lower tail extending to 620 keV, which is about 20 keV lower than the other three spectrum due to the more negative tail amplitude. After charge leak reconstruction, the photopeak low energy tail improves significantly as seen in Fig. 5.26(a), (b) and (c). The improvement for events with interaction depth bins between 5 and 15 is not as significant as the other three due to the larger tail extension so in order to illustrate the improvement, only the charge leak events are selected and shown in Fig. 5.27. Clearly, before the charge leak correction, charge leak events build up a broader photopeak with a lower photopeak centroid due to an uncertain amount of charge leaking to the neighbor pixels. After reconstruction, a photopeak with very low tail and correct photopeak centroid shows up.

The fraction of charge leak events at different depth of the detector is shown in

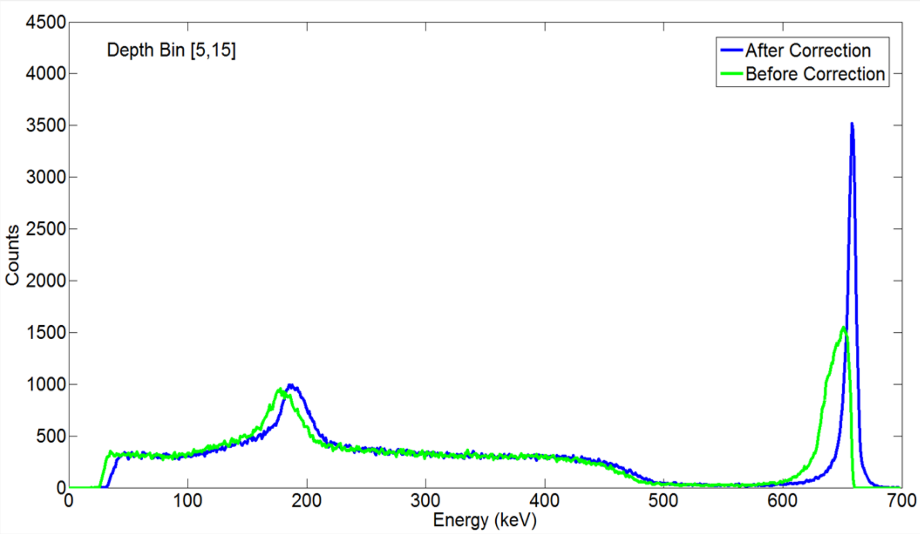

Figure 5.27: Spectrum comparison for charge leak events only with interaction depths between 1.8 and 5.6 mm

Table 5.3: Charge Leak Event(CLE) Identification Rate

Energy Range	0-700 keV		600-700 keV	
All Events	25238433		2795707	
CLE with Depth>5.6 mm[1]	882825	3.498%±0.004%	121552	4.35% ± 0.01%
CLE with 5.6mm>Depth>1.8 mm	206130	0.817% ±0.002%	38591	1.380% ± 0.007%

Table 5.3. With the help of the pixel-by-pixel neighboring pixel system response function, the charge leak events identification and reconstruction algorithm can be extended to about 25% more of the entire detector bulk. By combining this implementation and Dr. Yuefeng Zhu's implementation as shown in Table 5.3, 4.315%±0.004% of all the events can be picked up as charge leak events and 5.73%±0.01% of the photopeak events can be reconstructed back to the correct energy. Since this algorithm is based on the sub-pixel position and interaction depth of each event and only the inner 9×9 pixels can have both information with sufficient accuracy, all the charge leak events identified in the table above are from inner 9×9 pixels and have a depth of interaction greater than 1.8 mm.

---

[1] Dr. Yuefeng Zhu's implementation

5.4 Conclusion

This chapter describes how to utilize the pre-amplifier waveforms provided by the digital ASIC to identify gamma ray events. In the analog ASIC system, only a single amplitude and time information are provided for each channel so some events cannot be properly reconstructed due to the limited information. There are three types of gamma-ray events covered in this chapter: (1) single-pixel multiple interaction events, (2) incomplete charge collection events, and (3) side-neighbor charge leak events. The signature of each type of event has been discussed and the identification algorithm has been developed accordingly. After the events are identified, the corresponding reconstruction algorithms have been used based on the system response function. With the system response function reconstruction, these gamma-ray interactions, especially with full energy deposition, can be reconstructed properly and the lower energy tail of the photopeak is improved.

CHAPTER VI

Applications of Sub-pixel Position Resolution on Material Properties

In pixelated 3-D position sensitive CdZnTe detectors, the lateral position resolution is usually determined by the pixel pitch size. The pixel pitch size is 1.72 mm in large volume 20 mm×20 mm×15 mm CdZnTe detectors manufactured by Redlen used in these studies. Compared to the interaction depth resolution of about 0.5 mm, the lateral position resolution is relatively poor. With the digital ASIC, the transient signals on the neighbor of the collecting pixel can also be recorded and these signals can provide a more precise lateral interaction position, which will improve Compton scattering imaging [5]. Dr. Stephen E. Anderson and Dr. Yuefeng Zhu developed an algorithm to calculate the sub-pixel position of each electron cloud based on these neighbor transient signals [49, 58]. In this chapter, the sub-pixel position information is used to diagnose the material defects in the early batch Redlen detectors. Since the digital ASIC system can provide the pre-amplifier waveforms for each anode pixel, the profile of these waveforms can be used to study the charge transportation and collection problems caused by the material defects. These defects can degrade the accuracy of the sub-pixel position algorithm. It has been observed that the rising time of the anode signal waveforms tends to be longer for the events close to the cathode side. This is likely due to an elongated electron cloud caused by some severe trapping sites in the middle of the detector bulk. These results can be provided to the detector manufacturer so that the crystal growth process can be improved.

6.1 Sub-Pixel Position Sensing

According to the Shockley-Ramo theorem, the induced signal on a collecting electrode is different from that on a non-collecting electrode. In this study, the non-collecting pixel is referred as neighbor pixel. In order to study the charge induction, a waveform simulator was developed by Dr. Jae Cheon Kim [56]. The waveform simulator takes list-mode data containing the gamma-ray interaction location and energy deposition generated by Geant4 and generates the corresponding pre-amplifier waveforms on the collecting electrode and non-collecting electrode.

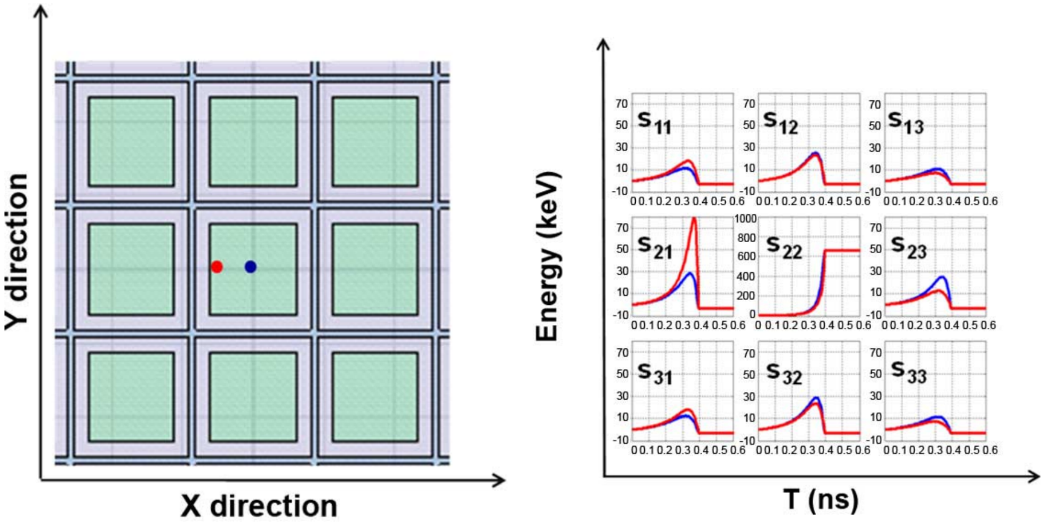

(a) (b)

Figure 6.1: The simulated waveforms (b) of two different sub-pixel locations (a). [7]

Fig. 6.1 illustrates the simulated waveforms for two different sub-pixel locations. The red set of waveforms corresponds to a sub-pixel position close to the left edge of a pixel and the blue set corresponds to the center position of a pixel. Clearly, if the sub-pixel position is close to the edge of a pixel, the closest neighbor pixel has the highest signal amplitude. This observation inspired the sub-pixel calculation algorithm, the maximum transient signal amplitude ratio. However, the maximum transient signal amplitude highly depends on the interaction depth as illustrated by Fig. 5.22 and 5.25 and becomes very small when the depth of interaction is very close to the anode side leading to huge calculation uncertainty for anode side events.

Interestingly, the transient signal peak to tail amplitude does not depend on the interaction depth. It is only determined by the weighting potential of the neighbor pixel, which is basically decided by the electrode size and the detector geometry. Therefore, the sub-pixel position is calculated via the opposing-neighboring ratio using the peak to tail amplitude of the transient signals. The opposing-neighboring ratio is defined as Eq. 6.1 and 6.2, where x_{sub} and y_{sub} are the sub-pixel position and S_{ij} is the peak to tail amplitude corresponding to Fig. 6.1 (b). The precision of the sub-pixel position calculation highly depends on the electronic noise since the transient signal amplitude on the neighbor pixels are very small. Since the electron cloud is not a point in reality due to trapping, de-trapping and diffusion effect, the calculated sub-pixel position is the centroid position of the electron cloud. Clearly, this calculation requires the collecting pixel to have eight neighbor pixels. If the collecting pixel is at the edge or corner, where only three or five neighbor pixels are available, then the sub-pixel position needs to be calculated in alternative way. Therefore, only the inner 9×9 pixels are considered in this study.

$$x_{sub} = \frac{S_L - S_R}{S_L + S_R} = \frac{\sum_{i=1}^{3} S_{i1} - \sum_{i=1}^{3} S_{i3}}{\sum_{i=1}^{3} S_{i1} + \sum_{i=1}^{3} S_{i3}} \tag{6.1}$$

$$y_{sub} = \frac{S_T - S_B}{S_T + S_B} = \frac{\sum_{i=1}^{3} S_{1i} - \sum_{i=1}^{3} S_{3i}}{\sum_{i=1}^{3} S_{1i} + \sum_{i=1}^{3} S_{3i}} \tag{6.2}$$

6.2 Material Defect Study

6.2.1 Double Photopeak Observation

The Traveling Heater Method h(THM) has become another popular method of growing large volume CdZnTe for high-resolution gamma-ray spectroscopic and imaging applications besides High Pressure Bridgman (HPB) recent years. Redlen Technology has adopted it to mass-produce CdZnTe detectors and delivered over 130 detectors for the Polaris project [21]. However, material defects have been observed in the early batch of these THM large volume CdZnTe detectors. One of the most common defects observed with the analog ASIC is the double photopeak for single-pixel events spectrum on some pixels. In order to study this material defect and help Redlen improve their crystal growth technique, the digital ASIC system and sub-pixel position information have been used to diagnose these detectors since the analog ASIC cannot provide sufficient insight of the charge transportation and collection properties.

Fig. 6.2 shows the 11×11 pixel map of photopeak on detector 4R61 and 4R83 before depth correction. Clearly, the top right corner of detector 4R61 has a double photopeak feature, which detector 4R83 does not. Before depth correction, the photopeak region is primarily determined by two competing factors, the collecting pixel weighting potential and electron cloud trapping. Usually, if the internal electric field is uniform and there are no severe trapping centers, the photopeak should not have two photopeak amplitudes, as shown in Fig. 6.2 (b). The largest amplitude difference in 4R61 between the double photopeak is about 100 ADC units, which is about 50 keV. This is very likely to be caused by some severe charge trapping due to the material defect. In order to obtain the position of the material defect, the depth separated spectrum has been studied. Fig. 6.3 shows the depth separated spectrum for one of the double photopeak pixel. There is a layer in the middle of the detector marked

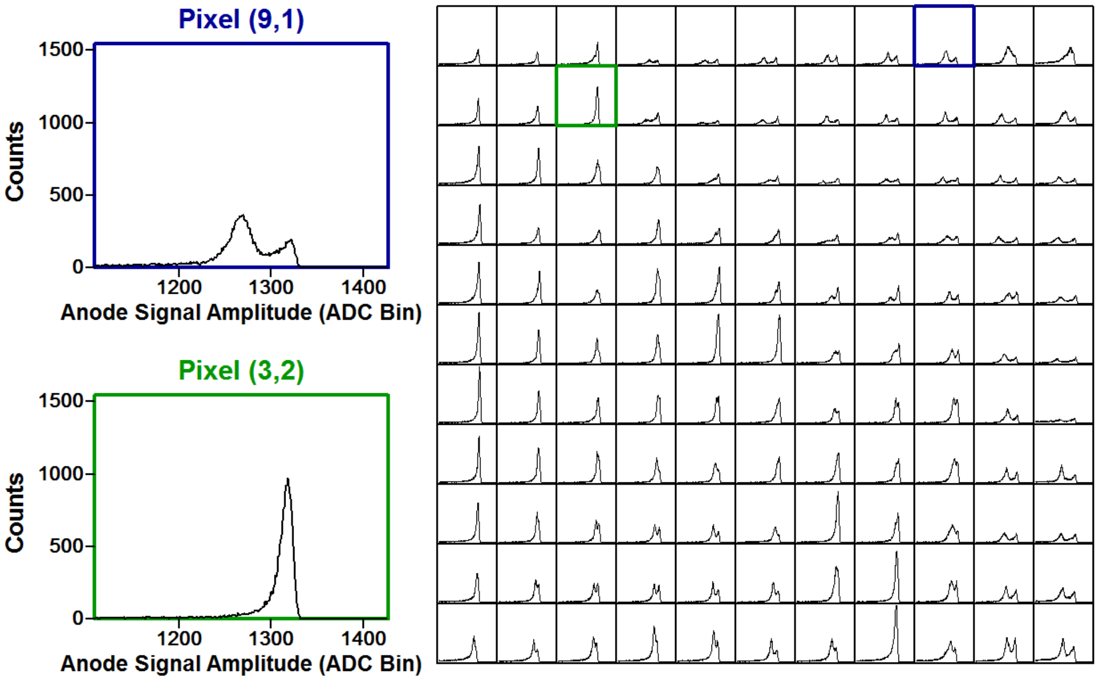

(a)

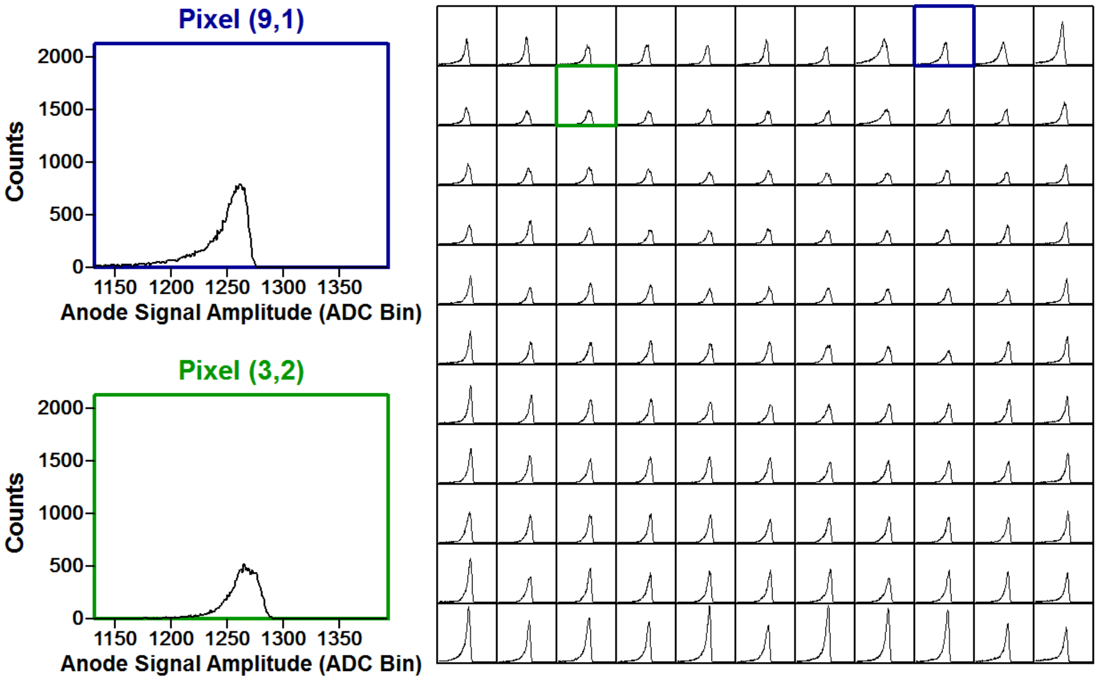

(b)

Figure 6.2: 11×11 pixel map of photopeak on detector 4R61 (a) and 4R83 (b) before depth correction.

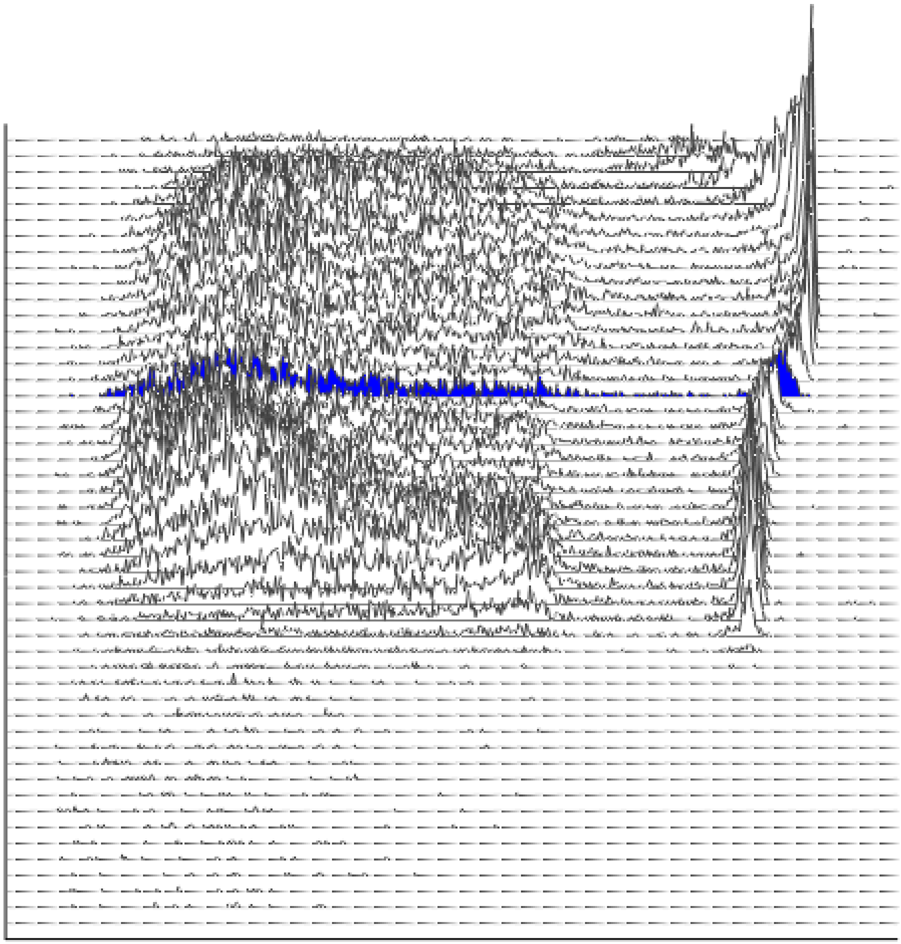

Figure 6.3: Depth separated spectrum for one of the double peak pixel. The top is the anode side and the bottom is the cathode side. The layer marked in blue represents the position of the material defect.

in blue to divide the detector bulk into two parts. If the interaction depth is above this layer, the photopeak centroid is consistently smaller while below, the centroid is higher, which forms the double peak spectrum. Fig. 6.4 illustrates the photopeak centroid vs interaction depth for 121 anode pixels. The dashed red line represents the interaction depth for the photopeak centroid changing position and clearly, it is the same for all the double peak pixels, which is very strong evidence that at that particular depth, in this case about 6 mm from the anode side, there is a material defect layer. This is the best diagnosis achieved by using an analog ASIC.

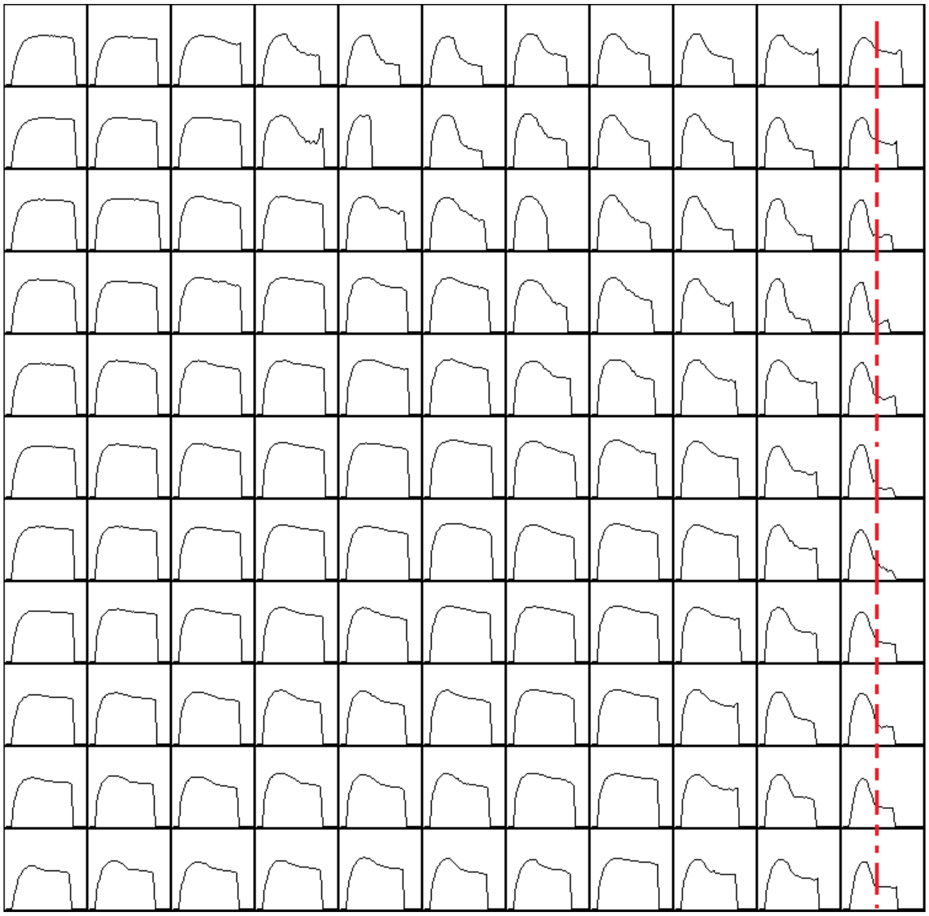

Figure 6.4: Photopeak centroid vs interaction depth for every pixel. The x-axis is the interaction and the y-axis is the photopeak centroid zoomed in range 1200 to 1400 ADC units.

6.2.2 Sub-pixel Position Distribution

As discussed in previous section, the analog ASIC can only tell that there is a charge trapping layer due to material defect in detector 4R61 at depth about 6 mm from the anode side. If it is the charge trapping that causes the photopeak amplitude to have a deficit of about 50 keV, the sub-pixel position distribution of the gamma rays should be still uniform since the ^{137}Cs source was placed on top of the cathode side and the transient signals on the neighbor pixels are affected by this evenly and therefore canceled out according to Eq. 6.1 and 6.2. However, in reality, the sub-pixel position distribution of these double peak pixels on Detector 4R61 is severely distorted

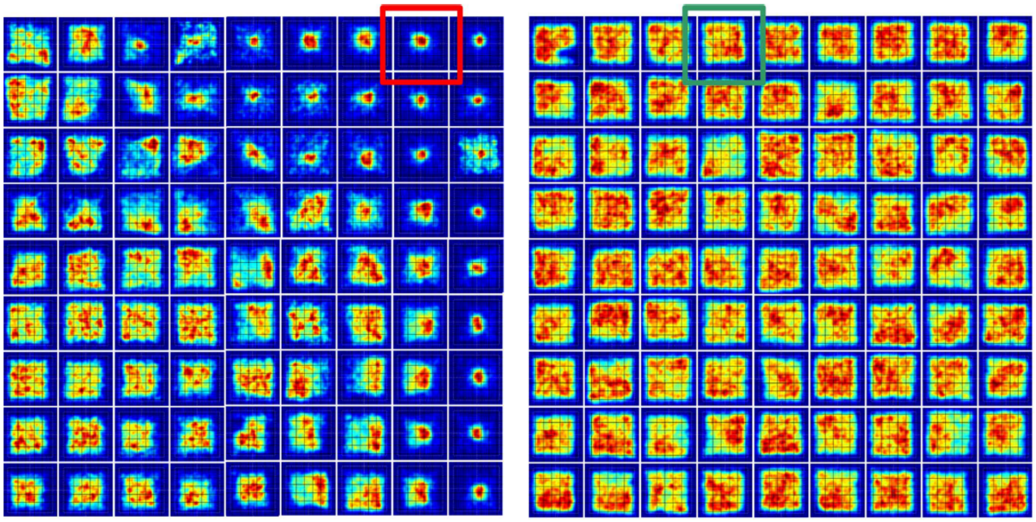
(a) (b)

Figure 6.5: Photopeak event count distribution over 7×7 sub-pixel positions on inner 9×9 anode pixels of detector 4R61 (a) and 4R83 (b). The blue to red color code stands for the counts from low to high. [7]

and biased towards the center of the pixel as shown in Fig. 6.5(a), which indicates that the material defect is not simply a charge trapping layer. As a comparison, the sub-pixel position distribution of 4R83 is shown in Fig. 6.5(b), which is evenly distributed over every pixel with a square like shape representing the pixel pitch [7].

In order to study the impact of the material defect layer, the anode and cathode waveforms for those double peak pixels are picked out shown in Fig. 6.6. Clearly, some of the anode waveforms have significantly longer rising time than others. According to the Shockley-Ramo Theorem, the rising time should be very short since the collecting pixel weighting potential changes rapidly within a pitch size distance from the anode side. The longer rising time means that the charge collection time is unusually long. There are two possibilities to cause a long charge collection time. One possible reason is that the electric field at the anode side is weak so that the drift velocity is slow, which leads to a long charge collection time. However, if the weak electric filed does exist at the anode side, all the events at different depths of interaction should have the same long rising time on the anode pulse waveforms, which in reality is not

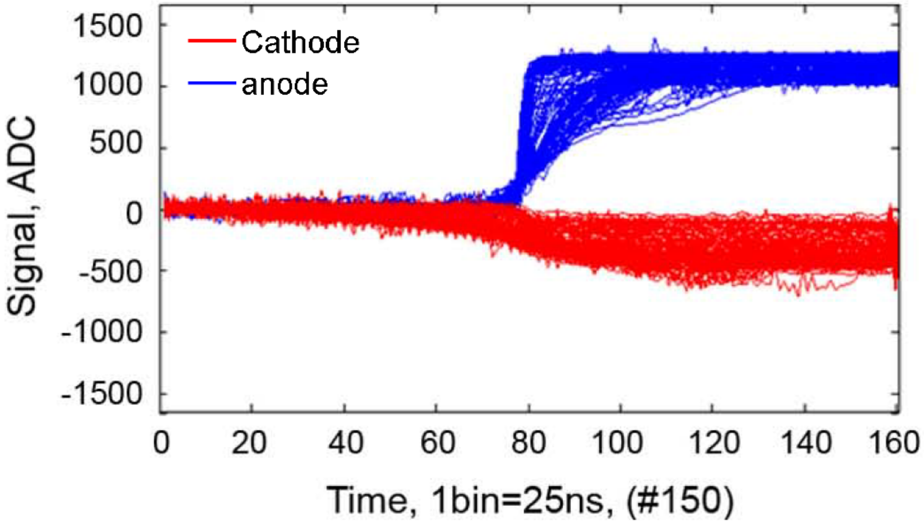

Figure 6.6: Individual energy deposition distribution of single-pixel multiple interaction events. [7]

the case. Therefore, the weak electric filed at the anode side cannot be the reason. The other possible reason is that the electron cloud has a elongated shape along the detector thickness, which results in longer charge collection time. The long shape electron cloud could be caused by the combining effect of trapping and de-trapping. Usually, the de-trapping time is much longer than the charge drifting time so the trapped electron cloud can be treated as charge loss, which is about 3% to 4% along the 15 mm thick detector. If the de-trapping time is relatively short, the trapped electron cloud will be released fairly quick and then change the electron cloud to a longer shape. Thus, the anode waveform rising time T_{RT}, defined as the time interval between the 5% and 95% of the anode amplitude, can be used as a filter parameter to classify the double peak events into two groups as shown in Fig. 6.7. Clearly, there are two peaks in the rising time spectrum, one centroid at 100 ns and the other centroid around 600 ns. The short rising time events corresponding to the higher amplitude peak gives a square shape sub-pixel position distribution. The long rising time events forms a lower amplitude photopeak due to the ballistic deficit besides the severe trapping since the 1 μs shaping time is not long enough for the 600 ns rising

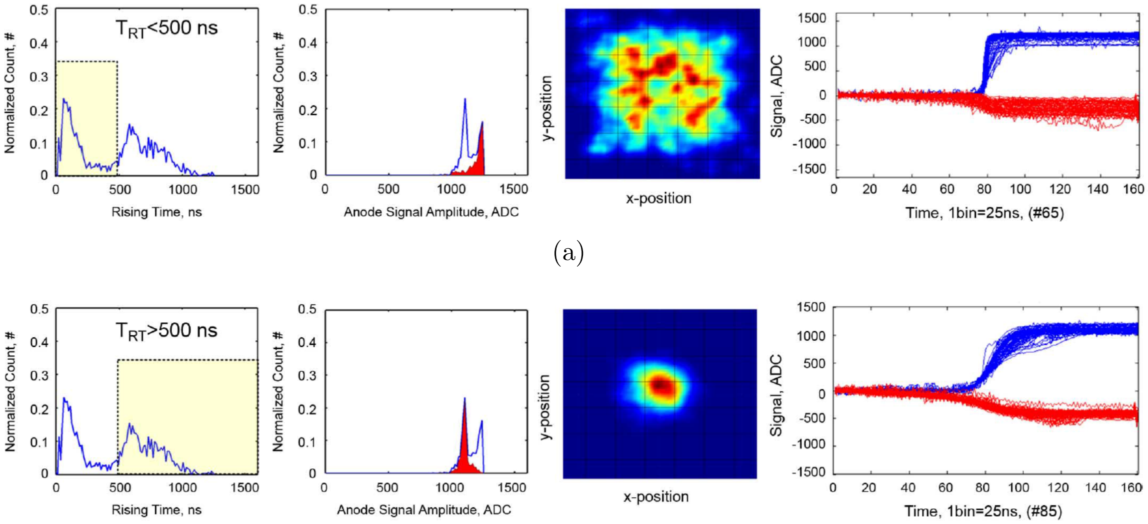

(a)

(b)

Figure 6.7: Anode waveform rising time filter for double photopeak events. (a) events with faster rise time and (b) events with slower rise time. [7]

time.

6.2.3 Simulation Validation

In the waveform simulator, the electron cloud size is determined by two factors, the initial electron cloud size and the diffusion. The initial electron cloud size can be generated by Geant4 simulation by tracking the secondary electrons and the ionization process. The diffusion model has been introduced in Chapter III. Typically, if a 662 keV gamma-ray deposits its full energy at the cathode side of a 15 mm thick detector, the final electron cloud size just before collection is around 200 μm. Fig. 6.8 shows the regular electron cloud model and the elongated electron cloud model at different parts of the detector. Assuming the electron cloud is evenly collected, the size of 600 ns rising time electron cloud should be 5 times bigger than the typical one. Therefore, an artificial expansion about 1.2 mm along the depth direction is added as the third factor determining the electron cloud size. The collecting pixel waveforms and non-collecting waveforms corresponding to different electron cloud(EC) model are

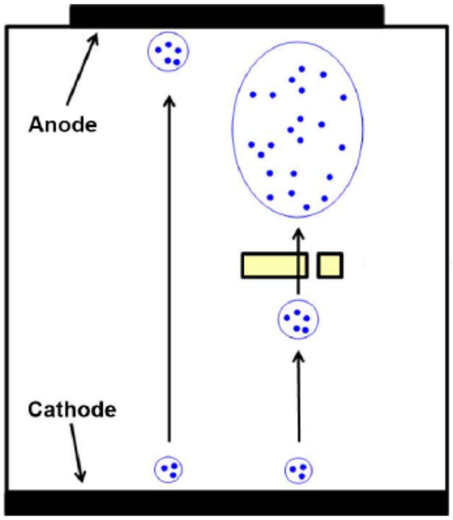

Figure 6.8: Illustration of the material defect layer causing the elongated shape of the electron cloud. [7]

shown in Fig. 6.9. Fig. 6.9(a) shows the similar waveform profile to the experimental data on Fig. 6.6, which indicates that the elongated shape electron cloud is a valid hypothesis. The transient signals amplitude on the non-collecting pixels are severely underestimated due to the long shape of the electron cloud, which biases the sub-pixel position calculation towards the center of the collecting pixel according to the Eq. 6.1 and 6.2. The dashed transient signals on Fig. 6.9(b) are corresponding to 0.4 mm, 0.6 mm, 0.8 mm, 1 .0 mm and 1.2 mm electron cloud vertical expansion [7].

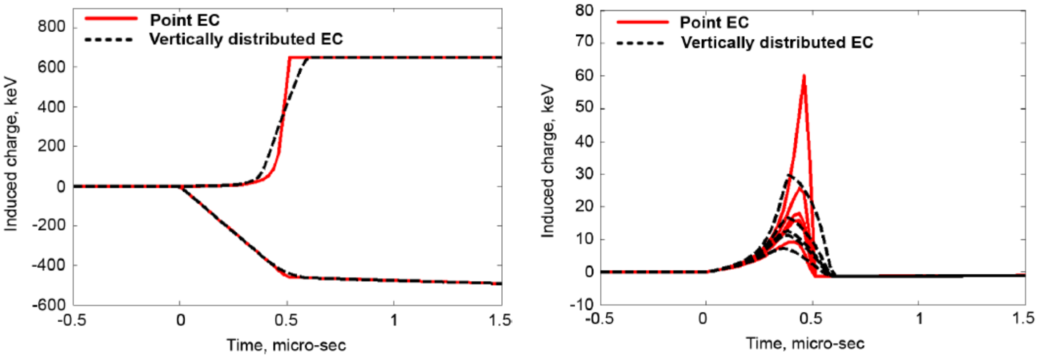

(a) (b)

Figure 6.9: Simulated waveforms on the (a) collecting pixel, and (b) non-collecting pixel corresponding to different electron cloud model. [7]

6.3 Conclusion

This chapter presents one material defect diagnosis technique using the digital ASIC system and the sub-pixel position distribution. The algorithm of the sub-pixel position calculation using the transient signals has been introduced. A large volume Redlen detector with double photopeak feature has been studied with both the analog ASIC and the digital ASIC. The analog ASIC can only tell there is a trapping layer in the middle of the detector bulk, which caused the photopeak event signal amplitude to have a deficit. The assumption of this trapping layer turned out to be not sufficient to fully explain the sub-pixel position distribution. The anode waveforms from those double pohotopeak pixels showed different rising time, which is assumed to be caused by a vertically distributed electron cloud. The waveform simulator generated the similar rising time profile by artificially expanding the electron cloud vertically. This effect was reported back to the detector manufacturer Redlen so that they can improve the crystal growth technique to minimize this material defect in future production.

CHAPTER VII

Conclusions and Future Work

7.1 Conclusions

The active volume of 20 mm×20 mm×15 mm CdZnTe detectors manufactured by Traveling Heater Method has been examined by a relative efficiency experiment and has been proven to be greater than 95%. The digital ASIC array system with 2 keV FWHM electronic noise has been applied to these large volume CdZnTe detectors and excellent spectroscopic performance has been demonstrated. The K X-rays from ^{137}Cs at 32 and 36 keV have been resolved for the first time with the digital ASIC system. The non-linearity of the digital ASIC array has also been studied and the performance of non-linearity correction has been verified by gamma-rays with different energies to be no more than ±2 keV within the dynamic range of 30 keV to 3 MeV. The single-module multiple pixel event energy resolution degradation has been investigated and shown to be caused by the weighting potential cross-talk correction imperfection. Three types of events including single-pixel multiple interaction events, incomplete charge collection events and side-neighbor charge leakage events have been successfully identified and reconstructed. Sub-pixel resolution distribution has been used to diagnose the material defect and the anode waveforms have been observed to have long rising time, which leads to the electron cloud elongation hypothesis. A simulation has been used to verify the hypothesis and the result is useful for the manufacturer to improve crystal growth technique.

7.2 Future Work

The real time data acquisition software developed for TlBr detectors is fully functional and has demonstrated the real time raw spectrum buildup. However, the real time spectrum calibration has not been implemented, which will be useful for real time application, especially the multiple pixel events for Compton imaging. The hole movement has been observed from the cathode waveforms and it will degrade the accuracy of the C/A ratio for depth calculation. Using cathode side events to create system response function may improve the depth calculation and isolate the signal contribution from hole movement.

It has been observed that the spectroscopic performance of the analog ASIC system with the same CdZnTe detector is better in winter than in summer. The same behavior has been noticed on the digital ASIC array system. A temperature study with the previous generation digital ASIC has been performed by Dr. Yuefeng Zhu with HgI_2 detectors. Therefore, it could be also useful to study the temperature dependent response of the digital ASIC array system with CdZnTe detectors. Since lower temperature will lead to lower electronic noise and better lateral charge collection non-uniformity [59], the overall energy resolution of CdZnTe should be improved further closer to the theoretical limit of 0.2% at 662 keV if the detectors are operated at room temperatures.

The single-pixel incomplete charge collection events have been successfully identified and reconstructed using system response function. The multiple pixel incomplete charge collection events involves multiple scenarios: (1) only one of all interactions has incomplete charge collection, (2) only some of all interactions have incomplete charge collection, and (3) even all interaction have incomplete charge collection. In addition, multiple pixel events will tend to have more interactions on the edge pixels, which leads to a higher probability of having incomplete charge collection. To simplify the event identification, two pixel events should be first studied. Since only the edge pixels can have incomplete charge collection, two pixel events can be divided into three major groups: (1) both interactions on the inner 9 by 9 pixels, (2) both interaction on the outer 40 edge pixels, and (3) one interaction on the inner pixel and the other on the outer pixels. Only events from the later two groups can have incomplete charge collection, which simplifies the event classification algorithm. Since the drift time of both interactions is still valid, the calculated to measured cathode signal ratio can be used as the signature of two pixel incomplete charge collection events.

BIBLIOGRAPHY

BIBLIOGRAPHY

[1] Z. He, "Review of the shockley ramo theorem and its application in semiconductor gamma-ray detectors," *Nucl. Inst. Meth. Phys. Res. A.*, vol. 463, no. 12, pp. 250 – 267, 2001.

[2] D. Xu, "Gamma-ray imaging and polarization measurement using 3-D position-sensitive cdznte detectors," *PhD thesis, University of Michigan*, 2006.

[3] P. N. Luke, "Single-polarity charge sensing in ionization detectors using coplanar electrodes," *Applied Physics Letters*, vol. 65, pp. 2884 – 2886, 1994.

[4] F. Zhang, C. Herman, Z. He, G. D. Deronimo, E. Vernon, and J. Fried, "Characterization of the H3D ASIC readout system and 6.0 cm^3 3-D position sensitive CdZnTe detectors," *IEEE Trans. Nucl. Sci.*, vol. 59, no. 1, p. 236, 2012.

[5] Y. Zhu, *Digital Signal Processing Methods for Pixelated 3-D Position Sensitive Room-Temperature Semiconductor Detectors.* PhD thesis, University of Michigan, 2012.

[6] F. Zhang, W. Kay, and Z. He, "Performance of 3-D position sensitive CdZnTe detectors for gamma-ray energies above 1 Mev," *Proc. IEEE Nucl. Sci. Symp. Conf. Record (NSS/MIC)*, vol. 31, pp. 2012 – 2016, 2009.

[7] J. C. Kim, W. Kaye, H. Yang, C. R. Brown, and Z. He, "Improvement of sub-pixel position sensing in nonuniform large-volume pixelated CdZnTe crystals," *IEEE Transactions on Nucl. Sci.*, vol. 60, no. 2, p. 1201, 2013.

[8] http://www.evproducts.com/pdf/material_prop.pdf.

[9] C. Celiktas, E. E. Ermis, and M. Bayburt, "Energy resolution improvement of NaI(Tl) scintillation detectors by means of a timing discrimination method," *J Radioanal Nucl Chem*, vol. 293, pp. 377 – 382, 2012.

[10] G. F. Knoll, *Radiation Detection and Measurement.* Hoboken, NJ: John Wiley & Sons, Inc, third ed., 1999.

[11] E. Sakai, "Present status of room temperature semiconductor detectors," *Nucl. Instrum. Methods*, vol. 196, p. 121, 1982.

[12] D. S. McGregor and H. Hermon, "Room-temperature compound semiconductor radiation detectors," *Nuclear Instruments and Methods in Physics Research A*, vol. 395, pp. 101 – 124, 1997.

[13] F. Doty, H. Barber, F. Augustine, J. Butler, B. Apotovsky, E. Young, and W. Hamilton, "Pixellated CdZnTe detector arrays," *Nuclear Instruments and Methods in Physics Research A*, vol. 353, pp. 356 – 360, 1994.

[14] B. E. Patt, J. Iwanczyk, G. Vilkelis, and Y. Wang, "New gamma-ray detector structures for electron only charge carrier collection utilizing high-Z compound semiconductors," *Nuclear Instruments and Methods in Physics Research A*, vol. 380, pp. 276 – 281, 1996.

[15] F. P. Doty, J. F. Butler, J. F. Schetzina, and K. A. Bowers, "Properties of CdZnTe crystals grown by a high pressure bridgman method," *J. Vac. Sci. Technol. B*, vol. 10, pp. 1418 – 1422, 1992.

[16] J. F. Butler, F. P. Doty, and C. Lingren, "Recent developments in CdZnTe gamma ray detector technology," *SPIE Gamma-Ray Detectors*, vol. 1734, p. 131, 1992.

[17] J. F. Butler, F. P. Doty, B. Apotovsky, S. J. Friesenhahn, and C. Lingren, "Progress in $Cd_{1-x}Zn_xTe$ (CZT) radiation detectors," *MRS Proceedings*, vol. 299, pp. 249 – 258, 1994.

[18] T. B. Mohammed, A. Friant, and J. Mellet, "Structure mis effects on polarization of HgI_2 crystals used for gamma-ray detection," *IEEE Transactions on Nuclear Science*, vol. 32, pp. 383 – 385, 1985.

[19] P. Siffert, J. Berger, C. Scharager, A. Cornet, R. Stuck, R. Bell, H. B.Serreze, and F. V. Wald, "Polarization in cadmium telluride nuclear radiation detectors," *IEEE Transactions on Nuclear Science*, vol. 23, pp. 159 – 170, 1976.

[20] R. Bell, G. Entine, and H. Serreze, "Time-dependent polarization of CdTe gamma-ray detectors," *Nuclear Instruments and Methods*, vol. 117, pp. 267 – 271, 1974.

[21] Y. A. Boucher, *Analysis of Cadmium Zinc Telluride Detector Performance and Characteristics for Applications in Gamma-Ray Imaging Spectrometers.* PhD thesis, University of Michigan.

[22] W. Shockley, "Currents to conductors induced by a moving point charge," *J. Appl. Phys*, vol. 9, p. 635, 1938.

[23] S. Ramo, "Currents induced by electron motion," *I.R.E. Proceedings*, p. 584, 1939.

[24] G. Bertolini and A. (eds.), *Semiconductor Detectors.* Amsterdam, Holland: Elsevier, 1968.

[25] O. Frisch, "British atomic energy report," *BR-49*, 1944.

[26] P. N. Luke, "Unipolar charge sensing with coplanar electrodes-application to semiconductor detectors," *IEEE Trans. Nucl. Sci.*, vol. 42, no. 4, pp. 207 – 213, 1994.

[27] T. Narita, J. E. Grindlay, J. Hong, and F. C. Niestemski, "Anode readout for pixellated CZT detector," *Proceedings SPIE*, vol. 5165, pp. 542 – 547, 2004.

[28] H. H. Barrett, J. D. Eskin, and H. B. Barber, "Charge transport in arrays of semiconductor gamma-ray detectors," *Physical Review Letters*, vol. 75, no. 1, p. 156, 1995.

[29] Z. He, G. F. Knoll, D. K. Wehe, R. Rojeski, C. H. Mastrangelo, M. Hammig, C. Barrett, and A. Uritani, "1-d position sensitive single carrier semiconductor detectors," *Nucl. Inst. Meth. Phys. Res. A.*, vol. 380, p. 228, 1996.

[30] Z. He, G. F. Knoll, D. K. Wehe, and J. Miyamoto, "Position-sensitive single carrier cdznte detectors," *Nucl. Inst. Meth. Phys. Res. A.*, vol. 388, p. 180, 1997.

[31] F. Zhang, *Events reconstruction in 3-D position sensitive CdZnTe gamma-ray spectrometers.* PhD thesis, University of Michigan, 2005.

[32] F. Zhang, C. Herman, Z. He, G. D. Deronimo, E. Vernon, and J. Fried, "Advancement in the BNL H3Dv4 ASIC readout system for 3-D position sensitive CdZnTn detectors," *IEEE Conference*, 2012.

[33] W. Li, Z. He, G. F. Knoll, D. K. Wehe, and J. E. Berry, "A data acquisition and processing system for 3-D position sensitive czt gamma-ray spectrometers," *IEEE Trans. Nucl. Sci.*, vol. 46, no. 6, p. 1989, 1999.

[34] W. Li, Z. He, G. F. Knoll, D. K. Wehe, and C. M. Stahle, "Spatial variation of energy resolution in 3-D position sensitive CZT gamma-ray spectrometers," *IEEE Trans. Nucl. Sci.*, vol. 46, no. 3, p. 187, 1999.

[35] F. Zhang, Z. He, D. Xu, G. F. Knoll, D. K. Wehe, and J. E. Berry, "Improved resolution for 3-D position sensitive CdZnTe spectrometers," *IEEE Trans. Nucl. Sci.*, vol. 51, no. 5, p. 2427, 2004.

[36] F. Zhang, Z. He, G. F. Knoll, D. K. Wehe, and J. E. Berry, "3-D position sensitive CdZnTe spectrometer performance using third generation VAS/TAT readout electronics," *IEEE Trans. Nucl. Sci.*, vol. 52, no. 5, p. 2009, 2005.

[37] F. Zhang, Z. He, G. F. Knoll, D. K. Wehe, and J. E. Berry, "New readout electronics for 3-D position sensitive CdZnTe/HgI$_2$ detector arrays," *IEEE Trans. Nucl. Sci.*, vol. 53, no. 5, p. 3021, 2006.

[38] W. Kaye, Y. A. Boucher, F. Zhang, and Z. He, "Calibration and operation of the Polaris 18-Detector CdZnTe array," *Nuclear Science Symposium Conference Record (NSS/MIC)*, p. 3821, 2010.

[39] C. E. Lehner, F. Zhang, and Z. He, "4π Compton imaging using a 3-D position-sensitive CdZnTe detector via weighted list-mode maximum likelihood," *IEEE Trans. Nucl. Sci.*, vol. 51, no. 4, p. 1618, 2004.

[40] C. E. Lehner, *4π Compton Imaging Using a single 3-D Position-Sensitive CdZnTe Detector*. PhD thesis, University of Michigan, 2004.

[41] S. J. Kaye, W. R. Kaye, and Z. He, "Experimental demonstration of coded aperture imaging using thick 3D-position-sensitive CdZnTe detectors," *Nuclear Science Symposium Conference Record (NSS/MIC)*, pp. 1902 – 1906, 2009.

[42] W. K. Warburton, "An approach to sub-pixel spatial resolution in room temperature X-ray detector arrays with good energy resolution," *Mat. Res. Symp. Proc.*, vol. 487, pp. 531 – 535, 1998.

[43] C. S. Williams, W. P. Baker, L. W. Burggraf, P. E. Adamson, and J. C. Petrosky, "Toward simultaneous 2D ACAR and 2D DBAR: Sub-pixel spatial characterization of a segmented HPGe detector using transient charges," *IEEE Transactions on Nucl. Sci.*, vol. 57, pp. 860 – 869, 2010.

[44] Z. He, "Digital 3-D position-sensitive CdZnTe gamma-ray detectors," *SORMA*, 2010.

[45] M. Amman, A. Priest, P. N. Luke, S. Asztalos, K. Sabourov, and K. Vetter, "Proximity electrode signal readout of high-purity ge detectors," *IEEE Transactions on Nucl. Sci.*, vol. 60, no. 2, p. 1213, 2013.

[46] H. Sakai, Y. Takenaka, A. Uritani, K. Inoue, and C. Mori, "Improvement of energy spectrum characteristics of cdznte semiconductor detector by means of digital waveform processing with neural network algorithm," *Nuclear Instruments and Methods in Physics Research A*, vol. 400, pp. 401 – 408, 1997.

[47] L. Zhang, H. Takahashi, D. Fukuda, and M. Nakazawa, "Clustering method to process signals from a cdznte detector," *Journal of Nuclear Science and technology*, vol. 38, no. 7, 2001.

[48] K. Hitomi, T. Tada, S. Kim, H. Yamazaki, and K. Ishii, "Measurement of electron drift mobility in tlbr crystals," *CYRIC Annual Report*, 2010-2011.

[49] S. E. Anderson, *Event Classification for 3-D Position Sensitive Semiconductor Detectors*. PhD thesis, University of Michigan, 2011.

[50] A. E. Bolotnikov, G. S. Camarda, Y. Cui, G. D. Geronimo, J. Fried, R. Gul, A. Hossain, K. Kim, G. Yang, E. Vernon, and R. B. James, "Rejecting incomplete charge-collection events in CdZnTe and other semiconductor detectors," *Nuclear Instruments and Methods in Physics Research A*, vol. 664, pp. 317–323, 2012.

[51] A. E. Bolotnikov, J. Butcher, G. S. Camarda, Y. Cui, G. D. Geronimo, J. Fried, R. Gul, P. M. Fochuk, M. Hamade, A. Hossain, K. Kim, O. Kopach, M. Petryk, E. Vernon, G. Yang, and R. B. James, "Array of virtual Frisch-Grid CZT detectors with common cathode readout for correcting charge signals and rejection of incomplete charge-collection events," *IEEE Trans. Nucl. Sci.*, vol. 59, pp. 1544 – 1551, 2012.

[52] K. Hitomi, T. Tada, S. Kim, Y. Wu, T. Tanaka, T. Shoji, H. Yamazaki, and K. Ishii, "Recent development of TlBr gamma-ray detectors," *IEEE Transactions on Nucl. Sci.*, vol. 58, pp. 1987 – 1991, 2011.

[53] C. Thrall, *Alternative Wide-Band-Gap Materials for Gamma-Ray Spectroscopy.* PhD thesis, University of Michigan, 2013.

[54] M. L. Rodrigues, *High-Flux Experiments and Simulations of Pulse-Mode Position-Sensitive CdZnTe Pixelated Detectors.* PhD thesis, University of Michigan, 2012.

[55] H. Yang, J. C. Kim, and Z. He, "Event classification and reconstruction of single pixel multiple interaction events," *Nuclear Science Symposium Conference Record (NSS/MIC)*, pp. 4663 – 4667, 2011.

[56] J. C. Kim, S. E. Anderson, W. Kaye, F. Zhang, Z. He, and et al., "Charge sharing in common-grid pixelated CdZnTe detectors," *Nuclear Instruments and Methods in Physics Research A*, vol. 654, no. 1, pp. 233 –243, 2011.

[57] H. Yang and Z. He, "Identification and reconstruction of single-pixel incomplete charge collection events," *IEEE Transactions on Nucl. Sci.*, vol. 60, pp. 1243 – 1247, 2013.

[58] Y. Zhu, S. E. Anderson, and Z. He, "Sub-pixel position sensing for pixelated, 3-D position sensitive, wide band-gap, semiconductor,gamma-ray detectors," *IEEE Transactions on Nucl. Sci.*, vol. 58, no. 3, pp. 1400 – 1409, 2011.

[59] Y. Zhu, W. R. Kaye, Z. He, and F. Zhang, "Performance improvement of 3-D positionsensitive pixellated HgI_2 detectors when cooled from room temperature to 10°c," *Nuclear Science Symposium Conference Record (NSS/MIC)*, p. 3959, 2010.